Investigating the use of Two-Photon Polymerisation for the Creation of Gradient Index Optics

Emma Marie Woods

Thesis submitted to the University of Nottingham
for the degree of
Doctor of Philosophy

October 2022

This thesis is dedicated to my wonderful grandmother for fostering my love of learning and being a beacon of support.

Abstract

Metamaterials consist of repeating unit cells resulting in a homogeneous averaged electromagnetic (EM) response. Spatially varying EM properties can be created by introducing variations within each unit cell. In this way gradient index (GRIN) metamaterials offer a route to developing GRIN optics with larger refractive index (RI) gradients compared to traditional GRIN optics. By altering the length scale of the features within the metamaterial, the lens can be designed to work in different parts of the EM spectrum opening up new avenues for telecommunications and integrated optics.

The aim of this work was to investigate the use of two-photon polymerisation (TPP), an additive manufacturing technique, to fabricate a GRIN metamaterial lens. The lens was to work in the $1\ \mu\text{m} - 2\ \mu\text{m}$ wavelength region (corresponding to $150\ \text{THz} - 300\ \text{THz}$) necessitating the nanoscale feature sizes TPP provides. Compared to conventional nanofabrication techniques, TPP is a truly 3D fabrication process that can open up the design space of metamaterial geometries.

Firstly, the line widths of a commercial resin, IP-L (Nanoscribe GmbH), at different laser powers and scan speeds were measured by fabricating ascending scan arrays using the commercial Nanoscribe GmbH Photonic Professional GT. By changing the laser dose, the focal spot of the laser is changed which results in different cured line dimensions. The minimum achievable line width determines the lowest wavelength the metamaterial would work at. Whereas the range of line widths determines the amount by which the metamaterial unit cells can be altered to produce the spatially varying properties. This work found the maximum line width to be 561 nm ± 21 nm and the minimum to be 273 nm ± 32 nm, resulting in a range of 228 nm ± 53 nm.

The capabilities of the TPP system were investigated by fabricating woodpile structures with different laser power parameters across the devices. Two different substrate preparation techniques were compared, as well as fabricating structures with and without frames for added structural stability. The initial investigation led to the design of the metamaterial structure used in this work; the cylindrical fishnet. This structure is made up of layers of concentric rings filled in by an increasing number of spokes in successive rings. This results in a structure somewhat like a circularly deformed fishnet structure.

Analytical calculations were undertaken to estimate the RI based on the filling fraction of the cylindrical lens structure for different line widths and number of spokes between each ring. A hyperbolic secant (sech) profile is normalised to the maximum and minimum analytical RI results and different line width / number of spokes combinations were selected which fall along this curve. Four lenses were designed in this way, and the 7 selected unit cells for each were simulated using finite element method modelling in COMSOL to investigate the geometry dependent RI.

A rectangular cut out geometry was used to approximate the unit cells for simulation to reduce computational requirements. The results were compared to the ideal sech curve as well as the analytical RI calculations for both the full cylindrical fishnet and the rectangular cut out. The analytical calculations for the rectangular cut out did not appear to predict the simulated results better than the cylindrical fishnet analytical calculations.

Using the analytical and simulated RI results, the focal lengths of the four lenses were predicted analytically. COMSOL simulations were used to investigate the focal length and relative focal spot size for each of the four lenses for the ideal and simulated profiles. Finally, proof of concepts lenses were fabricated highlighting the current capabilities of TPP and further areas of research for fabrication.

Acknowledgements

Thank you Professor Chris Tuck, Professor Mark Fromhold, and Professor Ricky Wildman for giving me the opportunity to carry out this PhD and for being amazing supervisors throughout.

Thank you to my sponsors Dr Peter Raven and Dr Terry Shepherd at Malvern Optical and Dr Karl Lymer and Bob Parsley at DSTL for providing additional technical guidance, financial support, and conference opportunities. Thank you Terry for your help with the spokes derivation.

Thank you to Dr Richard Cousins at the Nanoscale and Microscale Research Centre for expediting my re-training after lock down so that I could get the line width data I needed.

Thank you to "The Marks", Mark East and Mark Hardy, our patient lab technicians, who were always on hand when kit broke or I was confused.

Thank you to the TPP working group for sharing ideas. Thank you especially to Dr Robert Owen for keeping us organised with the rotas and ordering consumables, thank you to Dr Jisun Im for providing me with the silanized slides, and thank you Alice Konta for sharing ideas, print files, and laughs.

To all on the CDT, cheers to us! To my Texas road-trip buddies, thank you for making our first conference and the extended holiday a wonderful experience. To Chris Strong, thanks for being a great desk buddy.

A massive thank you to Lunch Club for being amazing friends and providing a wonderful support network as we all navigated completing our PhDs. A special shout out to Katie Blake, Liz Birchall, and Andrew Dickins for being gracious rubber duckies and top-tier meme providers.

To my amazing ex-housemate, Charlotte Henshaw, thank you for all of the kitchen singing and dancing sessions, for mac & cheese nights, and for being an all around amazing human. And to Rachel Jeffree, our honorary housemate, for being equally as crazy and wonderful.

Thank you to Canvas Nottingham for providing free-food and fun nights, I'm still so grateful you chose Nottingham to set up a second home. To Christine Barber, thank you for our chats and your endless support and friendship.

Thank you to Matt Hopwood for being my resident mathematician when the circle maths got too much, and for the general sanity checks along the way.

A big thank you to Louise Wells, for being a great friend and physics buddy, for always being at the other end of our fabulous messenger chat, and for just being you. And a special thank you to Mary and Robert Wells for providing a second home from home, I hope I have more free time to use it now.

Thank you to my family, especially my uncle for ferrying me to and from university during undergraduate, without you the road here would have been much more stressful.

To my loving partner Macauley Henchliffe, thank you for putting up with me, especially in these last three months of writing.

Finally, to my grandmother, Norma, thank you for giving me every opportunity you could to get me here. I will be forever grateful for everything you've given me.

Publications

Journal Papers

M. Askari, D. A. Hutchins, P. J. Thomas, L. Astolfi, R. L.Watson, M. Abdi, M. Ricci, S. Laureti, L. Nie, S. Freear, R. Wildman, C. Tuck, M. Clarke, E. Woods, and A. T. Clare, "Additive manufacturing of metamaterials: A review," *Additive Manufacturing*, vol. 36, p. 101562, 2020.

Conference Proceedings

E. Woods, M. Fromhold, R. Wildman, and C. Tuck, "Investigating the Production of Gradient Index Optics by Modulating Two-Photon Polymerisation Fabrication Parameters," in *Proceedings of the 30th Annual International Solid Freeform Fabrication Symposium*, (Texas), p. 2338, 2019.

E. Woods, M. Fromhold, R. Wildman, and C. Tuck, "Modulating two-photon polymerisation fabrication parameters towards the production of gradient index optics," in *2019 IEEE Research and Applications of Photonics in Defense Conference, RAPID 2019 - Proceedings*, 2019.

E. Woods, R. Wildman, M. Fromhold, and C. Tuck, "Analytical Design of Additively Manufactured Focusing Metamaterial," *2020 IEEE Photonics Conference, IPC 2020 - Proceedings*, 2020.

Conference Presentations

E. Woods "Design and Fabrication of an Additively Manufactured Infrared Metamaterial", Defense Materials Forum, UK Online, 2021.

Conference Poster Presentations

E. Woods, M. Fromhold, R. Wildman, and C. Tuck, "Metamaterial Lenses Fabricated via Additive Manufacturing", Operating in the Future Electromagnetic Environment (OFEME), London, 2021

List of Figures

List of Tables

Glossary

ALD	Atomic Layer Deposition.
AM	Additive Manufacturing.
AOM	Acousto-Optic Modulator.
CVD	Chemical Vapour Deposition.
DOE	diffractive optical element.
EBL	Electron Beam Lithography.
EM	Electromagnetic.
EMT	Effective Medium Theory.
FDTD	Finite-Difference Time-Domain.
FEM	Finite-Element Methods.
FIB	Focused-Ion Beam.
FTIR	Fourier Transform Infrared Spectroscopy.
GRIN	Gradient Index.
GWL	General Writing Language.

LIT	Laser Induced Transfer.
LP	Laser Power.
MGT	Maxwell-Garnett theory.
MLA	Microlens Array.
MoM	Method of Moments.
NIR	Near-infrared.
PBCs	Periodic Boundary Conditions.
PC	Photonic Crystal.
PI	Photo Initiator.
PMLs	Perfectly Matched Layers.
RI	Refractive Index.
SEM	Scanning Electron Microscopy.
SRR	Split Ring Resonators.
SS	Scan Speed.
STED	Stimulated Emission Depletion.
TPA	Two-photon Absorption.
TPP	Two-photon Polymerisation.
UC	Unit Cell.

Contents

Chapter 1

Introduction

1.1 Motivation

One of the prime tools use by scientists for centuries is the optical lens. A curved surface will focus light in a way dictated by its refractive index (RI), and as such their operation is well understood. However, in the hunt for arbitrary control of electromagnetic radiation, new approaches to optics are being discovered; one such discovery is that of the metamaterial [1].

Metamaterials are deliberately designed structures that result in electromagnetic properties that are derived from the structure geometry rather than their constituent materials alone [2]. The most widely known metamaterial response is that of the negative RI whereby for a finite range of frequencies both the permittivity (ε) and permeability (μ) are negative. This property resulted in the demonstration of “superlensing” [3]. In general, metamaterials consist of repeated unit cells resulting in a homogeneous averaged electromagnetic response. It is possible, however, to create spatially varying electromagnetic properties by introducing variations within each unit cell [2]. In this way gradient index (GRIN) metamaterials are presented as an approach to developing GRIN optics.

GRIN optics as a subject dates from the 1850s and can be used in applications including lensing and filtering [4]. By having an RI gradient that decreases radially from the centre to the outer edge of an optical element, light can be focused in much the same way as a conventional convex lens [5]. However, unlike conventional lenses, GRIN lenses are flat leading to a reduction in spherical aberrations which decreases coupling losses, whilst also saving space and allowing more compact optical systems [6]. GRIN lenses for optical applications are currently limited in performance and design by available manufacturing capabilities. By introducing metamaterial GRIN lenses a wider array of fabrication technologies become available. In particular the additive manufacturing technique two-photon polymerisation (TPP) is an interesting and valuable alternative.

TPP is a micro-structuring technique that draws structures in a photocurable resin using a tightly focused laser. By focusing and ultrashort pulse excitation, a high power density is achieved allowing polymerisation within regions smaller than the diffraction limit. TPP allows the fabrication of structures of arbitrary geometry, since the cured photopolymer is supported by the polymer bulk, with feature sizes close to 100 nm [7].

The contribution to knowledge of this thesis has been to show the novel manufacture of graded index metamaterial lenses from two-photon polymerisation.

1.2 Aims and Objectives

The aim of this work was to produce a metamaterial GRIN lens to operate in the short wave infrared waveband (1 μm - 2 μm). They key areas of this work are to understand the feature size and geometry limitations of a commercial TPP system, to understand how altering unit cell size and geometry change the resulting effective refractive index of a metamaterial, and to investigate how the RI profile will affect the focal length of the resulting lens.

This work can be broken down into three main tasks with their own objectives:

1. Two-Photon Polymerisation Characterisation:
   - Measure the line widths of different laser doses using TPP to formulate a catalogue of achievable feature sizes.
   - Investigate geometry changes using TPP processing parameters.
2. Metamaterial Unit Cell Characterisation:
   - Conduct analytical calculations using effective medium theory to estimate the metamaterial RI.
   - Conduct computational simulations for selected unit cells to compare to analytical results.
3. GRIN Lens Design:
   - Predict the focal length of the lens using analytical equation.
   - Conduct computational simulations to understand how the ideal vs computational RI profile affects the focal length.
   - Print proof of concept lenses to understand further fabrication considerations.

1.3 Thesis Outline

This thesis discusses all work relating to designing and creating a metamaterial gradient index lens using two-photon polymerisation. The outline of the thesis is as follows:

Chapter 2 discusses the literature relevant to the three topics of this work. In section 2.1, gradient index optics are discussed including what they are, what they are used for and traditional fabrication methods. Section 2.2 discusses what metamaterials are and how they are used, their working principles and how they are fabricated. Two-photon polymerisation is discussed in section 2.3. This includes applications of TPP, the working principles, and important considerations when using TPP for metamaterial fabrication.

Chapter 3, the feature sizes of a commercial resin IP-L are measured for different TPP laser doses. A dose test is performed to find the workable range of the resin. A common test pattern called an ascending scan array are used to measure the line widths by fabricating the arrays at different laser doses. The line widths measured from SEM images using image analysis software (ImageJ). Finally, the data is fit to the theoretical equation for line width against laser power found in the literature.

Chapter 4 looks at the limitations of fabricating with TPP. Here, the structural fidelity and adhesion to the substrate is investigated, as well as larger area printing. In addition, structures are made by tuning the processing parameters across the structure in order to create a spatial feature size gradient. The chapter finishes by presenting the cylindrical fishnet structure that was used as the metamaterial lens in this work.

Chapter 5 investigates the effective refractive index of the metamaterial unit cells of different geometries. Analytical calculations are presented for the cylindrical fishnet structure from which 4 lenses are designed. Select unit cells are taken forward based on the analytical results, and computational simulations are undertaken. The chapter also provides detailed information about the parameter retrieval method used to convert from simulated data to the effective RI.

In chapter 6, the results from chapter 5 are used to investigate the focal length of the resulting lens. Analytical calculations are undertaken, followed by computational simulations of the ideal and simulated RI profiles. Proof of concept lenses are printed and further fabrication considerations are presented.

Finally, chapter 7 outlines the achievements and contributions of this work in the context of current research, and suggests future work to be undertaken to further advance this research.

Chapter 2

Literature Review

2.1 Gradient Index Optics

Gradient index (GRIN) is a term used to describe an inhomogeneous medium with a spatially varying refractive index (RI) [8]. This causes light to propagate along a curved path as opposed to the rectilinear paths taken in conventional homogeous materials [9] which is demonstrated in the diagram in figure 2.1. By choosing an appropriate RI profile, GRIN media will act in the same manner as conventional optical components such as lenses or a prism. Naturally occurring GRIN media exist where examples include that of the human eye and the earth's atmosphere. In the latter case, changes in air density due to altitude or heat result in natural light bending phenomenon such as the mirage [8].

The field of GRIN optics has been studied for over 150 years and many different analytic solutions have been published in this time [10]. One classic example is that of James Clerk Maxwell's fisheye lens. In 1850, Maxwell presented a spherically symmetric material with a varying RI given by,

$$n(r) = a/(b^2 + r^2), \tag{2.1}$$

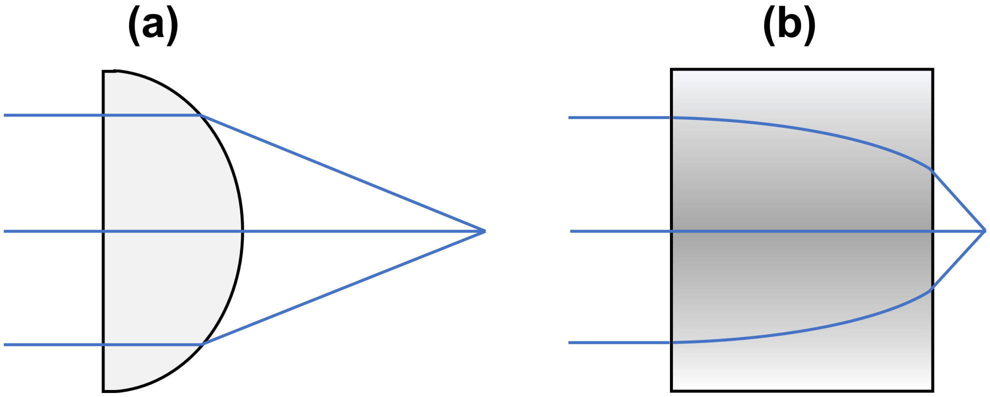

Figure 2.1: A diagram representing (a) the rectilinear ray paths in a plano-convex lens and (b) the curved ray paths in a GRIN lens. Focal points and colour gradients are not to scale.

where a and b are constants and r is the radial distance.

Maxwell used geometrical optics to show that the ray paths through the material are circles allowing perfect imaging between conjugate points on the surface of the sphere [11]. While this example uses a continuous medium between the object and image, Luneburg modified the system to allow for discontinuities in the RI [12]. This spherically symmetric structure performs perfect imaging between two given concentric spheres. In the classical Luneburg lens, any parallel rays passing through the lens will converge at a point located on the surface of the lens. This is of particular importance for applications such as integrated optics [8].

Another important analytic solution is that of the hyperbolic secant (sech) profile presented by Fletcher in 1954 [13]. A radial RI profile given by,

$$n(r) = n_0 \operatorname{sech}\left(r/\alpha\right), \tag{2.2}$$

produces sinusoidal rays for paths in the meridional plane such that repeated focal points are produced along the optical axis. Once again r is the radial distance, α is the gradient constant, and n_0 is the RI at the centre. Wood showed these sinusoidal paths experimentally in [14]. This result is of particular importance for commercial applications and is the basis of the self-focusing lenses that are widely used within science and technology.

2.1.1 RI Profiles & Applications

There are three basic types of GRIN profiles as illustrated in figure 2.2; spherical, axial, and radial. Spherical gradients, such as the Maxwell fisheye and Luneburg lenses, have a symmetric RI around a point such that isoindicial surfaces are concentric spheres. The equations governing ray propagation through spherical GRIN media are similar to those for geodesic lenses [8].

Axial gradients have RIs that vary along the optical axis with only a small amount of optical bending. Such gradients allow for the correction of monochromatic aberrations rather than adding power to the lens. Sands showed that using an axial gradient is equivalent to using an aspheric to correct for aberrations [15]. The main difference between aspheric surfaces and axial gradients is that by using axial gradients the spherochromatism of the lens can be modified due to the RI profile varying with wavelength. The spherochromatism can be increased or decreased, depending upon the dispersion of the GRIN material, independent of the monochromatic correction [9]. A number of lens designs have made use of axial gradients, however the chromatic variation of the gradient produces an advantage for photographic objectives and so, much of the work has focused on this [16, 17].

Radial gradients also allow for aberration correction in addition to being able to modify the focal length. Achromatized singlets with flat surfaces can be created due to the effects the dispersion of the GRIN material has on the paraxial chromatic aberration. In addition, colour-corrected lenses can be created by using GRIN media with curved surfaces [9]. Commercially, the flat GRIN lens is an important example as there are a diverse range of applications. GRIN rod lens arrays are used within the photocopying indus-

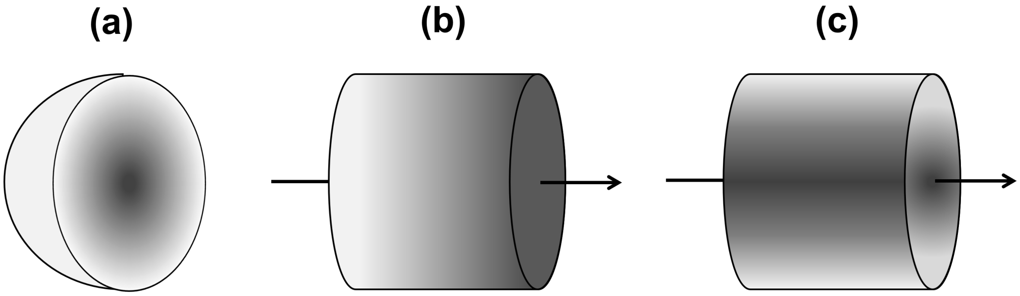

Figure 2.2: A diagram representing the types of gradient index lenses where is (a) spherical refractive index distribution decreasing from the core to the outer edge (as in Maxwell's fish-eye and Luneberg lenses), (b) axial refractive index distribution varying along the optical axis, and (c) radial refractive index distribution decreasing from the centre to the outer edge (as in the Wood lens). Colour gradients are not to scale.

try [18], GRIN lenses can be used in medical endoscopes [19], they are used to focus light when writing to and reading from CD systems [20]. They are also used in optical sensing where intensity-modulated fibre-optic sensors employ GRIN lenses for improved coupling efficiency [21]. GRIN lenses are useful for on- and off-axis imaging, collimation, and focusing which are important for communications systems [8].

2.1.2 Fabrication Techniques & Limitations

GRIN optics are usually made from glasses or polymers and while there are numerous fabrication techniques for these materials, the two important features of any technique are the depth of the gradient and the magnitude of the RI change (Δn) [4]. For GRIN glasses, the most common technique is the ion exchange process [9]. Gradients are created by placing a glass containing a single valence ion into a molten salt bath, containing a different ion to that in the glass, at temperatures between 400°C to 600°C. Over the course of a few days the ions in the bath diffuse into the glass and exchange an ion of equal valence. The resulting GRIN profiles are limited in shape and depth ($\sim$10 mm) creating Δn of $\sim$0.04, in addition, they suffer from large chromatic aberrations that are undesirable for radial GRIN lenses [4].

The "ion stuffing" technique can create slightly larger Δn compared to other techniques presented here. Gradients are made by using an acid to dissolve out a soluble phase of a phase separating glass leaving behind a glass sponge. This sponge is placed in a bath where ions diffuse into the material; this process is stopped after a short time leaving a gradient in the material. While ion stuffing can create gradients of $\Delta n = 0.04$ with a gradient depth of ~50 mm, only limited gradient profiles can be created [4] .

Neutron irradiation takes a boron-rich glass and bombards it with neutrons creating a change in the boron leading to the RI change. This technique requires a large number of neutrons and may not lead to a permanent gradient, also Δn is limited to 0.02 with a depth of 0.1 mm [22]. Chemical vapour deposition (CVD) has been used to create GRIN fibres for telecommunications [23]. This process creates layers of slightly varying chemical compositions of glass creating a structure of ~2 cm. This is then drawn, creating layers smaller than the wavelength of light meaning the gradient appears to be continuous but is only $\Delta n = 0.01$ across a depth of 0.1 mm.

GRIN polymer materials have been produced using two methods. The first creates a gradient by exchanging one monomer for another monomer in a partially polymerised material in much the same way as the ion exchange method [24]. The second uses partial polymerisation where the monomer is differentially changed into a polymer using a UV light source [25]. Whilst large areas of material can be produced along with arbitrary gradient profiles, once again only small gradients of Δn ~0.03 are formed [4].

While Moore [4] suggests the area of the gradient region is important, with the aim of creating GRIN components at the same length scale as conventional optics, smaller optical components lend themselves well to the modern focus of integrated and compact optical systems. However, it is clear that the above fabrication techniques are limited by the small index variations achievable as well as the lack of control of the resulting index profile. The small index variations in particular limit further miniaturisation due to the long propagation lengths needed to bring light to a focus. For this reason, interest turned to using metamaterials for the development of GRIN optics [2].

2.2 Metamaterials

Metamaterials are artificially structured materials designed to have specific material properties arising from the geometry rather than the constituent materials alone [1]. Both theoretical and experimental investigations for mechanical, acoustic and optical metamaterials have been studied at length; here the focus is that of optical metamaterials. The functional building block, or unit cell, is termed the "meta-atom" and it must have dimensions at or lower than the wavelength of incident light. With inhomogeneities at this length scale, from the perspective of the energy source, the material is macroscopically uniform meaning metamaterials are essentially materials rather than devices [26].

One of the oldest examples of a metamaterial is the Lycurgus Cup (figure 2.3). The cup was made in the 4th-century AD of ruby glass with embedded gold nanoparticles, such that it changes colour depending upon the surrounding lighting conditions [27]. This metamaterial artefact was created without a full understanding of the physics behind it, and similarly within the scientific community structures with artificial electromagnetic (EM) properties were studied before the term metamaterial was coined. Examples include the "twisted-jute" creating a chiral effect [28] and periodic arrays of metallic wires [29], spheres [30] or plates [31] that create artificial dielectrics.

There are three main papers that are considered to have laid the groundwork for modern EM metamaterials research. Veselago's paper on negative RI materials saw the first step towards the area of modern metamaterials [33]. This paper presented the requirement that both the permittivity and permeability must be negative in order to achieve negative RI; a phenomenon that would see a ray at the interface between a positive and

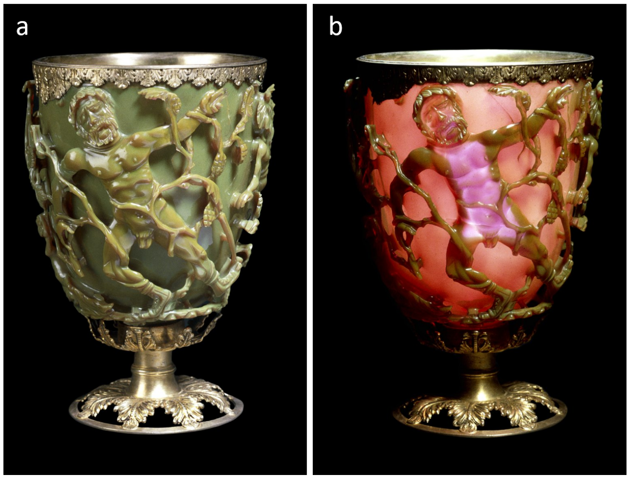

Figure 2.3: The Lycurgus Cup viewed in (a) reflected light and (b) transmitted light. Copyright the Trustees of the British Museum [32].

negative RI material refracted back in the original direction rather than continuing forward at a new angle given by Snell's law.

The existence of negative RI materials was proved experimentally by Smith et al. in 2000 [34]. They observed negative refraction at the interface of their wedge-shaped metamaterial which consisted of periodic array of copper split ring resonators (SRR) and wires. This produced a region of attenuation in scattering as shown in figure 2.4.

The gap between novel metamaterials and applications was filled by Pendry's work on perfect lenses [3]. Pendry showed that a slab of negative RI material can focus a point-like source of light to a point on the opposite side of the slab. All three of these papers presented work on negative RI materials, and many early papers focused on negative RI metamaterials working in the microwave regime due to ease of fabrication at cm/mm length scales. However, metamaterial research has since expanded far beyond this. Tailoring the shape and size of the metamaterial's unit cells, artificially tuning their composition and morphology, and placing inclusions in a predetermined manner are all ways to achieve new and exciting ways of manipulating light [1]. In particular, this has opened the door to applications such as cloaking [35], negative [36] or zero index [37] materials, in

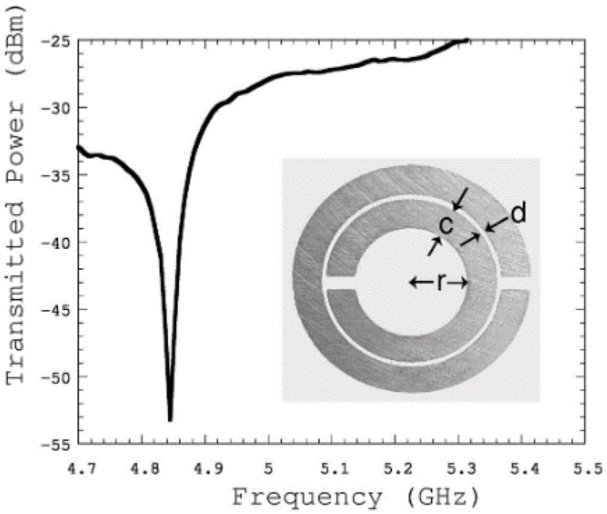

Figure 2.4: Resonance curve of a copper split ring resonator from Smith et al. [34]. Dimensions c = 0.8 mm, d = 0.2 mm, and r = 1.5 mm. The resonance region is at ∼4.845 GHz. Figure reproduced from [34].

addition to alternatives to conventional materials for optical absorbers [38], gratings [39], sensors [40], and lenses [5,41–47].

The metasurface is a widely used alternative approach for the creation of lenses. Generally, metasurface lenses are made from a spatially varying array of resonant microstructures causing a spatial gradient in their phase response [48]. This approach has enabled the design and development of aberration-free flat optics [41], and sub-wavelength imaging capabilities [42]. A theoretical demonstration by Memarzadeh et al., showed that by making small spatial adjustments to their resonant structure, they could modulate the phase lag between the structures across the device thus enabling them to focus light [43]. The Capasso group later experimentally demonstrated control over the amplitude and phase of transmitted light using a pattern of V-shaped nano-antennas [44]. Figure 2.5 shows an example array from [44] along with their experimental set up and results of testing the ordinary and anomalous refraction for six samples with different Γ (lateral period). The results show that the sample with the smallest Γ, corresponds to the largest phase gradient and the most efficient light scattering into the cross-polarized beams.

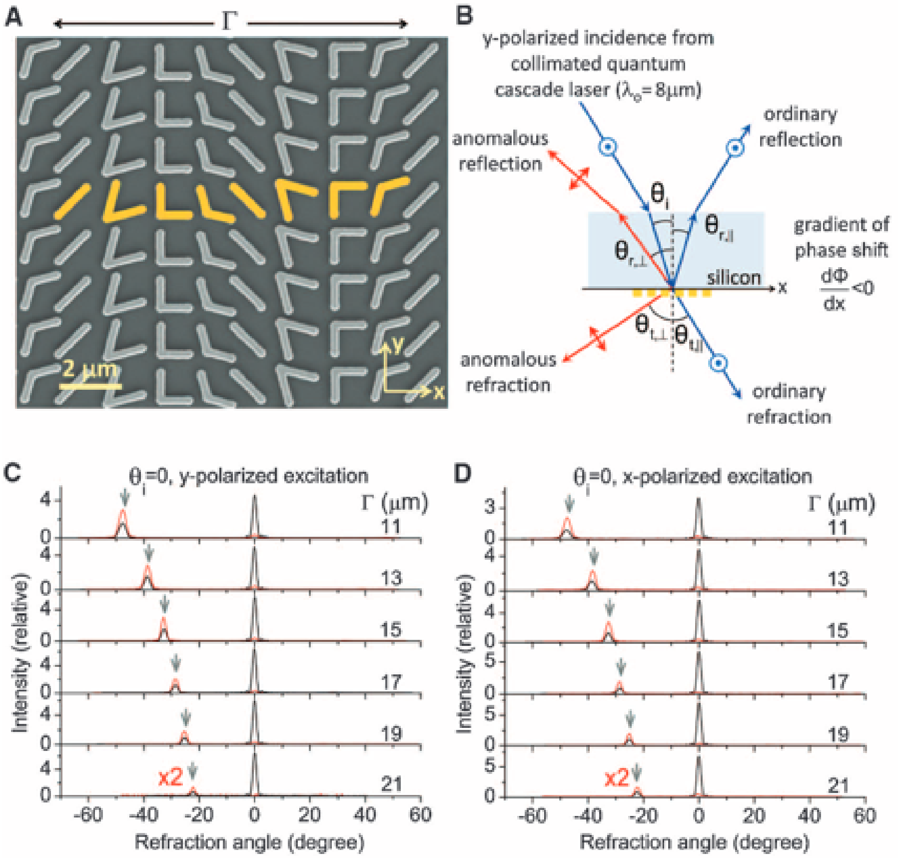

Figure 2.5: Results of V-shaped nano-antennas from Yu et al. [44]. (A) Scanning electron microscope image of an antenna array. The unit cell comprises of eight V-antennas, as indicated in yellow, with a periodicity of Γ = 11 μm in the x-direction and 1.5 μm in y. (B) Schematic experimental setup for y-polarised excitation (electric field normal to plane of incidence). (C and D) Measured far-field intensity profiles of the refracted beams for y- and x-polarised excitations respectively. The red and black curves are measured with and without a polariser for six samples of different Γ. The red curves are magnified by a factor of 2 for clarity, and the grey arrows indicate calculated angles of anomalous refraction. Figure reproduced from [44].

An alternative approach is that of the GRIN metamaterial that seeks to change the RI across the structure rather than the phase. Pinchuk et al. investigated negative GRIN materials and their ability to focus light using analytical calculations as well as finite-difference time-domain (FDTD) simulations [5]. They showed that a metallic film pierced with equidistant holes of decreasing diameter towards the edges, focused light with focal lengths dependant on the profile of the diameters. Paul et al. used arrays of annular slots with different radii to create a Δn = 1.5 gradient across their lens for an operating range of 1.2 THz to 1.4 THz [45]. Devlin et al. fabricated nano-pillar arrays of silicon rods with varying diameter and compared four different RI profiles, showing that the Luneburg profile provided a higher out-coupled intensity [46].

Interestingly, nano-pillar arrays are used in both GRIN metamaterial and metasurfaces to a similar affect, with differences in the implementation. Both Devlin [46] and Arbabi [47] create lenses by varying the diameter of silicon rods, however Devlin reduces the diameter from the centre to the outer edge, whereas Arbabi has higher and lower diameter pillars interspersed throughout the structure. One of the main drawbacks to the metasurface approach is that relying on a resonant response introduces large chromatic aberrations due to the accumulated phase dispersion of the light during propagation [49]. Whereas working in the effective regime by using GRIN metamaterials enables the creation of broadband lenses as the wavelength of interest is away from any resonances in the structure.

2.2.1 Metamaterial Working Principles

Maxwell's equations govern electromagnetic phenomena and describe the relationship between fields, sources, and material properties [50]. Microscopically, atoms are arranged in a periodic manner making up unit cells within the crystalline structure. Whilst the electromagnetic field excites local dipoles within the atoms, the induced inhomogeneous field is not felt on the macroscopic scale by the light. At this scale the detailed features and responses of the underlying structure are averaged and from this ε and μ can be calculated. The permittivity (ε) and permeability (μ) are two parameters that determine the electromagnetic properties of a material and relate to the RI by,

$$n = n' + in'' = \sqrt{\varepsilon\mu}, \tag{2.3}$$

where n' and n'' are the real and imaginary components of the RI respectively and,

$$\varepsilon = \varepsilon' + i\varepsilon'', \tag{2.4}$$

$$\mu = \mu' + i\mu''. \tag{2.5}$$

The complex component arises due to energy absorption and the phase delay between the transmittance and reflectance of the light [1]. Since the underlying inhomogeneities of metamaterials are smaller than the wavelength of interest, the EM response due to the metamaterial can also be averaged. In this case, effective parameters are dependent on the properties of the composite materials, their filling factor and overall geometry.

The two most widely used approximation theories for obtaining effective parameters are the Maxwell-Garnett theory (MGT) [51] and the Bruggeman effective medium theory (EMT) [52]. These two theories are based upon different assumptions for the composite structure and material properties. MGT assumes that inclusion particles are embedded in a host material with a low filling fraction and well defined spherical shapes. This gives rise to the equation for the effective permittivity ε as,

$$\frac{\varepsilon - \varepsilon_h}{\varepsilon + 2\varepsilon_h} = f\frac{\varepsilon_1 - \varepsilon_h}{\varepsilon_1 + 2\varepsilon_h}, \tag{2.6}$$

where ε_h and ε_1 the relative permittivity of the host medium and inclusion particles respectively, and f is the volume filling fraction [51]. When there is no clear distinction between what is the host material and what is the inclusions Bruggeman's EMT becomes useful. In this theory the two constituent materials are treated symmetrically overcoming MGT's restriction to low-f cases. In EMT, a host medium (ε_h) has two inclusions (ε_1, ε_2) dispersed within it with volume filling fractions of f_1 and f_2. For the two inclusion composite (equation 2.6) becomes,

$$\frac{\varepsilon - \varepsilon_h}{\varepsilon + 2\varepsilon_h} = f_1\frac{\varepsilon_1 - \varepsilon_h}{\varepsilon_1 + 2\varepsilon_h} + f_2\frac{\varepsilon_2 - \varepsilon_h}{\varepsilon_2 + 2\varepsilon_h}. \tag{2.7}$$

From this one can see that in a two phase composite where $f_1 + f_2 = 1$, the "host" medium is the composite material itself so setting $\varepsilon = \varepsilon_h$ the effective permittivity is given by,

$$f_1 \frac{\varepsilon_1 - \varepsilon_h}{\varepsilon_1 + 2\varepsilon_h} + f_2 \frac{\varepsilon_2 - \varepsilon_h}{\varepsilon_2 + 2\varepsilon_h} = 0, \tag{2.8}$$

which is the expression first developed by Bruggeman in 1935 [52]. Equations 2.6 and 2.8 are both just analytical approximations for effective permittivity of a composite. An approach known as the Bergman theory uses a set of spectral density functions as fit functions to correlate with the geometry of the composite [53,54]. This method calculates effective behaviour of the system and can distinguish between the influence of the geometrical structure and that of the dielectric properties of the components. However the mathematics behind this method is involved and so interested readers are referred to [53] for further reading.

These effective parameters can be experimentally retrieved in a number of ways and rely on measuring the magnitude and phase of the reflected and transmitted light through the sample. The metamaterial is considered as a uniform planar slab of material so that when illuminated by light only the reflectance R and transmittance T are considered, ignoring scattering and diffusion processes [1]. In the infrared frequency range fourier transform infrared spectroscopy (FTIR) is a useful tool for measuring T and R. This method is a fast process with a better signal-to-noise ratio compared to dispersive spectrometers. It is also important to extract phase data from the transmitted and reflected light which can be achieved using ellipsometry. This method measures the change in the polarisation state of the reflected light and is able to provide frequency-dependent phase information without using home-made apparatus [1].

Extracting the effective parameters of metamaterials from experimental data requires the determination of four variables due to ε and μ being complex quantities. Extracting these values from experimental data was first investigated in [55] which provided two equations for the RI and the impedance Z,

$$\cos(nkd) = \frac{1 - r^2 + t^2}{2t} \tag{2.9}$$

$$Z = \pm \left[\frac{(1+r)^2 - t^2}{(1-r)^2 - t^2} \right]^{\frac{1}{2}}, \tag{2.10}$$

where $k = 2\pi/\lambda_0$ is the wave vector, d is the thickness of the metamaterial layer, t is the normalised transmission coefficient and is equivalent to the conventional t multiplied by $\exp(ikd)$, and r is the complex reflection coefficient. These equations are obtained using a summation based on the Fresnel equations. Following constraints outlined in [55], the real and imaginary parts of the above equations are solved and the complex values of Z and n are obtained then, by using ε = n/Z and μ = nZ, the effective parameters are retrieved. Further considerations should be made when the metamaterial is adhered to a substrate layer so that equations 2.9 and 2.10 become,

$$\cos(nkd) = \frac{1 - r^2 + n_s t^2}{[(n_s + 1) + r(n_s - 1)]t} \tag{2.11}$$

$$Z = \frac{i[(r+1) - t\cos(nkd)]}{n_s t \sin(nkd)}, \tag{2.12}$$

where n_s is the refractive index of the substrate [1]. [56] provides a general retrieval procedure for multilayer systems which is useful for this work for measuring these parameters with the presence of a substrate.

The effective parameters can also be obtained from computational simulations of the metamaterial. Several different electromagnetic approaches are used including finite-element methods (FEM), finite-difference time-domain (FDTD) methods, and the method of moments (MoM). MoM (or boundary element method) is a frequency-domain method for performing EM simulations. It is performed by solving linear partial differential equations (PDEs) and only requires the surface to be meshed (discretised) providing a computational advantage over other methods. However, it is mostly suited to dealing with linear problems and piecewise homogeneous materials [57].

FDTD is a common method for solving EM problems that have some time dependence and works well for a wide range of frequencies and simulating non-linear materials. FDTD works by solving Maxwell's equations on a mesh and computes the electric and magnetic fields at different points on the grid. However, the time-domain discretisation introduces a numerical dispersion error affecting the simulation accuracy with a higher error accumulation over time, especially for high frequencies [57].

FEM is a popular approach to solving PDEs in general and is well suited for multiphysics problems. It involves applying a mesh to an object and approximating the solution to the governing equations of each individual element of that mesh, such that the resulting expressions give a system of algebraic equations to be solved. Unlike numerical techniques based upon finite difference or volume methods, FEM can easily capture complex geometries, particularly where boundaries have corners, at a cost of slightly more mathematical effort. In addition, since FEM is usually employed on the frequency domain and so there is no dispersion error like with FDTD [57].

There are plenty of commercial software packages available for simulating metamaterials, including COMSOL Multiphysics, CST Microwave Studio, RSoft FullWAVE, amongst others. For a review of the different solvers on the market readers are referred to [58]. Simulation results must also undergo a parameter retrieval process to convert from T and R data to Z and n; approaches for this will be discussed in detail in chapter 5.

2.2.2 Fabrication Methods

There are a number of well-established techniques used to fabricate micro/nano-structures that can be employed for fabricating optical metamaterials. Whilst photolithography is a dominant process in many industries, even the state-of-the-art 193 nm technology cannot produce the required feature sizes needed for optical metamaterial fabrication [1]. Instead of using UV light a collimated beam of X-rays can be used to pattern a resist through a mask [59]. Since the wavelength of light is much shorter, X-ray lithography has an increased lateral resolution and has produced feature sizes smaller than 30 nm [60]. However, the size of the features on the mask directly translate to the size of the pattern since X-rays cannot be focused by optics. This means in order to produce small features the mask must be equally as small. In addition the membrane of the mask must be very thin and they are made from expensive materials and so it is the cost of mask production limiting large scale metamaterial production via X-ray lithography [61].

The most widely used metamaterial fabrication technique is electron beam lithography (EBL). EBL is a maskless lithographic technique that uses a focused beam of electrons to form patterns on a photoresist [62]. This technique is widely implemented due to its high processing reliability, patterning flexibility, and high resolution enabling sub 10 nm feature sizes [36, 63, 64]. Despite being a 2D technique, EBL has been used to fabricate 3D metamaterials by creating more stacks during the EBL process. The number of stacks achievable is limited by the high aspect ratio which leads to challenges in the lift-off procedure and increased sidewall roughness [65]. Since the method is step-by-step it requires additional process development and careful alignment between the layers which increases the fabrication time making EBL a costly and low throughput technique [1, 65].

Focused-ion beam (FIB) milling can also be used to fabricate metamaterials. This technique uses a focused beam of gallium ions to sputter atoms from the surface or to implant gallium atoms into the surface. Due to its sputtering capability it is used as a micro-machining tool and with a spot size of 10 nm can be used to fabricate optical metamaterials. FIB has been used to fabricate split-ring resonators with feature sizes of 75 nm across a 16×16 μm^2 pattern (figure 2.6) in as little as 20 minutes [66].

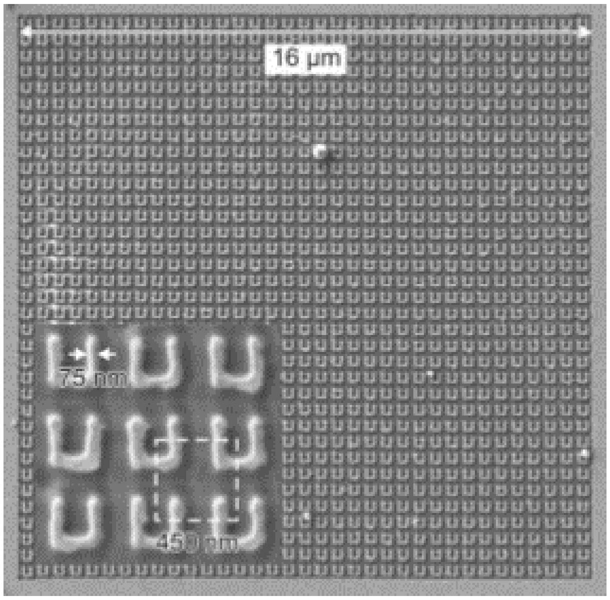

Figure 2.6: Scanning electron microscope image of array of split-ring resonators fabricated by FIB writing. Figure reproduced from [66].

FIB milling has also been used to fabricate 3D metamaterials where an alternating stack of metal and dielectric layers are evaporated onto a substrate and FIB milling used on the stack to form the pattern [26]. However, FIB milling is a destructive process and can lead to contamination of the metamaterial by the implantation of gallium ions causing deviations from the theoretical operation of the metamaterial; as such FIB is used mostly for rapid prototyping of metamaterials [1].

While EBL and FIB can be use to fabricate 3D metamaterials in the optical regime, they are limited in terms of structural height and geometrical complexity. Making full use of the novel properties provided by optical metamaterials requires a move from planar patterns to 3D nanostructures. As such, the use of additive manufacturing (AM) for metamaterials is of considerable interest, allowing control over multiple length scales, within a single step process, while exploiting new geometrical and design freedoms [67]. Of particular interest for optical metamaterials is two-photon polymerisation (TPP) as it produces nanoscale features.

2.3 Two-Photon Polymerisation

Two-photon polymerisation (TPP) is an AM technique that can be used to create structures with feature sizes around 100 nm [68]. Just like other AM techniques, TPP allows arbitrary 3D structures to be created from computer aided design (CAD) models [69]. As discussed in the previous section conventional lithographic techniques offer a higher resolution but they are limited to producing high-aspect ratio 2D structures with a relatively low throughput [68].

After Maruo's successful fabrication of 3D structures via TPP in 1997, a wide range of applications were suggested for this technology [70]. The fabrication Micro-Electro-Mechanical Systems (MEMs), by TPP has been widely investigated. Examples include microtweezers [71], microturbines [72], and optically driven pumps [73]. TPP has also been used to fabricate compact multi-lens objectives [74]. These lenses of $\sim$100 μm have resolutions of up to 500 lp mm^{-1} showing good optical quality for imaging applications such as endoscopic instruments. In [75] coupling elements were fabricated by TPP on the end of optical fibres and demonstrated coupling efficiencies up to 88% between edge-emitting lasers and single mode fibres.

TPP is also widely used to fabricate metamaterial and photonic crystal (PC) structures. The most well known pattern is the woodpile structure, as shown in figure 2.7

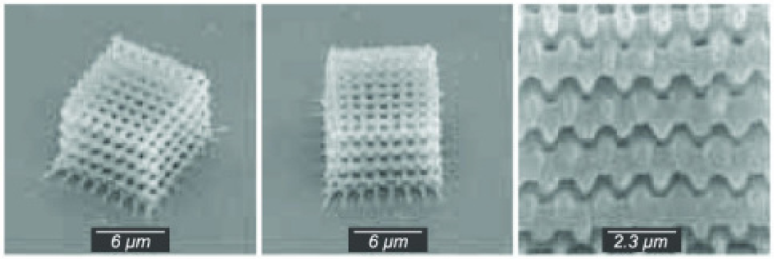

Figure 2.7: Scanning electron microscope images of TPP woodpiles fabricated in resin SU-8. Figure reproduced from [76].

which can generate optical bandgaps [76]. Yet it is structures like spiral PCs which truly highlight the design freedoms that AM provides over conventional manufacturing techniques [76, 77]. Chiral PCs are able to create bandgaps with a low RI contrast [78]. They have a higher mechanical stability than laterally disconnected structures [79], furthermore, a bi-chiral PC (figure 2.8) demonstrated lower directional dependency compared with uniaxial structures [78].

In [80], TPP is used to create voids in a positive tone photoresist which are filled with gold using electroplating. Since the RI contrast between the gold and polymer is sufficiently high there is no need to remove the photoresist. However, the structure design scope is limited to what can allow gold filling, making this technique 2.5D rather than 3D. Elongated split-ring resonators were fabricated in [81] by creating TPP scaffolds and using silver chemical vapour deposition thus creating a high quality magnetic metamaterial at the NIR frequency.

TPP GRIN lens structures have been used for infrared concentration which is an attractive solution to increase the photometric performance of sensors by concentrating the

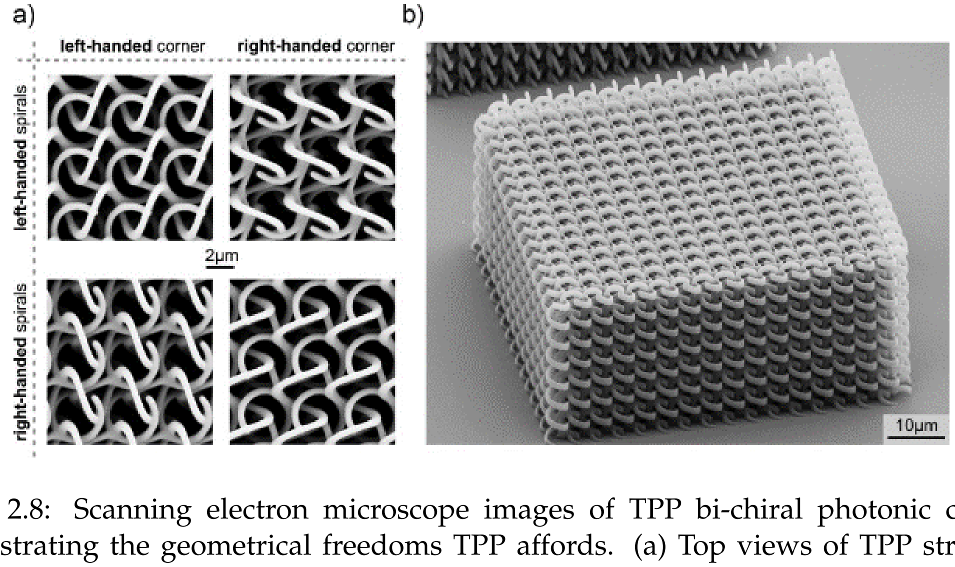

Figure 2.8: Scanning electron microscope images of TPP bi-chiral photonic crystals, demonstrating the geometrical freedoms TPP affords. (a) Top views of TPP structures with different chiral "handedness" and (b) oblique view of a right/left-handed TPP structure. Figure reproduced from [78].

light into a small area. Moughames et al. [82] fabricated a fishnet GRIN lens (volume $1.5\lambda^3$) with air gaps from $\lambda/20$ to $\lambda/8$ to concentrate mid-infrared light ($\lambda = 5$ μm). The GRIN lens, shown in figure 2.9, fabricated in this experiment achieved an intensity increase of up to 2.5 times. During this experiment, a home-made tri-acrylate polymer was used to fabricate the metamaterial structure, but they hypothesised that by using higher refractive index material like silicon, high-quality GRIN lenses could be realised.

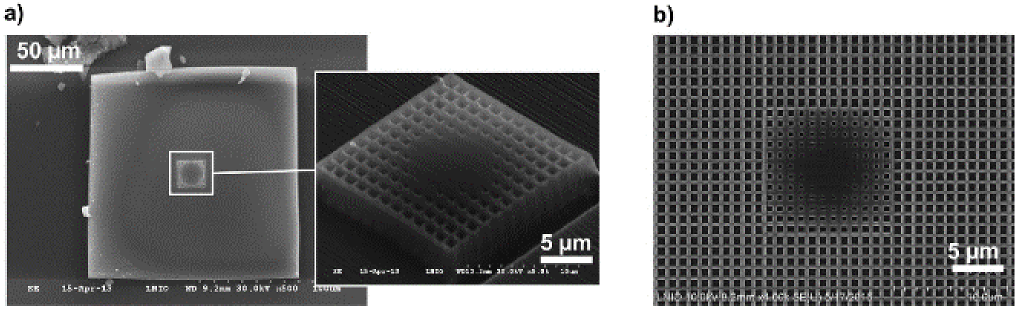

Figure 2.9: Scanning electron microscope images of metamaterial fishnet light concentrator fabricated by TPP. (a) Top view of concentrator designed for 10.4 μm wavelength integrated in a polymer block and (b) top view of concentrator designed for 5.6 μm. Figure reproduced from [82].

2.3.1 TPP Working Principles

TPP is based on photopolymerisation whereby two photons are absorbed by a photo initiator (PI) enabling the movement of an electron from its ground state to its excited state. This mechanism is known as two-photon absorption and was first described in [83]. This work numerically predicted that two photons can be absorbed through a virtual state, changing the electronic state of the atom or molecule. Two-photon absorption (TPA) is the fundamental process of TPP and is one process under the umbrella of multiphoton processes [84].

TPA works by simultaneous excitation where the first photon moves the electron to a virtual state which has a lifetime of 10^{-15} s. Only if a second photon arrives within this lifetime will it be absorbed [7]. The photons must have energy half of that of the

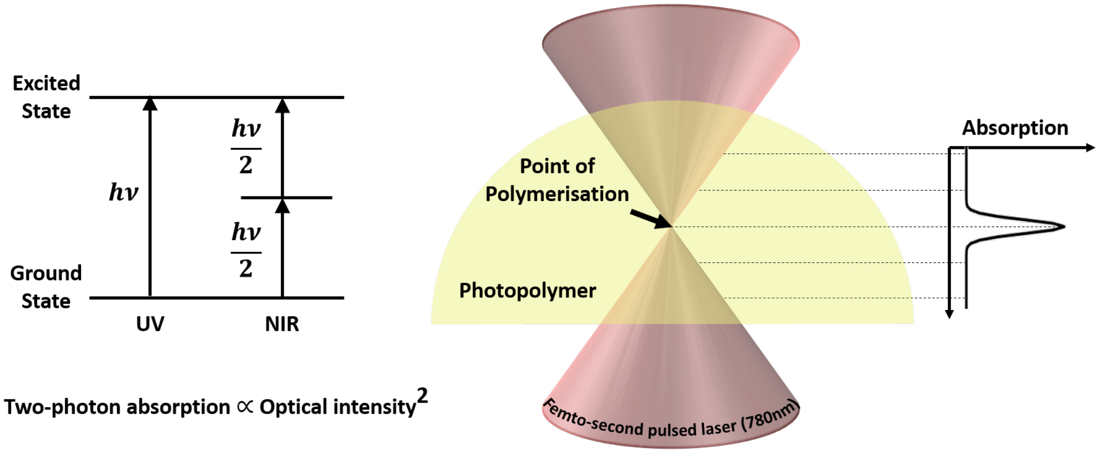

Figure 2.10: Fundamentals of two-photon polymerisation generated by a focused laser beam. Two near-IR photons are required to excite the electron from the ground to the excited state where as only one photon of UV light would be required. Lasers are pulsed to allow the two photons to arrive within 10^{-15} s. The NIR beam is focused into the polymer where curing occurs only at the focal point of the laser. TPA is non-linear and is related to the square of the laser intensity.

energy gap, corresponding to near-infrared (NIR) radiation, and light intensities must be sufficiently high to ensure the second photon arrives within the lifetime of the virtual state. Figure 2.10 shows the mechanism for TPA as compared to single photon absorption using UV light.

The development high power density monochromatic laser sources enabled the fabrication of microstructures via TPA [85]. Ti:sapphire lasers are widely used for TPP since they produce an ultrahigh peak power with short pulse widths of ∼100 fs making them capable of inducing TPA. Additionally, their central wavelength is ∼800 nm allowing easy control of the polymerisation threshold [7]. By using a high NA objective lens to focus the laser into a photocurable resin, a photon density profile is formed with constant total number of photons at every cross-section (figure 2.10). The number of absorbed photons in TPA is defined by,

$$\frac{dI}{dz} = \delta \cdot I^2, \tag{2.13}$$

where δ is the material dependent TPA cross-section and I is the incident light intensity [84]. Due to this, it is only at the focal point of the beam that the NIR light will be absorbed leading to high spatial resolution that is below the diffraction limit of the light [70]. Moreover, since the resin is transparent to NIR light, structures that are out-of-focus have little effect on the attenuation of the laser beam meaning it is not necessary to stack 2D layers making TPP a true 3D patterning technique.

When the laser is focused into a liquid-state resin, the photosensitiser chromophore used to enhance two-photon activation is excited by the absorption of two photons and then emits UV-fluorescent light. This light is then absorbed by PIs which generates radicals (initiation). These radicals then react with monomers or oligomers which go on to produce monomer radicals, which then expand in a chain reaction (propagation) until two radicals meet (termination). This process, known as free radical polymerisation, is described by,

$$initiation : S \xrightarrow{hv,hv} S^{*} \cdots \xrightarrow{I} I^{*} \to R^{\cdot} \tag{2.14}$$

$$propagation : R^{\cdot} + M \to RM^{\cdot} \xrightarrow{M} RMM \cdots \to RM_{n}^{\cdot} \tag{2.15}$$

$$termination : RM_{n}^{\cdot} + RM_{n}^{\cdot} \to RM_{n+m}R \tag{2.16}$$

which show the interactions of the photosensitiser (S), PI (I), radical ($R^{\cdot}$) and the monomer (M), where S^{*} and I^{*} are the excited states of the photosensitiser and PI respectively [7]. Cationic photopolymerisation also exists, sharing the same structure as free-radical polymerisation however the PI generates a cation as a result of energy absorption [69].

Resins used in TPP are made up of two key components which are the PI and the monomer; however other components can be introduced such as polymerisation inhibitors, solvents to assist in casting, and filler polymers to increase viscosity [86]. Initial work surrounding TPP made use of commercially available UV photopolymers such as urethane acrylates and epoxies. These photopolymers were developed for macro-scale 3D parts, and although they allow the precise fabrication of microstructures, they are unsuitable for photonics applications due to insufficient mechanical and chemical properties. Therefore several materials, including inorganic-organic hybric polymers, biopolymers, photoresits and hybrid polymers containing metal ions have been developed for multiphoton fabrication [70]. Details on specific developments and considerations around GRIN metamaterials will be outlined in the following subsection.

2.3.2 TPP Considerations for Metamaterials

There are several key issues and considerations surrounding the fabrication of GRIN metamaterials using TPP. Firstly, since the feature sizes need to be much smaller than the target wavelength range, often quoted betweeen $\lambda/4$ and $\lambda/10$, achieving smaller feature sizes will allow a metamaterial to operate in the visible or NIR wavelength range. Secondly, the dimensional accuracy of the structures is important since any deviation from the design will change the functionality of the device. Finally, the processing efficiency should be considered as a means of high volume, or large structure fabrication since the metamaterials fabricated may need to be several mm in overall size (10^6 times larger than the feature size). These areas can be improved by looking at the TPP process or by altering the materials used in fabrication.

Resolution & feature size

A lot of research has been undertaken to improve the resolution of TPP due to competition with other high resolution nanofabrication processes such as EBL and FIB lithography [87]. Resolution is often used interchangeably with “feature size” in the literature; formally the resolution is the minimum spacing of two adjacent yet separated structures, and feature size refers to the size of isolated structures [88]. Whilst both play an important role in the fabrication of metamaterials, this section will mostly focus on reducing the feature size.

The feature sizes of TPP depend upon the voxel (3D pixel) dimensions which are dictated by both the laser spot shape and material parameters. The following equations are derived from Gaussian optics,

$$D = \omega_0 \sqrt{\ln\left(\frac{I_0^2 t\beta\tau\nu}{I_{th}}\right)} \tag{2.17}$$

$$L = \frac{2z_R}{n}\sqrt{\exp\left[\frac{1}{2}\left(\frac{D\cdot NA}{\lambda}\right)^2\right] - 1}, \tag{2.18}$$

where D is the voxel diameter in the horizontal plane and L is the voxel height. I_0 is the intensity at the focal point center, t is the exposure time, β is the material sensitivity/reactivity coefficient, τ is the laser pulse duration, ν is the repetition rate, I_{th} is the threshold intensity, n is the RI and z_R is the Rayleigh length [89]. Finally, ω_0 is the beam waist given by,

$$\omega_0 = 0.61\frac{\lambda}{NA}\sqrt{\frac{\ln 2}{2}}, \tag{2.19}$$

where λ is the wavelength of the laser light, NA is the numerical aperture of the objective lens as defined in [90].

Equations 2.17 and 2.18 show that the voxel dimensions can be minimised by optimising the laser dose, i.e. laser scan speed and power, however this has an often quoted limitation of 100 nm [87]. Despite this, sub-100 nm structures have been achieved by changing certain material properties, as suggested by the β term in the above equations. For instance highly sensitive PIs can be used to lower the threshold intensity and exposure time necessary for polymerisation. A lower intensity threshold decreases the region of initial radical generation, and a short exposure time decreases the number and diffusion of these radicals, both of which lead to smaller voxel dimensions [87]. This method has been used to demonstrate lateral sizes of 80 nm [91].

Radical quenchers have also been introduced into photo curable resins which have enabled voxel sizes down to 65 nm [92] and line patterns of 95 nm wide [93]. It is important to note that this method could result in an increase in laser threshold which contributes to larger voxel sizes. Additionally, an increase in radical quenchers could result in shorter polymer chain lengths leading to structures with a low molecular weight. This affects the mechanical strength of the structure and could lead to distortions during development [93]. Any distortions would affect the optical quality of a metamaterial and so this method of feature size reduction may be undesirable in metamaterial fabrication.

Another way to improve the resolution is to use metal-polymer nanocomposites which are processed through simultaneous polymerisation and reduction. In [94] line widths of 78 nm were achieved by adding gold salt to PETA resin. It is thought that the energy required for gold salt reduction lowers the effective energy available for polymerisation thus narrowing the portion of the laser beam that is above the polymersiation threshold [95]. However, the addition of metal-salts will change the optical properties of the resin, and in particular its RI [96]. Understanding how the RI of the resin is altered is paramount to the effective design of any metamaterials using these nanocomposites.

As a final consideration, voxel size can be reduced by altering the TPP set up and introducing additional processing techniques. Once such technique is to couple TPP with stimulated emission depletion (STED) microscopy. In STED, molecules in the excited state are brought back to the ground state through stimulated emission. STED-lithography systems, such as that shown in figure 2.11, use two lasers to write a structure [84].

A pulsed excitation laser excites the PIs for polymerisation, in the same way as for TPP, and a second deactivation laser locally inhibits the polymerisation ability of the PIs by forcing energy emission. The deactivation laser is shaped using a phase plate to change the Gaussian distribution to a donut-shaped mode which has zero intensity along the optical axis. By overlapping the two lasers, polymerisation can be restricted to only the central region of the excitation laser spot thus reducing the voxel size further [97]. Using

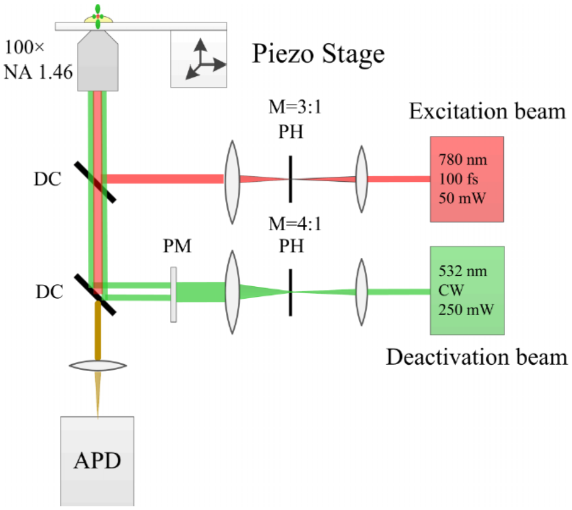

Figure 2.11: Example set up of STED-lithography using two lasers: TPA at 780 nm and depletion at 532 nm. PH are pin holes for mode purification, PM is a 2π spiral phase plate to create a donut beam, APD is an avalance photodiode used to monitor the back-reflected beams to ensure correct beam overlap and DC are dichroic mirrors. Diagram reproduced from [84].

this method, features have been written with line widths of 65 nm for a 810 nm excitation laser [97] and 55 nm for a 780 nm excitation laser [88]; the depletion laser was 532 nm in both cases.

Dimensional accuracy

A major limitation in TPP is the polymer shrinkage exhibited during the development process. This will affect the overall geometry, so that the metamaterial may no longer work as intended. For example, deformations can prevent the formation of band gaps in PCs [84]. Sun et al. proposed a shape precompensation method to overcome the material dependent shrinkage rate, which is an experimentally measurable constant [98]. For their woodpile structures, they found a lateral linear shrinkage rate of $2\%/\mu$m which is normal to the substrate surface. This shrinkage is due to the tensile stress induced by photopolymerisation gradually being released from the substrate adhered bottom layer.

The anticipated shape and size disparity was compensated for in the structure design phase, the result of which can be seen in figure 2.12. Several papers have also demonstrated shrinkage compensation in the design phase by introducing a solid support frame around the structure perimeter leading to increased mechanical stability. In this way, lattice distortions are limited only to the boarder zones of the structure [99].

Other solutions are to develop low-shrinkage materials for use in TPP. Polymerisation shrinkage can be explained on the basis of the degree of conversion obtained in the structure which is based on the initial monomeric reactive group concentration. Therefore, lower shrinkage can be obtained by using monomers with higher molar mass and lower degrees of functionality. Introducing ethoxy groups to multifunctional monomers will reduce shrinkage as the concentration of double bonds drops significantly with in-

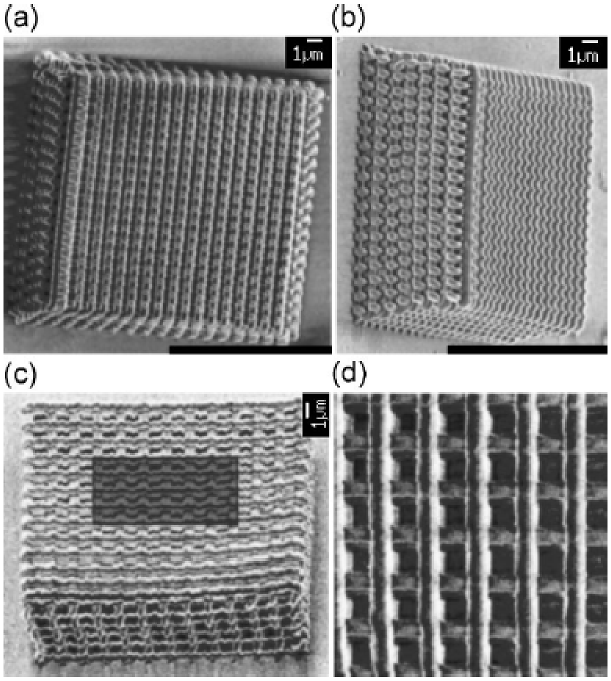

Figure 2.12: SEM images of woodpile structures where (a) has no precompensation exhibiting a shrinkage of 2%/μm and (c) showing a nearly cubic woodpile with precompensation accounting for this shrinkage. (b) and (d) show (a) and (c) respectively from different angles, where (d) is the highlighted region from (c) rotated by 90°. Image reproduced from [98].

creasing molecular weight. Additionally, methacrylates are known to shrink less than acrylates as they have a lower conversion resulting from lower reactivity and higher polymer rigidity [100]. Nonlinear Optical (NLO) silica sol-gel is a material that attracted interest due to its stability and low cost. Farsari et al. [101] used a photosensitive sol-gel material containing "NLO chromophore disperse red 1" and produced woodpile structures with very little shrinkage or distortion. This is due to the shrinkage occuring during the preparation process, so that when polymerised no molecules are released so there is very little shrinkage to cause distortion.

Altering the development procedure may also be a way to combat shrinkage. Usually the sample will be developed in solvent and then transferred to a rinsing liquid then removed and dried. However, capillary forces as the developer solvent and rinsing liquids evaporate can lead to unwanted shrinkage. In [102] instead of removing the sample from the developer, a percentage of the developer was removed and replaced by the rinsing liquid, this was repeated three times separated by a 10 minute residence time. Whilst still in the bath, the sample was exposed to UV light before being rinsed and dried. Their work found that this method reduced shrinkage from 30% to 10%, however it is a longer and more involved process than the basic development procedure.

Fabrication efficiency

The speed of TPP depends on many physical and material parameters however to provide a rough example using a commercial Nanoscribe GmbH Professional GT system, a woodpile structure of 1 mm×1 mm×20 μm with a log spacing of 1 μm and 20 layers would take approximately 30 minutes in galvo mode at a rate of 10 mm $s^{-}1$. This does not include stop/start time for the lines and movement of the stage for stitching. Whereas, if piezo mode were used it would take over 2 days [103]. Two main ways of increasing fabrication speed are through the creation of custom PIs and introducing multiple spot parallel processing.

The PI is an important component of the resin used in TPA. Several factors including its δ value, quantum yield Φ_r, initiation velocity, and solubility are important in determining how suitable the PI is for TPP. Many groups use PIs that are commercially available however there is considerable research surrounding the design and synthesis of new PIs with increased δ [70]. PIs developed with high δ tend to sacrifice Φ_r and initiation velocity values, however even if these values were to decrease by an order of magnitude, δ can be increased by several orders of magnitude through good molecular designs. Therefore, increasing δ is usually the preferred route to increasing TPP efficiency [104].

In order to increase the δ of free radical PIs, work has centred around molecules composed of a conjugated central region flanked by electron-donating (D) or -accepting (A) groups. δ values as high as 1250 GM have been synthesised using configurations such as D-π-D, D-π-A-π-D, and A-π-D-π-D where π is a conjugated bridge [105]. This value is high compared to 20 GM which is the typical value for commercial compounds [106]. Increasing δ not only speeds up the photopolymerisation process, but also allows lower laser powers to be used which is sure to increase the fabrication efficiency of TPP.

One strategy looking to improve TPP throughput is the use of a microlens array (MLA) [107]. The method uses an array of microlenses arranged in a periodic pattern on a transparent substrate which converts the collimated beam into multiple focus spots allowing parallel processing. Since the laser power is divided across several hundred spots the initial laser pulse energy is amplified to preserve the energy needed for TPP. Despite this compensation, the uniformity of laser intensity delivered across each lens needs to be addressed. Figure 2.13 shows how the voxel size changes for a single-shot exposure from the centre to outer edge of the array [107]. However, in this current form, the reduction in size from the central to the outer region could be the basis for fabricating GRIN metamaterials.

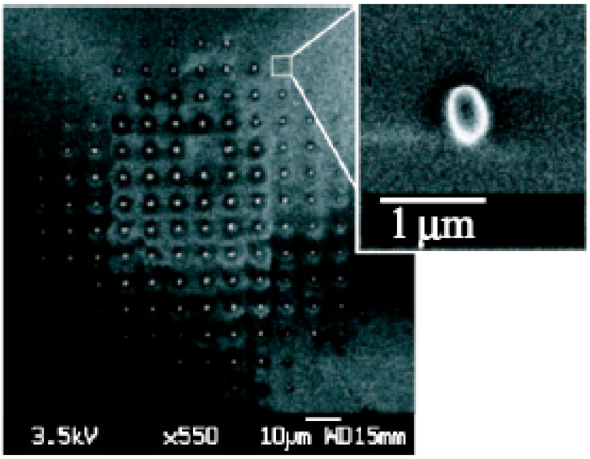

Figure 2.13: SEM images of a voxel array produced with a single shot laser dose. The pattern shows clear differences between the outer and inner voxels. Image reproduced from [107].

Material Considerations

A lot of work has focused on creating resins with higher RIs. This was driven by photonic crystal research, as in order to produce a full band gap an RI difference of 2 is needed between the material and the surrounding air [70]. Higher RI materials are also important for metamaterial structures due to the part the materials play on achievable effective parameters. A number of methods have been used to increase the RI including the development of high RI monomers [108]. A less complicated approach is to dope commercially available resins with high RI particles since by using EMT the mixture can be considered of a single materials with effective material properties [50]. Duan et al. demonstrated the generation of titanium dioxide (TiO_2) nanoparticles in the 3D structure and presence of PBG using TiO_2-doped resin [109]. However, care must be taken to use materials that are transparent at the intended wavelength of operation or if not, introduce effects useful to the operation of the metamaterial.

It is also possible to use TPP to produce a negative mould and to backfill the structure with materials of higher RI and subsequently remove the original structure [70]. Shir et al. created inverse Silicon woodpile structures by coating a TPP woodpile structure with a layer of Al_2O_3 using chemical vapour deposition (CVD) and layers of Silicon using atomic layer deposition (ALD) [110]. The polymer (SU-8) and Al_2O_3 were subsequently removed using Hydrofluoric acid resulting in an Si inverse woodpile structure which demonstrated a complete bandgap. Challenges with this method are due to the number of post-fabrication steps increasing production time, while also magnifying any distortions in the polymer structure leading to non-uniform surfaces.

Another material consideration is the ability to print multi-material structures. Metamaterials with 3 or more materials often have improved properties for the desired functionality. In [111, 112] subsequent polymerisation was used to create a network of high and low dielectric packets. Structures relating to material one are printed and developed, then the second material is deposited and further fabrication was carried out. This method suffers from low accuracy due to the multiple stages of samples alignment and development.

Efforts have also been made to fabricate metal-dielectric structures using TPP for visible metamaterials and PCs. One example being the simultaneous photopolymerisation and reduction discussed previously for line width reduction [94]. Askari [113] combined optical trapping with multi-photon polymerisation to create polymer fishnet structures with particles arranged inside the gaps. The set up can be used to position a wide number of particles provided their RI is higher than that of the photoresist. The fabrication speed is limited by the trapping force generated by the optical trap, so to increase fabrication speeds a diffractive optical element (DOE) was used to produce 7 traps in a hexagon pattern allowing an increase in fabrication speeds. The accuracy of the particle deposition is controlled by the focal spot of the polymerisation laser; by reducing the spot size less polymer is used to fix the transported particle in place reducing any movement of the particle during polymer solidification.

A hybrid TPP and laser induced transfer (LIT) system by Kuznetov et al. [114] allows high quality spherical nanoparticles to be deposited onto specific areas of a design. The particles change their shape according to the receiver structure allowing different designs to be realised. One limitation is that a femtosecond laser is used for both LIT and photopolymerisation so the LIT process cannot be done in the presence of photoresist. Therefore, this is a sequential process with increased fabrication times, but may be an acceptable compromise to be able to realise metal/polymer structures at the nanoscale. While these show promise towards multi-material TPP, all of the examples increase the already large fabrication times prohibiting large scale manufacture.

2.4 Summary & Gap In the Knowledge

Gradient index optics are important for a wide range of applications but have been limited by the technologies available to fabricate GRIN materials [8]. GRIN lenses with larger RI gradients will reduce the focal length of the component and allow further miniaturisation over conventional optics which are particularly useful for integrated optical systems. A lot of research has been undertaken to assess the use of metamaterial structures that work as GRIN optics [2]. Since metamaterials have electromagnetic properties that are controlled by the underlying geometrical structure rather than just their material constituents, the hope is to create larger RI gradients and arbitrary GRIN profiles [1].

Ordinarily, metamaterials are fabricated using techniques such as EBL and FIB milling [62, 66]. However, the geometrical design space is limited for these processes, and as such TPP is suggested an alternative to GRIN metamaterial fabrication. TPP is an AM technique capable of fabricating arbitrary 3D structures [69] and has already been used in metamaterial fabrication intended for the IR range [81, 82]. Moughames et al. showed the ability to “collect”, or focus, light with a TPP GRIN metamaterial structure, however future research would need to assess any imaging qualities of such lenses [82].

This work aims to be a comprehensive investigation into the use of TPP for creating a broadband GRIN metamaterial lens. TPP offers the geometrical flexibility that is crucial in creating the small changes in each unit cell required to create the RI gradient. Whilst there are many challenges to overcome including the minimum feature sizes and polymer shrinkage, TPP offers the ability to create micro-structured lenses with mm overall size.

2.5 Thesis Methodology

This work used a commercial TPP system (Nanoscribe GmbH Photonic Professional GT) to assess the fabrication of GRIN metamaterials using TPP. The material used is IP-L which is a proprietary Nanoscribe resin formulated specifically for polymerisation at 780 nm wavelength. This allowed the assessment of TPP GRIN metamaterials using already in the market systems and materials.

Firstly, this work looked to create a catalogue of achievable feature sizes of IP-L at different laser doses so that feature size gradients across a GRIN structure could be controled. An ascending scan test pattern [115] was fabricated at different laser doses and imaged via SEM. The images were processed in ImageJ [116] and a bounding box analysis provided the line dimensions; the resulting data was analysed using MATLAB. The results were fit to the theoretical equation (equation 2.17) presented in section 2.3.2 to discuss the ability to predict line widths for doses not experimentally tested.

Following this, work was undertaken to look at the practicalities of printing gradient structures with TPP. This included looking at ways to control shrinkage by implementing stabilising frames, and by improving structure adhesion by silanizing the glass substrates. Woodpile structures were printed with feature size gradients by altering the laser dose across the structure to understand how this affects stability. Using the information gathered, a “cylindrical fishnet” geometry was imagined for use as the metamaterial as it provided several ways to alter the geometry to produce a gradient.

Using the feature size catalogue found from the ascending scan samples, and with the cylindrical fishnet structure chosen, the next work package looked at simulating the structure to understand the RI achievable for different geometries. Analytical calculations using the Maxwell-Garnet theory [51] were undertaken where the fill fraction was based on the achievable line widths. The results were fit to four hyperbolic secant profiles that were normalised to different maximum and minimum RI values, and the closest matching unit cells along a discretised curve were selected. The selected unit cells were simulated in COMSOL for a greater understanding of how the geometry affects the RI. This provided a list of achievable effective RI values for different unit cell geometries.

Finally, using these effective RI results a simple 2D lens simulation was set up in COMSOL to understand how the RI profile, smooth verses discrete regions, affects the focal length and focal spot size of the resulting cylindrical lens. Example structures with these theoretical RI gradients were printed providing further insight into future improvements needed for printing GRIN lenses using TPP.

Chapter 3

Feature Size Characterisation

3.1 Introduction to Line Width Measurements

The aim of the work presented in this chapter is to understand the range of feature sizes obtainable for a commercial TPP resin, IP-L. The minimum feature size determines the minimum wavelength of operation for the metamaterial lens. For TPP, the feature sizes, specifically line width and height, depend on the material being used as well as the laser parameters while printing. As shown in equations 2.17 and 2.18 the laser power (LP) and scan speed (SS) have an effect on the resulting line widths and line height; the combination of these two parameters is referred to as the laser dose [7]. A dose test was undertaken to find a range of laser power and scan speed combinations that produce well polymerised structures. A test pattern was printed at each dose combination and the resulting line widths measured. This chapter also investigates the theoretical line width model based on equation 2.17 which would allow the prediction of line width for a particular dose without experimental measurements. The main outcome of this chapter is the catalogue of line width measurements which were used to design the metamaterial lens in chapter 5.

3.2 Measurement Methodology

3.2.1 Fabrication using Nanoscribe TPP System

A commercial TPP setup (Nanoscribe GmbH Photonic Professional GT) was used to fabricate the structures in this work. The system uses a 780 nm fibre laser with an 80 MHz repetition rate and 120 fs pulse duration. An oil immersion objective lens (1.4 NA, 63X, 190 μm WD) was used to focus the laser beam. Structures were written in galvo mode where the laser beam is moved relative to the sample using a high speed XY galvo-scanner and a piezo stage moves the sample in the z-direction.

The structures were designed in DeScribe, the print preparation software for the Nanoscribe, resulting in a .gwl file. Print files can be created by either importing an STL file or a design can be programmed in DeScribe using General Writing Language (GWL). The first method is useful for larger solid structures, where features are bigger than the line width, as it is sliced into layers with a set hatching distance and orientation between each scan line. However, this method falls short for creating structures from single scan lines, as lines not oriented in the direction of the scan path are split into segments breaking continuity. This work made use of GWL programming, where laser coordinate data is defined by mathematical functions, allowing for more complex designs and also giving the ability to change laser parameters across the structure.

The substrate used is a 22 mm $\times$ 22 mm glass coverslip with a thickness of 0.16 mm. The coverslip is washed in Acetone (VWR Chemicals, UK) followed by 2-propanol (Sigma-Aldrich, Dorset UK) and then blow dried in air; this is the base procedure recommended by Nanoscribe. After the substrate is prepared, it was then secured to the sample holder using tape where a drop of Zeiss Immersol^{TM} 518F was applied to the centre of one side and the IP-L resin (Nanoscribe, Germany; previously known as IP-L 780) was drop-cast on the other. This resin is a negative-tone resist optimised for TPP, and of the available resins at the start of this project it offered the smallest feature sizes of the Nanoscribe library, and the lowest shrinkage. Following this, the sample holder was placed into the Nanoscribe for writing and the previously prepared .gwl file is loaded. Post writing, samples were developed in propylene glycol monomethyl ether acetate (PGMEA; Sigma-Aldrich, Dorset UK) for 20 minutes and cleaned in 2-propanol for a further 2 minutes then blow dried in air.

Images of samples were taken using either an optical microscope (Nikon Eclipse LV100ND) or Scanning Electron Microscopy (SEM). For SEM, samples were sputter coated with 10 nm of iridium to create a conductive surface ready for imaging at 15 kV using a JEOL 7100F FEG-SEM. Files were saved in .tiff format to ensure high fidelity of the data.

3.2.2 Resin Dose Test

A dose test is performed to find the workable range of the resin (IP-L). A range of scan speeds between 10 μm s^{-1} to 100 000 μm s^{-1} were investigated, where the scan speed increased linearly over a logarithmic scale. To perform the dose test 3 arrays of woodpile structures with a rod spacing 0.9 μm and a layer offset of 0.5 μm were printed at powers between $10\% - 120\%$ in 5% intervals for each of the chosen scan speeds. The arrays were printed in different runs to account for fabrication variations resulting in an incorrect result (e.g dust in the resin causing an explosion where the dose would otherwise be fine). The resulting structures were visually inspected using SEM to find the power range for each scan speed where “good” structures were produced; specifically well-formed structures with no micro-explosions or inconsistencies.

It should be noted that the Nanoscribe system uses percentages when programming the laser power. The system is calibrated to 50 mW output at 100% power, where an acousto-optic modulator (AOM) controls the power output through the system. Powers above 100% are possible by increasing the power scaling of the machine, but there is still an upper limit which can change over time as the laser ages. Therefore, to ensure longevity power scaling was set to 1.2 in this work, allowing a maximum power of 120% or 60 mW.

3.2.3 Line Width Measurement and Analysis

Ascending Scan Test Pattern

The popular "ascending scan" method was employed to create a pattern to measure the line widths of IP-L. In this method, lines are printed with increasing offset from the substrate as demonstrated in figure 3.1. Since the laser focal point is elliptical, lines adhere to the substrate at smaller offsets but fall off at larger offsets due to the smaller surface area at the tip. Adhered lines allow the measurement of the line width, while fallen lines should fall and adhere to the surface allowing the measurement of line height.

The need for multiple lines arises from the uncertainty when finding the interface between the substrate and the resin. The Nanoscribe is set to find the interface at the

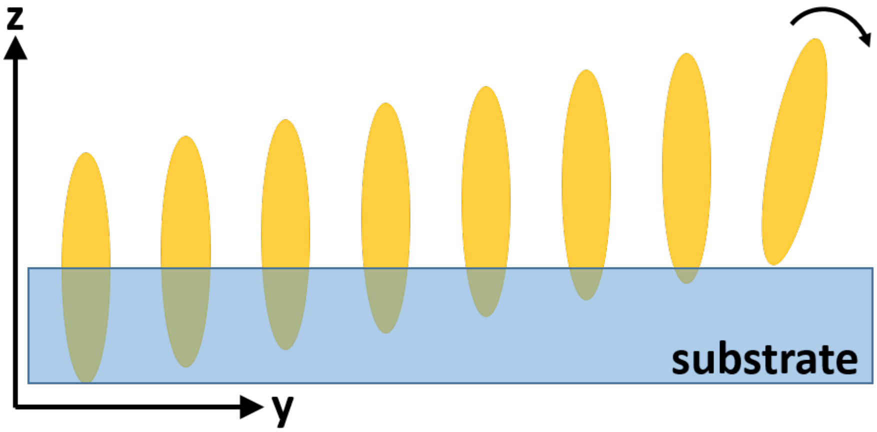

Figure 3.1: Visualisation of ascending scan array where lines are fabricated at increasing offset from the surface of the substrate. The lines are spaced 2 μm apart in the y-direction to minimise potential overlap of fallen lines.

midway point of the voxel, where it should be the thickest and therefore allow good adhesion. Increasing the offset allows for the true widest point of the voxel to be uncovered providing an accurate line width measurement. Each ascending scan set consists of 8, 2 μm long lines where the offset from the substrate is increased in 0.1 μm steps for scan speeds under 20 000 μm s^{-1}, and in 0.025 μm steps for scan speeds greater than or equal to 20 000 μm s^{-1}. This difference was to account for the shorter voxel height at the higher scan speeds as initial studies found only lines at the first offset were adhered to the substrate in this speed region.

For each of the acceptable dose combinations found in section 3.2.2, an array of lines is created by repeating the ascending scan pattern 5 times to assess repeatability within the sample. The interface was found at the start of each repeat to account for any variation in the substrate between each line set. Five samples were made in different runs and on different days to assess the run-to-run repeatability of the line widths. The samples were prepared for SEM as per section 3.2.1 and an image was taken of every array of lines across the five samples corresponding to 465 images. Images were taken across multiple days making sure a single sample was imaged in one sitting so as not to cause variations within a single data set.

Data Extraction & Analysis

The simplicity of the ascending scan arrays means line widths can be measured easily using image processing techniques in order to speed up the analysis process. ImageJ was used to extract the line width data from the SEM images of the ascending scan arrays [116]. A macro was created to batch process all ascending scan images. First the images were cropped to remove the SEM parameter information, converted to 8-bit, and a median filter with a radius of 2 was applied to remove random noise. Following this, the Huang white auto threshold was used, chosen after trying all thresholding methods within ImageJ and visually inspecting which provided consistent results across multiple images. Lines were then analysed by applying the "Oriented Bounding Box" analysis from the MorphoLibJ plugin [117], and the data was exported in .xlsx format. The full macro can be found in appendix A.

MATLAB was used for statistical analysis of the data by importing the .xlsx file. The results from the bounding box analysis provided the x and y location of the centre of each box, along with the box length and width. THe position and dimensions were output in pixels and were converted into nanometers for analysis. Images were taken at a magnification of 5500 to allow for a whole array to fit in one image; this corresponded to 17 nm per pixel. Fabricated lines had a length of 2 μm; values with a box length larger than 2.5 μm and smaller than 1.5 μm were removed from the data set and assumed to be non-line artefacts.

Lines that had fallen were removed from the data by calculating the median of the remaining lines and removing lines outside of 3 times the median average distance from the median [118]. The bounding box coordinate data was then used to sort the lines into their position on the array to enable the comparison of lines at the same z-offset. Finally, the line width for each array was taken as the mean of the row with the highest offset with as many of the 5 lines present as possible. The weighted mean and standard deviation is used to combine the line widths from each of the 5 samples, and the pooled standard deviation is used to look at variations within a single sample.

Fitting Line Width Data to Theory

An investigation into the theoretical fit of the line width vs power for each scan speed was then undertaken. Understanding the relationship between the line widths and the laser parameters is useful for predicting line widths for a particular dose without having to experimentally test that combination specifically. The following section looks to fit the experimental data to the theoretical fit given by equation 2.17, MATLAB's curve fitting toolbox was used to fit the data to the custom equation for line width given by,

$$D = \omega_0 \sqrt{\ln\left(\frac{P\tau\nu}{Sa}\right)}, \tag{3.1}$$

where ω_0 is the beam waist given by equation 2.19, P is the laser power in mW, $\tau = 100$ fs is the laser pulse duration, $\nu = 80$ MHz is the repetition rate, S is the scan speed in μm s^{-1} and a is the fitting parameter which has grouped the other parameters in equation 2.17 so that $a = \beta/I_{th}$; representing the ratio of the material coefficient and threshold intensity.

In order to avoid a complex result, and thus a failed curve fit, the following upper limit was applied to the fit,

$$a_{upper} < \frac{P\tau\nu}{S}, \tag{3.2}$$

and the lower limit was set to 0. This is physically justified since the power and speed combination must be larger than the threshold intensity in order to initiate polymerisation to begin with. The results of the individual fits were compared to a single optimised fit using the *nlinfit* function from MATLAB's Statistics and Machine Learning Toolbox.

3.3 Results

3.3.1 Dose Test Results

If the laser dose is too low, corresponding to low power and fast scan speeds, polymerisation is not (fully) initiated resulting in either no structure forming, or an inconsistent structure that is not self-supporting (figure 3.2a). Whereas, if the dose is too high (high power and slow scan speeds) micro-explosions occur in the resin (figure 3.2c). A "good" dose will result in consistent fabrication as in figure 3.2b. A dose was considered acceptable where 2 or more of the structures at a particular dose produced "good" structures.

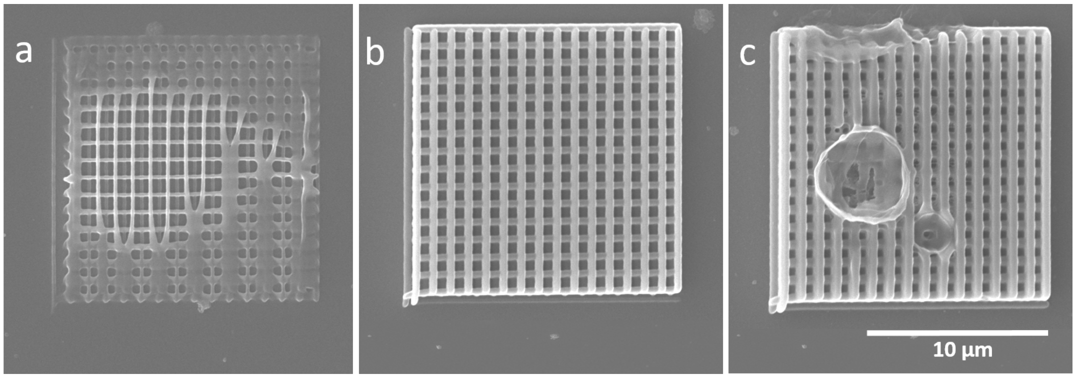

Figure 3.2: Example woodpiles printed for the dose test where (a) is underexposed demonstrating the inconsistencies, (b) is a good dose showing a well polymerised and consistent structure, and (c) is overexposed and shows remnants of micro-explosions.

Figure 3.3 shows a map of the resulting dose regions where the corresponding power in milliwatts is also shown for ease of conversion (100% = 50 mW). The blue (ticks) show the workable range of the resin; these power and speed combinations were used for the ascending scan samples and are summarised in table 3.1.

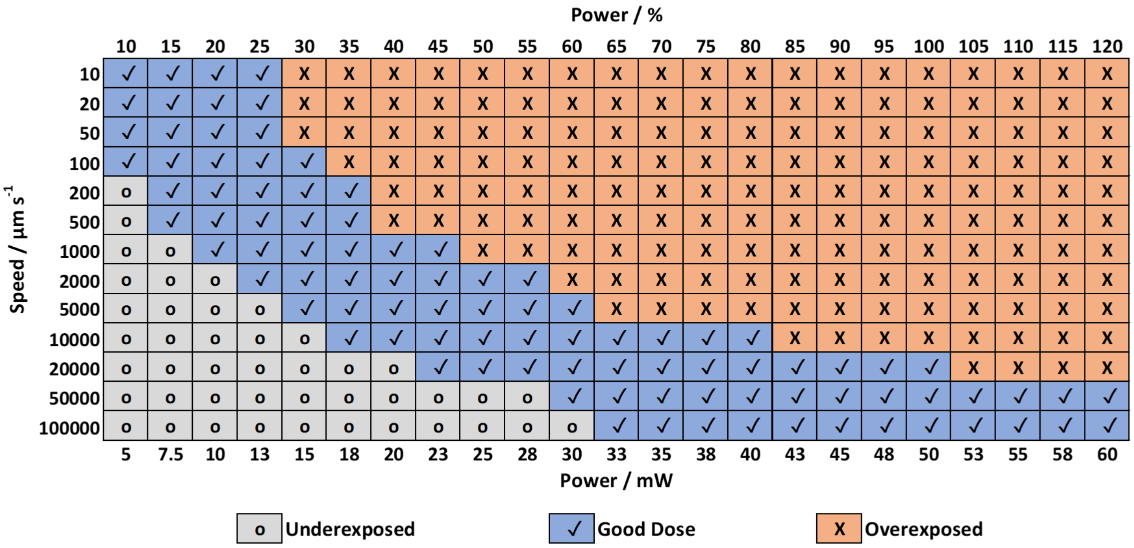

Power / %

Speed / µm s^{-1}	10	15	20	25	30	35	40	45	50	55	60	65	70	75	80	85	90	95	100	105	110	115	120
10	✓	✓	✓	✓	X	X	X	X	X	X	X	X	X	X	X	X	X	X	X	X	X	X	X
20	✓	✓	✓	✓	X	X	X	X	X	X	X	X	X	X	X	X	X	X	X	X	X	X	X
50	✓	✓	✓	✓	X	X	X	X	X	X	X	X	X	X	X	X	X	X	X	X	X	X	X
100	✓	✓	✓	✓	✓	X	X	X	X	X	X	X	X	X	X	X	X	X	X	X	X	X	X
200	o	✓	✓	✓	✓	✓	X	X	X	X	X	X	X	X	X	X	X	X	X	X	X	X	X
500	o	✓	✓	✓	✓	✓	X	X	X	X	X	X	X	X	X	X	X	X	X	X	X	X	X
1000	o	o	✓	✓	✓	✓	✓	✓	X	X	X	X	X	X	X	X	X	X	X	X	X	X	X
2000	o	o	o	✓	✓	✓	✓	✓	✓	✓	X	X	X	X	X	X	X	X	X	X	X	X	X
5000	o	o	o	o	✓	✓	✓	✓	✓	✓	✓	X	X	X	X	X	X	X	X	X	X	X	X
10000	o	o	o	o	o	✓	✓	✓	✓	✓	✓	✓	✓	✓	✓	X	X	X	X	X	X	X	X
20000	o	o	o	o	o	o	o	✓	✓	✓	✓	✓	✓	✓	✓	✓	✓	✓	✓	X	X	X	X
50000	o	o	o	o	o	o	o	o	o	o	✓	✓	✓	✓	✓	✓	✓	✓	✓	✓	✓	✓	✓
100000	o	o	o	o	o	o	o	o	o	o	o	✓	✓	✓	✓	✓	✓	✓	✓	✓	✓	✓	✓
Power / mW	5	7.5	10	13	15	18	20	23	25	28	30	33	35	38	40	43	45	48	50	53	55	58	60

o Underexposed ✓ Good Dose X Overexposed

Figure 3.3: Dose region map for IP-L resin. The grey (circles) are where underexposure occurs, the blue (ticks) are the workable doses, and the orange (crosses) represent regions of overexposure.

Table 3.1: Table showing the laser scan speeds and their corresponding laser powers producing good structures as defined from Figure 3.2. These powers cover the blue (ticks) region from Figure 3.3. Steps for the laser powers are 2.5 mW and 5% for each unit.

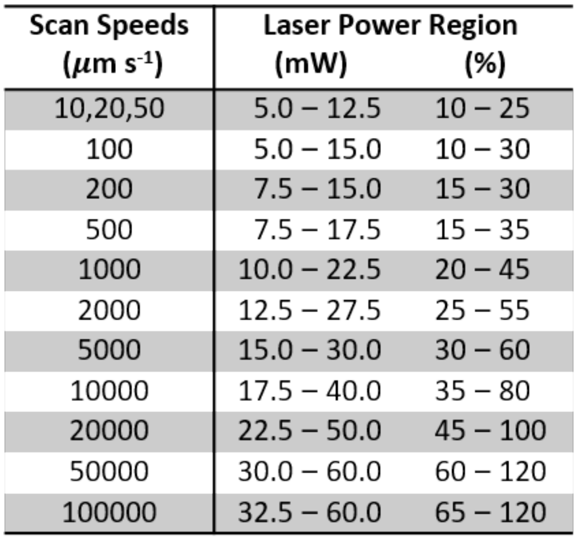

Scan Speeds (μm s^{-1})	Laser Power Region (mW)	(%)
10,20,50	5.0 – 12.5	10 – 25
100	5.0 – 15.0	10 – 30
200	7.5 – 15.0	15 – 30
500	7.5 – 17.5	15 – 35
1000	10.0 – 22.5	20 – 45
2000	12.5 – 27.5	25 – 55
5000	15.0 – 30.0	30 – 60
10000	17.5 – 40.0	35 – 80
20000	22.5 – 50.0	45 – 100
50000	30.0 – 60.0	60 – 120
100000	32.5 – 60.0	65 – 120

3.3.2 Ascending Scan Measurements

Figure 3.4a shows an SEM image of an example array (SS = 50 μm s^{-1} & LP = 7.5 mW) where each column is a repeat of the ascending scan pattern for that dose, with the z-offset increasing from the lower to the upper lines. It was intended that line heights could be measured using the lines that had fallen over. However, as shown in the image, these lines would often scatter across the substrate during the development process rather than falling in place making it difficult to measure both line width and height with any consistency. Due to this, the maximum offset was limited to 0.7 μm (0.2 μm for scan speeds $\geq$ 20 000 μm s^{-1}), corresponding to 8 lines total, to reduce the number of fallen lines scattering across the substrate, and the study was limited to measuring line widths.

An example array after image processing is shown in figure 3.4b demonstrating the results of the thresholding as well as showing the calculated bounding box around each feature. The numbers are auto-generated and provide a tag to each feature extracted by the software. These tags are not always in numerical order as they appear on the substrate and so a method was employed to sort the data into their respective position on the substrate as previously discussed in section 3.2.3.

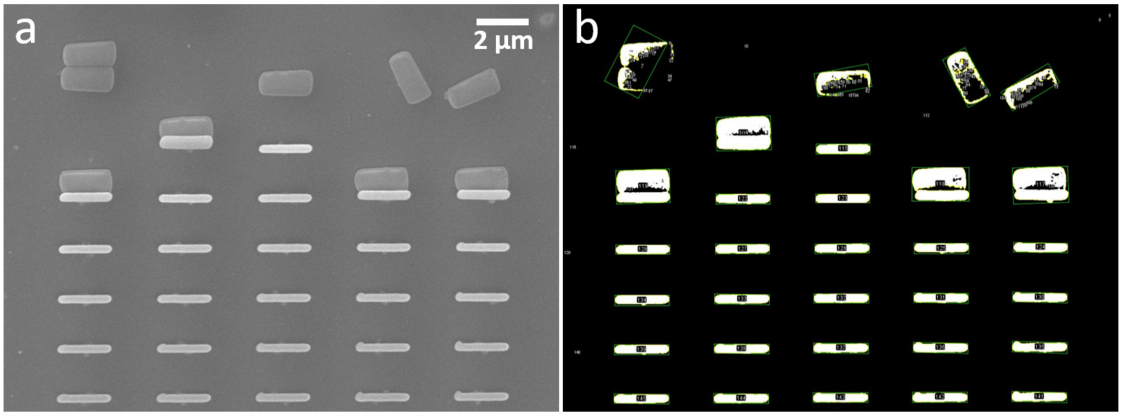

Figure 3.4: Example ascending scan array for SS = 50 μm s^{-1} & LP = 7.5 mW where (a) is the raw SEM image and (b) shows the array post image processing to the same scale. The line widths were taken as the width of the bounding boxes as shown in green.

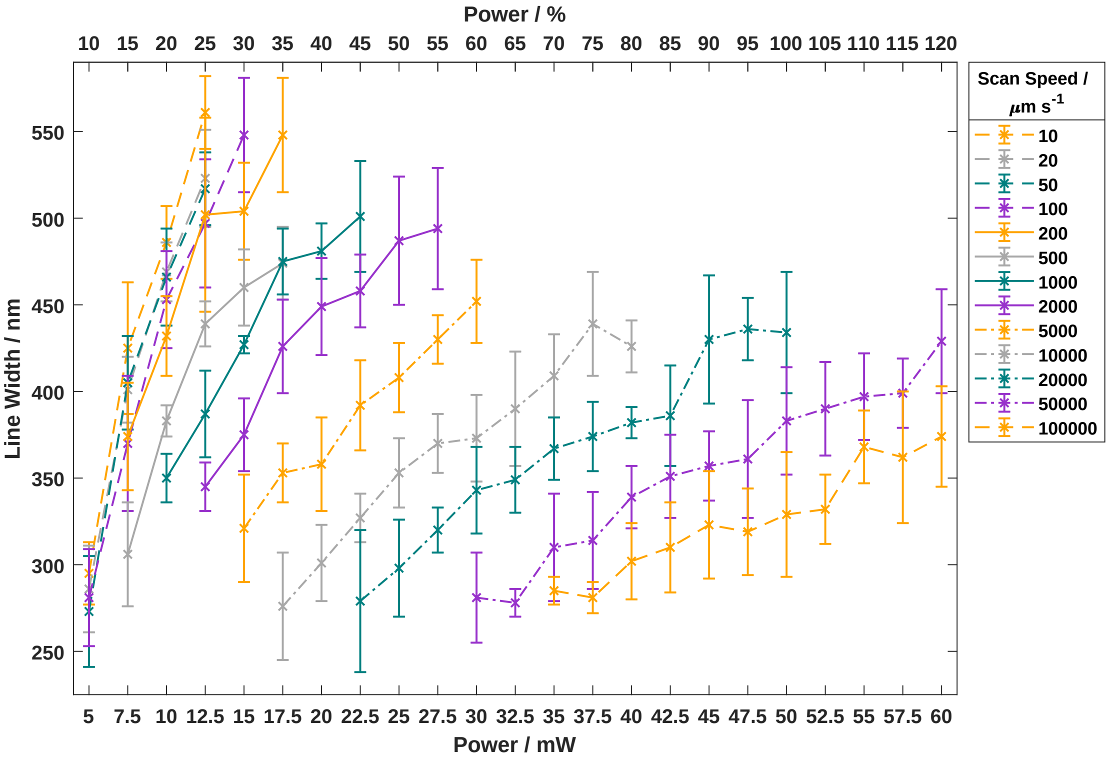

Figure 3.5: Achievable line widths for the 13 selected laser scan speeds for their respective laser power regions. The smallest line width is 273 nm ± 32 nm and the largest is 561 nm ± 21 nm. The general trend of increasing line width with increasing laser power is apparent, as well as decreasing line width with increasing scan speed. Large error bars and scattered data are due to experimental inconsistencies. Results are comparable to the study conducted by Guney et al. [115].

Figure 3.5 shows the line widths as a function of laser power for each scan speed. As expected the line width increases with increasing power and decreases with increasing scan speed; relating to increasing and decreasing laser dose respectively. The maximum line width was found to be 561 nm ± 21 nm for a dose combination of SS = 10 μm s^{-1} & LP = 12.5 mW and the minimum was 273 nm ± 32 nm for SS = 50 μm s^{-1} & LP = 5 mW. These results make up the catalogue of achievable line widths which were used in the analytical effective refractive index calculations as discussed in section 5.2.1.

It is clear from the error bars in figure 3.5 that there is generally a large uncertainty on the line width values. Table 3.2 summarises the in-run (across a single sample) and run-

Table 3.2: A table showing the pooled standard deviation of line widths for each of the five samples as well as the run-to-run variation representing the standard deviation across all five samples.

Pooled Standard Deviation (nm)					
Sample 1	Sample 2	Sample 3	Sample 4	Sample 5	Run-To-Run
18	22	10	9	16	26

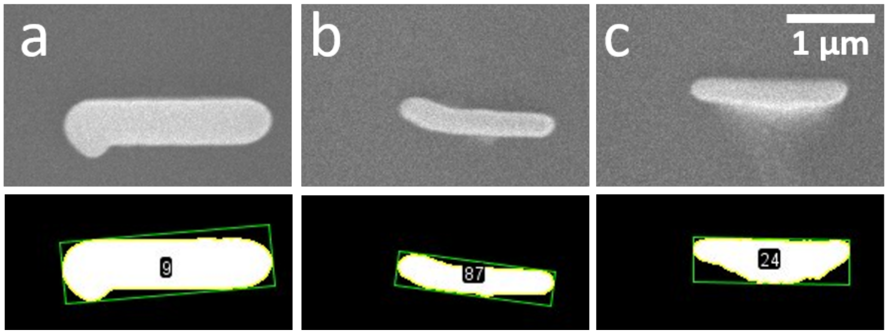

Figure 3.6: Examples of line imperfections (a) overgrowth due to laser acceleration at the left hand edge, (b) bowing where adhesion to the substrate occurs after curing and (c) debris such as dust or other particulates left over from various points in the fabrication process. In the example in (c), the line width is increased due to undissolved uncured resin in the region.

to-run (across all samples) pooled standard deviations indicating the repeatability of the results. Line imperfections, such as those demonstrated in figure 3.6 will have an effect on the line width results. In addition, daily differences in SEM set up will affect the focus of the image affecting the bounding box analysis. Figure 3.7 shows images of the same ascending scan array (SS = 10 000 μm s^{-1} & LP = 35 mW) taken on two separate occasions. The processed image for the top row of lines is shown above their respective raw images. The average width of the top row of lines was 442 nm ± 17 nm and 391 nm ± 17 nm for (a) and (b) respectively representing a 3 pixel difference.

The oriented bounding box analysis was used to measure line dimensions to account for any lines not falling perfectly along the x-axis. This is an improvement compared to using the in-built bounding box analysis in ImageJ as widths are artificially increased

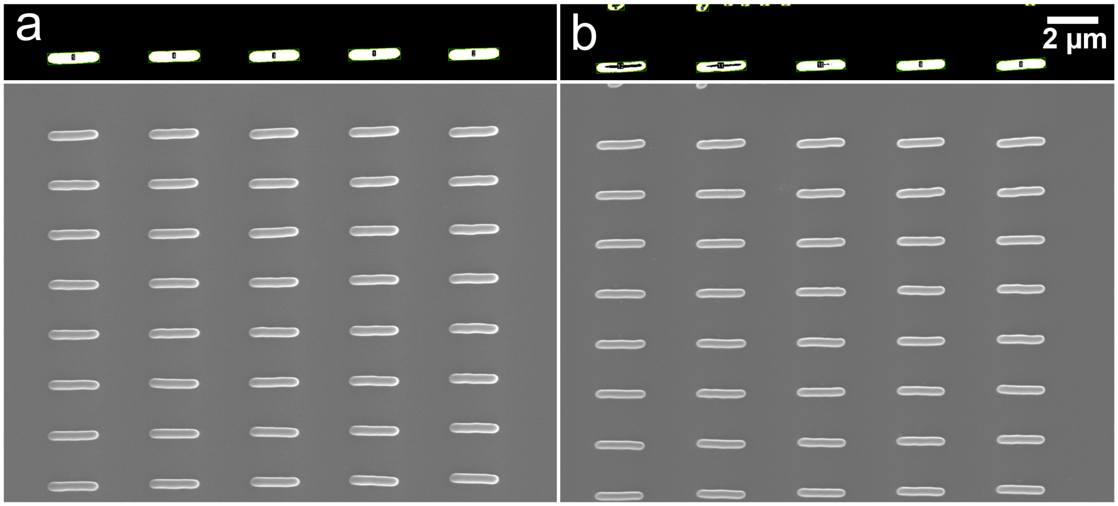

Figure 3.7: SEM images of the SS = 10 000 μm s^{-1} & LP = 35 mW array on the same sample taken on different days. The black strip shows the top row of lines for the image below after image processing.

if the line is on the diagonal. By way of example, for figure 3.7(a) using the in-built bounding box the line width average for the top row is 459 nm ± 17 nm compared to 442 nm ± 17 nm for the oriented bounding box (representing 17 nm or 1 pixel difference). For figure 3.7(b) the difference is 34 nm or 2 pixels (425 nm ± 17 nm and 391 nm ± 17 nm for in-built and oriented bounding boxes respectively). The larger difference between bounding box methods for (b) is likely due to differences in aligning the sample within the SEM itself. While the array shown here had relatively few misaligned lines other arrays were more apparent in their diagonality, whether due to alignment of the SEM image, or simply due to differences while printing.

3.3.3 Fitting Line Width Data

Figures 3.8 and 3.9 show the line width results and theoretical fit for each scan speed data set, along with their corresponding fit parameter (a) and coefficient of determination (R^2) to indicate goodness of fit. It is clear that the fits, and thus the theoretical equation, are not accurately describing the dataset. However, there seems to be an improvement in the fit with increasing scan speed shown by the increasing R^2 value.

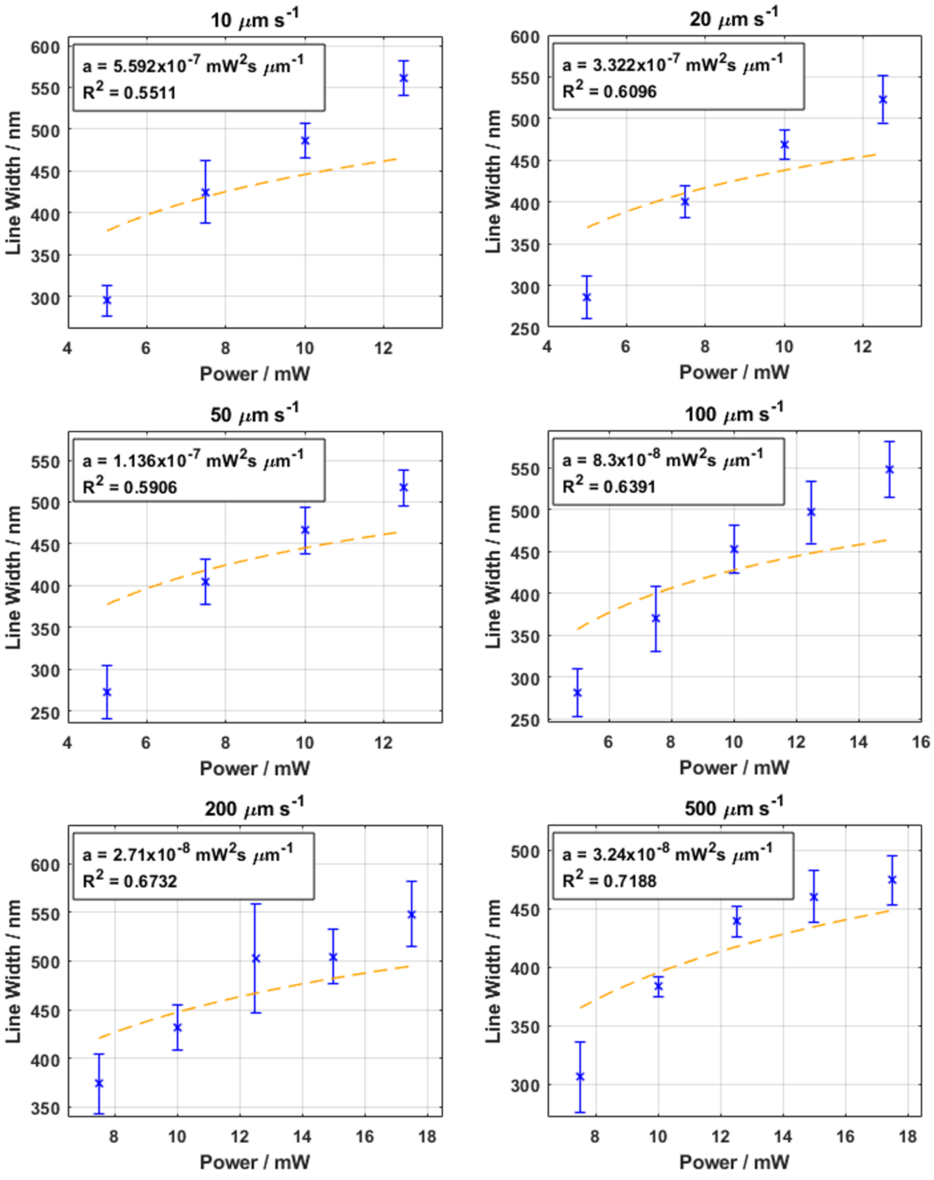

Figure 3.8: Line width against laser power with associated theoretical fit for the lowest 6 scan speeds. Annotations show fit parameter, a, and the R^2 for each of the tested scan speeds. The fit improves as the scan speed increases, although uncertainty in the line width measurements appears to be larger for higher scan speeds.

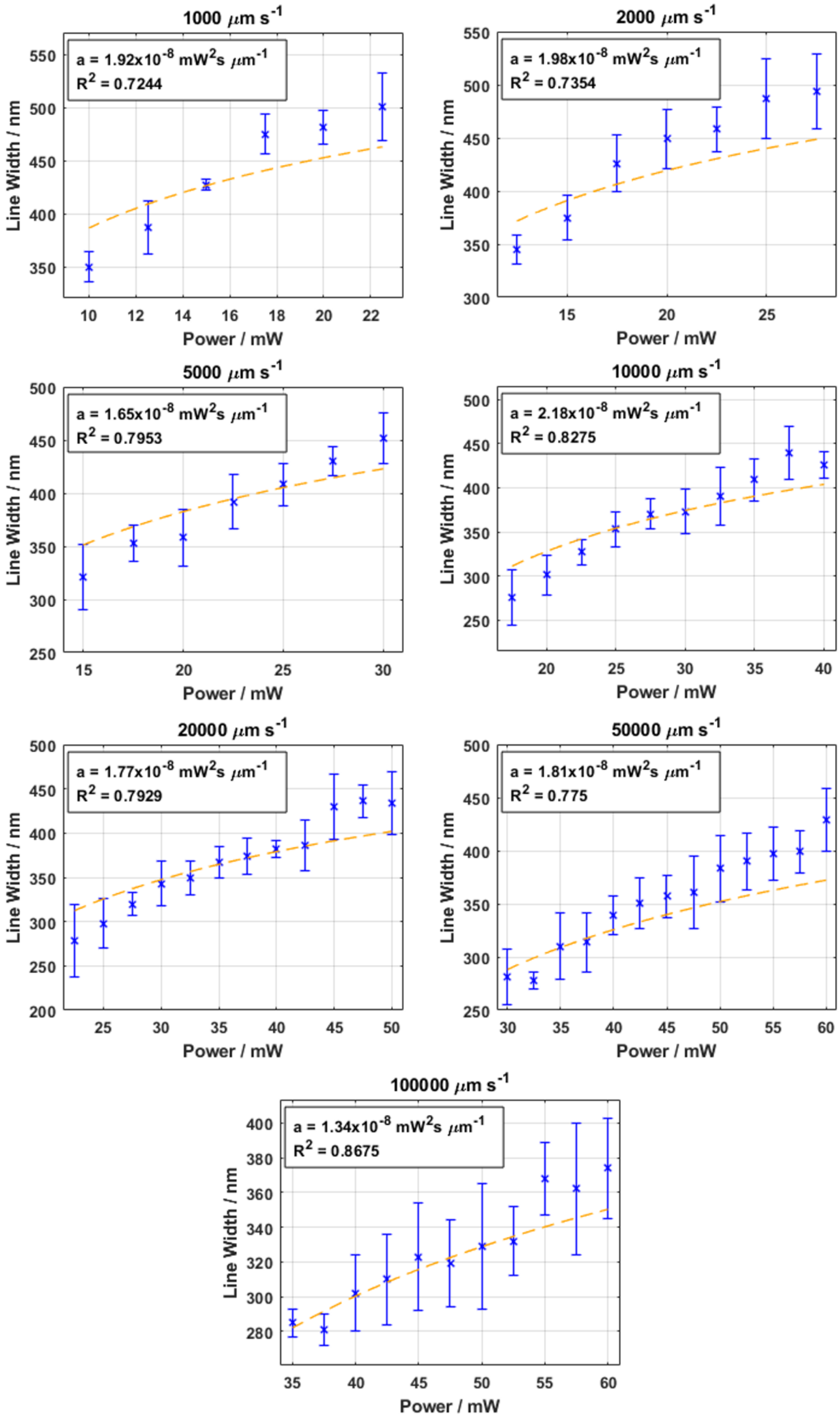

Figure 3.9: Line width against laser power with associated theoretical fit for the highest 7 scan speeds. Annotations as in figure 3.8.

To further demonstrate the inaccuracy of the theoretical fit, figure 3.10 shows the fitting parameter a and the R^2 value with respect to the log of the scan speed. The decrease in the size of the error bars for a and the increase in the R^2 value show an improved fit as the scan speed increases. The final fit coefficient data point does not have an associated error as it was defined by the bounds of the fit given by equation 3.2, additionally a cannot go below 0 for any of the scan speeds. Physically, a should have the same value for all scan speeds as it is only dependent on material parameters. Yet, while the plot shows a decrease in a towards the higher scan speeds, the large uncertainty on the first 4 data points indicates that there may be more factors to consider within the theoretical equation (equation 2.17). This will be discussed further in section 3.4.3.

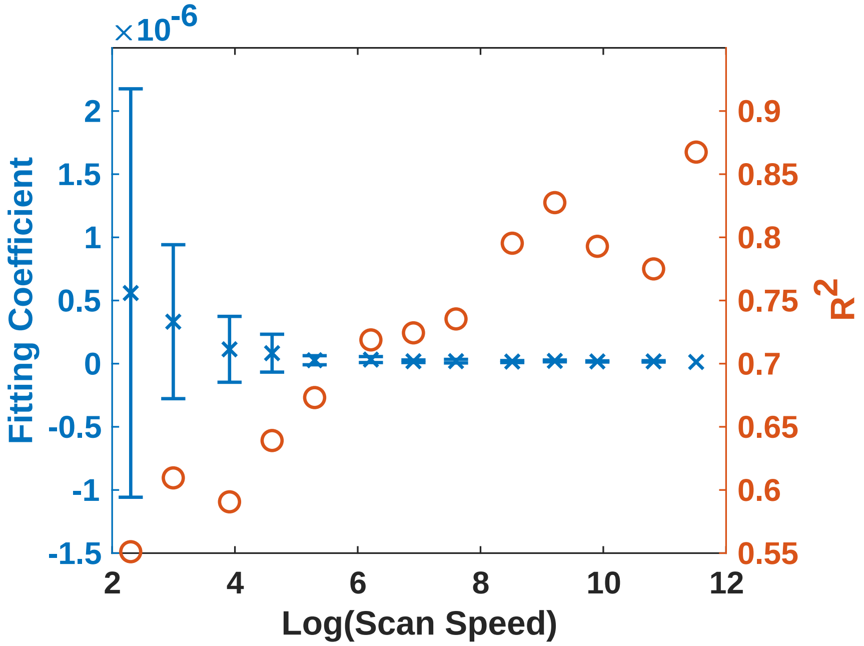

Figure 3.10: Blue (crosses): Fitting coefficient, $a = \beta / I_{th}$, against the log of the laser scan speed. The fitting parameter appears to decrease from the lowest to highest scan speed however there is a large uncertainty on the lower 4 scan speeds meaning this trend may not be accurate. Orange (circles): Coefficient of determination, R^2 against log of the scan speed. There is a clear increase in the goodness of fit for the higher scan speeds. These data indicate that the theoretical equation may not be taking into account physical phenomenon more apparent in the lower scan speed region.

Further work looked at using an optimisation algorithm to find the single best fit value across the whole data sets since a should be the same for all scan speeds. Using the *nlinfit* function in MATLAB a was found to be a = (2.0315 ± 0.3411)$\times 10^{-8}$ mW^{2}s μm^{-1}. The uncertainty associated with this value is large compared to the value itself. In addition, the value of a is still bound by the the upper limit given by equation 3.2, which across all scan speeds is bound further by the lowest a_{upper} limit, i.e a_{upper} = 1.34$\times 10^{-}8$ mW^{2}s μm^{-1} for SS = 100 000 μm s^{-1}. This upper limit is not within the uncertainty of the a result from the optimisation algorithm.

3.4 Discussion

3.4.1 Resin Dose Region

Multiple dose tests should be undertaken as on the day differences can cause a discrepancy in where the dose boundaries exist. Dust or bubbles in the resin can cause micro explosions where the dose would otherwise be acceptable, thus lowering the upper power boundary. These issues could be reduced by setting up the TPP within a clean room environment to reduce air particulates or by filtering the resin before use. Nanoscribe have recently started selling resin in syringes with the aim of reducing the number of air bubbles formed during deposition, this should also reduce or even eliminate particulates entering the resin tube as there is no top facing opening to collect dust.

The lower power boundary exists as more of a phased state between insufficient energy and a good dose. It is clear when polymerisation has not been initiated as there is no structure present at that point in the array. However, there is a point where there is a high enough dose to cause polymerisation, but the structures formed are inconsistent. The example in figure 3.2(a) shows that polymerisation has occurred, but many of the logs in the structure have fused together. One explanation for this is that the voxel height is shorter at lower doses, so the overlap, and thus the adhesion, between the layers will be reduced. This will create loose lines in the structure that are freely able to move towards each other under capillary attraction. This region has been excluded from the accepted dose region in this work, however it is clear that structures can be formed here but would rely on the specific geometry that is to be printed.

Following on from that last point, usually dose tests are performed with the structure that is planned to be printed. This is because the hatching and slicing distances (line spacing and layer offset) affect the dose in a particular region due to proximity effects [119]. A more densely packed structure will have the accepted dose region shifted towards the lower power regions, whereas the region for a highly spaced structure will be shifted towards the higher power regions. As will be shown in chapter 4, the metamaterial structure used in this work is a cylindrical fishnet structure, with varying numbers of spokes between each ring. This changes the density of the structure, as required to alter the refractive index, and so the dose region is likely to be different depending on the number of spokes in the structure. As such a new dose test was undertaken to tweak any boundaries for each spoke variation; results will be shared in chapter 4.3.3.

3.4.2 Line Width Study

The methodology used in this section was based on methods presented by Guney et al. [115] to allow for comparisons between this thesis and their work. The results in figure 3.5 can be compared to the line width vs laser power results presented in figure 3 in [115]. Both works have shown the expected trend of increasing line width with increasing laser power, and decreasing line width with increasing scan speed. Data points in both works are somewhat scattered with anomalies in the trend present for most scan speeds. The actual line width values themselves are not directly comparable due to using two different resins (IP-L verses IP-Dip), in addition to having different lab conditions and image analysis techniques; both works used ImageJ but specific filtering and measurement algorithms are not discussed in [115].

The data in figure 3.5 shows a large overlap between the first 5 scan speeds. This is likely due to line dimension saturation where the monomer and/or photo-initiator concentration drops around the volume of the focal spot where polymerisation is confined. Yet it is unlikely to be at complete saturation since the increased exposure time may lead to micro-explosions in the photoresist before this point. This is the result of rapid temperature increases due to photo-ionization in the photoresist [120].

Line width variations within a single print are usually due to inhomogeneities within the photoresist, and variations in the laser power and scan speed. The laser power is controlled by an AOM, therefore AOM voltage fluctuations will affect the power at any given point and thus alter the resulting line width. Generally, it seems that there is a larger uncertainty in the data for faster scan speeds demonstrating the trade-off between writing time and precision [115].

Other in-run variations include imperfections in the lines themselves leading to inaccuracies with the bounding box analysis. Figure 3.6 shows three types of line imperfections: overgrowth, bowing, and debris. Lines are fabricated from left to right, as such the overgrowth is likely due to extra exposure at the start of the line where the laser is not yet at speed. Bowing is likely due to a lack of initial adhesion to the substrate leading to the line shifting within the resin or development solution before settling. This lack of initial adhesion may occur due to localised height differences in the substrate. Debris encompasses various forms of dust or other particulates left over from various points in the fabrication process landing on or near the line inhibiting accurate bounding box analysis. In figure 3.6c the line width is increased due to undissolved resin in that region. While it is difficult to control for these imperfections, averaging over more lines would reduce the affect they have on the overall dataset, however this will increase the time taken to run the study.

Run-to-run variations are more important when setting the expected line dimension uncertainty. Laser power and scan speed calibration are performed automatically before each run which introduces uncertainty as the algorithm will find the substrate/resin interface at slightly different position each time. In addition, day-to-day variances in lab conditions, namely temperature and humidity, will have an effect on the resin causing variances during polymerisation. During one week of tracking these variations were measured as ± 0.2°C and ± 4.5%. While these are small differences, they do not account for the changing seasons which, in terms of temperature, were noticeable as a lab user. Further tracking of humidity and temperature over the seasons should be undertaken to see if implementing improved environment controls are required.

When setting up the SEM, finding the focus, as well as correcting beam alignment and astigmatism are user-controlled so naturally vary each time. For the example shown in figure 3.7 an additional reason for difference in line dimensions for the same array could be due to degradation of the array as the electron beam will have been focused on that spot longer than when just taking a single image. Since only a single example was investigated the 3 pixel (51 nm) difference may not be representative of the expected variation between measurements.

The pooled standard deviation results presented in table 3.2 are much smaller than the equivalent results discussed in Guney et al. [115]. Their in-run deviation for line width was found to be 42.2 nm and the run-to-run was 49.6 nm for lines printed on an identical Nanoscribe system in the resin IP-Dip. Differences are likely due to using a different system with its own environmental fluctuations, as well as likely differences in image processing techniques. The run-to-run SD determined in this thesis of 26 nm is 10% of the minimum line width, therefore an investigation into how much of an affect this has on the properties of the metamaterial should be undertaken in future work.

Finally, the study was limited to measuring line widths only as these dictate the working wavelength region of the metamaterial. However, line heights are important to understand to ensure a good overlap between layers for adhesion. Additionally, a mismatch in heights, due to altering the dose, across different regions in a GRIN metamaterial structure would need to be accounted for in the design. Therefore, ways in which to accurately measure the line height should be considered in the future. One suggestion could be to fabricate a structure with several layers and use optical profilometry to measure the overall height, as in Bunea et al. [121]. Using this, combined with the number of layers and layer offset, the height of each layer can be calculated; note however that many additional uncertainties are likely to be introduced with this method. In chapter 4 the use of silanized slides to improve adhesion of the fallen lines was investigated and the results presented.

3.4.3 Theoretical Line Width Fit

The results in figures 3.8 and 3.9 show that the theoretical line width equation (equation 2.17) overestimates the line width for lower powers and underestimates line widths for higher powers. While a single optimised fitting parameter was investigated, mathematically a is limited by the lowest value equation 3.1 can take across all scan speeds to avoid complex results.

Additionally, the large uncertainties on the results in figure 3.10 indicate that the theoretical equation may not be taking into account physical phenomenon present at the lower scan speeds. In particular, rapid temperature increases due to photo-ionization may be altering the line widths considerably in this region [120]. Indeed, across the literature where many papers present line width results in this lower scan speed range, the data deviates from the theory [90, 122–125]. Many of these papers present the data and the line of best fit, however none discuss the goodness of fit, even when the theoretical line is clearly not describing the dataset well as was found in this thesis.

Of particular note is Shukla et al. where their work focused on simultaneous polymerisation and photoreduction [124]. They present line width against laser power results for lines of both Resin (SU-8) and Resin/Metal (SU-8/Au) fabricated at a laser scan speed of 50 μm s^{-1}; figure 2 from [124]. Their measurements were taken from confocal transmission images of lines still supported by the uncured polymer. The levelling off of line width at low powers would indicate a limitation in the measurement technique since theoretically line width should keep reducing until the dose is insufficient for polymerisation. Nonetheless, after excluding these data points, the theoretical equation fits their polymer-only data with the same trend as found in this thesis; overestimating at the lower powers and underestimating at the higher powers. In the absence of error bars, it is unclear to what degree the theoretical equation fits their data, however from visual inspection it looks to be a better fit compared to the equivalent in this work for SS = 50 μm s^{-1} shown in figure 3.8; likely explained by the difference in resin.

For the Polymer/Gold results in [124] the same pattern is less apparent. While the data point for 50 mW is below the fit line, the next three data points seem to follow the reverse trend whereby the theory is underestimating at the lower power region and overestimating at the higher power. With only four data points and no uncertainties it is difficult to form conclusions of fit to such a complicated function. However, since both polymerisation and photoreduction occurs, it is unlikely to follow the same pattern as the polymerisation-only process due to the additional physical mechanisms in play. This will require further investigation if simultaneous photopolymerisation and photoreduction is used to reduce the minimum line width in future work related to this thesis [94].

Liu et al. present line width against stage speed (equivalent to scan speed where the stage is moved relative to the laser focal spot instead) results in figure 4 in [125]. Speeds were between 5 μm s^{-1} to 40 μm s^{-1} and once again their experimental data deviates widely from the theoretical line in this range. In particular, their 10 mW power fit produces an asymptote towards zero between two data points which is not addressed in the paper. Liu et al. [125] present a single fitting parameter $C'_{th} = I'_{th}/\beta\tau\nu$ (parameters are the same as in equation 2.17) with a value of C'_{th} = (5.74 ± 0.86)$\times10^{-5}$ mW^{2}s μm^{-5}. It is not stated how this value was obtained, although it is assumed to be the average the individual fits. Much like in this work, it is likely that using a single fitting parameter across each data set caused the $\ln$ term to go negative and thus produced a complex result invalidating the line width prediction.

One way to by-pass the derivation of a full physics model of line dimensions is to develop an empirical model. Guney et al. [115] report on a semi-empirical analytic model through simulations of the focal spot and fitting on their experimental line width and height data. Their simulation was used to generate an initial line dimension where the polymerisation reaction begins, which increases until the final dimension is reached at the end of the polymerisation reaction. They then use a mixture of general form equations with power and scan speed dependence, and physical relationships (such as the radical chain polymerisation rate) to generate general equations with model coefficients obtained by fitting their line width and line height for the Nanoscribe resin IP-Dip. The model was able to estimate line dimensions to within one standard deviation of the average value in 86% of cases over a wide range of dose combinations. Future work should look at finding equivalent equations for IP-L, this has not been undertaken in this work as there appear to be some minor steps missing from the methodology in [115] which will require further investigation.

3.5 Summary

- The dose region producing “good” (i.e well polymerised, stable) structures for IP-L has been found across a wide range of scan speeds and laser powers.

- A catalogue of achievable line widths was created where the maximum line width was found to be 561 nm ± 21 nm for a dose combination of SS = 10 μm s^{-1} & LP = 12.5 mW and the minimum was 273 nm ± 32 nm for SS = 50 μm s^{-1} & LP = 5 mW.
- The run-to-run standard deviation of the line width results was found to be 26 nm. However, tests will need to be undertaken to assess the affect these variations would have on the properties of the metamaterial.
- The line width against laser power data for each scan speed was fit to the theoretical equation. The fitting parameter representing the ratio of the material coefficient and threshold intensity was found for each of the different scan speeds. The theoretical equation does not fit the data well and other methods of line width prediction should be investigated in future work.
- These results show the ability to manipulate the line dimensions using the printing parameters which is the suggested method for altering the metamaterial unit cells within the lens. However, line height should be investigated again in the future in order to fabricate a lens with a consistent height between each refractive index region.

Overall, this chapter has achieved its aim of creating a catalogue of achievable line widths for different fabrication doses. These values were used in the analytical calculations in chapter 5. Altering the line width changes the filling fraction of the structure which will contribute towards changing the refractive index of the metamaterial. The next chapter presents work assessing the current capabilities of the commercial TPP system with respect to fidelity to the design, structural stability, and creating feature size gradients.

Chapter 4

TPP Fabrication Capabilities

4.1 Introduction to TPP Fabrication Capabilities

The aim of this chapter was to assess the capabilities and viability of TPP for fabricating gradient metamaterial structures. As discussed in chapter 2, there are several issues and considerations when fabricating using TPP. Here, initial work towards controlling shrinkage, increasing substrate adhesion, and printing larger areas are considered. Following on from this, an investigation is undertaken into how to implement feature size gradients across a structure. By altering the feature sizes, the properties of the metamaterial can be tuned to a particular value at arbitrary points in the structure. This would allow for a single structural print file to be used and only the laser power and scan speed would need updating to create new gradients, rather than creating a whole new file each time, thus streamlining the design and fabrication process. To investigate this, gradient woodpile structures were fabricated where the laser parameters were changed both between different scan lines and along a single scan line. Finally, using the knowledge gained from practical use of the system, a metamaterial geometry is suggested for the GRIN lens.

4.2 TPP Exploration Methodology

4.2.1 Fabrication Considerations

Section 2.3.2 discussed TPP limitations that are of particular importance to consider when fabricating metamaterials. In particular, shrinkage and structural deformation will alter the geometry of the metamaterial and thus have an affect on its resulting properties. Additional considerations include limits on the size of the metamaterial that can be fabricated; important if you want a large area lens. This section presents the methodologies used to investigate shrinkage and large area fabrication based on a practical understanding of the process.

Controlling Shrinkage and Improving Adhesion

Two methods of controlling shrinkage are implemented and compared: creating a frame around the main structure, and using silanized glass substrates. With the frame implementation, the idea is to contain any shrinkage to the outer edges of the frame and to provide a support to the structure of interest. To minimise extra fabrication time, rather than a solid frame, a fishnet structure is fabricated at SS = 10 000 μm s^{-1} and LP = 25 mW with 0.5 μm spacing between each line. A fishnet structure is demonstrated in figure 2.9 and is so called due to its resemblance to fishnets used in the fishing industry.

Two .gwl files were made, one with a square cut out in the central region and one with a circle cut out, this is where the main structure will be fabricated. The structures have been programmed in such a way that the size of the central region can be changed with a single parameter, making it adaptable to many different structure sizes. Woodpile structures are also fabricated at SS = 10 000 μm s^{-1} and LP = 25 mW with and without the frames in order to compare the results. For each layer, the frame area is printed first for the main structure layer to be embedded into.

The second method is to use silanized glass slides in order to increase the adhesion to the substrate as this will affect the structural stability. As such, the use of silanized slides was compared to slides prepared as outlined in chapter 3. Silanization functionalises the surface of the glass to promote better adhesion to the substrate while printing [126]. Slides were prepared on behalf of the author using the following silanization process:

1. Treat slide with oxygen plasma for 10 minutes
2. Soak in a solution of 8 mL 3-(Trimethoxysilyl)propyl methacrylate and 400 mL dry Toluene at 50°C for 2 hours
3. Wash twice in Acetone
4. Dry under vacuum at 35°C.

Forming a solid structural foundation should have a positive affect on the structure as further layers are polymerised. The same woodpile structures both with and without frames are printed as a point of comparison. Additionally, the ascending scan array test pattern from chapter 3 was printed to see if the improved adhesion will allow the measurement of line heights.

Large Area Fabrication

When using the 63X objective on the Nanoscribe, as described in section 3.2.1, fabrication is limited to a circular region with diameter d = 200 μm. Creating structures larger than this requires splitting the structure and moving the stage to fabricate each area in succession; this is known as stitching. When importing a CAD model, the splitting is guided through DeScribe, where settings such as block size, wall angle, and stitching overlap are chosen. However, since the metamaterial is not a solid block of material but will be made from multiple individual scan lines which are generated from programming rather than created from CAD, it is up to the user to define such settings within the code to ensure the lines in each area overlap. Initial work looking at the accuracy of stitching single lines together has been undertaken here. Four woodpile structures were fabricated next to each other in succession to create a larger structure. Woodpiles were also made where each layer was written in one go with the aim of increasing adhesion between each segment.

4.2.2 Geometry Alteration by Process Variation

Initial geometry alteration work focused on the woodpile structure, which consist of layers of logs offset by 90° each layer with a $\frac{1}{2}$ pitch horizontal offset every 2 layers, as illustrated in figure 4.1. Firstly, four types of woodpiles are fabricated at SS = 10 000 μm s^{-1} and the power is different for each log in the structure. Each woodpile is as follows: (1) power increasing from 15 mW to 35 mW and decreasing back to 15 mW in steps of 1 mW for both x and y oriented layers, (2) the same power profile as (1) but only for x oriented lines, y oriented lines are fabricated at 25 mW, (3) power increasing from 15 mW to 35 mW in steps of 0.5 mW for each log in both the x and y oriented layers, and (4) the same power profile as (3) but only for the x oriented layer, y oriented lines are fabricated at 25 mW.

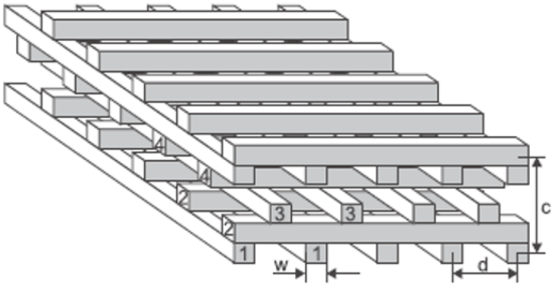

Figure 4.1: A schematic of the common woodpile structure which consists of layers of logs in alternating orientations. Every two layers, there is a $\frac{1}{2}$ pitch offset in the layers. Where the pitch is defined here as d and is the spacing between the logs. A unit cell consists of 4 layers as labelled on the diagram with c being the unit cell height. Additionally, w is the width of each logs which in this work corresponds to the line width.

Next, changing the power along a single scan line is investigated and can be achieved by two methods. The first is using an inbuilt Nanoscribe function by defining a 4th column in the coordinate value array which sets the power at the line's starting and finishing coordinate. For example,

$$\begin{array}{cccc} 0 & 0 & 0 & 30 \\ 10 & 0 & 0 & 50 \end{array}$$

creates a 10 μm line along the x-direction where the power increases linearly from 30$\%$ at the starting coordinate (x=y=z=0), to 50$\%$ by the time it reaches the end coordinate (x=10, y=z=0). The second method is to manually change the power by dividing the line into sections and defining the power for each section using the $LaserPower$ function. This second route enables a user defined power profile for the laser. Both single layers of lines and woodpile structures are fabricated using both methods. The 4th column linear power change is from 20 mW to 35 mW along each line in the structure, and the user defined line-segmentation method uses a hyperbolic secant power profile with a 35 mW maximum power at the centre, decreasing to 20 mW at the edges.

4.2.3 Metamaterial Geometry

While TPP can theoretically be used to fabricate arbitrary 3D structures, design considerations must be met in order to create a structurally sound and repeatable geometry. A metamaterial geometry was designed based on the outcomes of the work in this chapter. A circular structure was designed with the aim of reducing the stresses built up during fabrication to combat shrinkage without the need for a frame.

Each layer of the structure consists of an array of concentric rings with a number of spokes between each ring as illustrated in figure 4.2. It could be likened to a cylindrical fishnet and will be referred to as such in this work. Similar structures have been reported

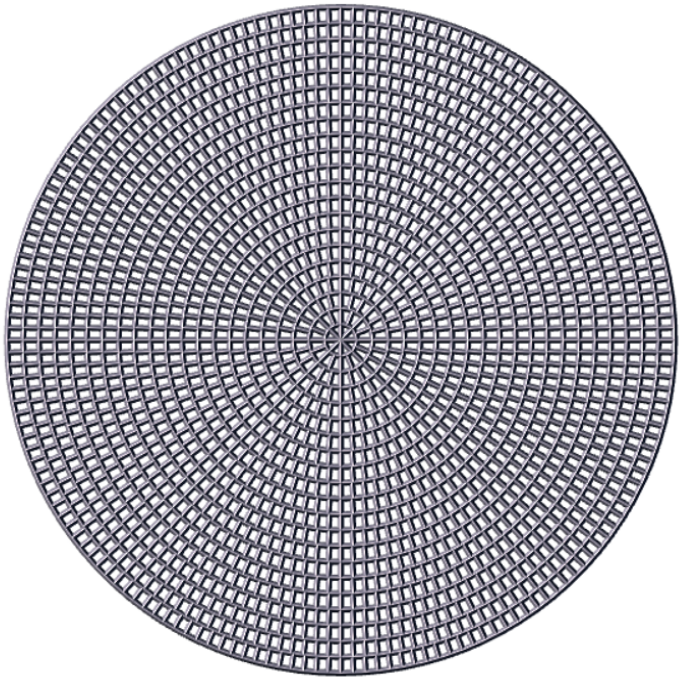

Figure 4.2: A rendering of the cylindrical fishnet structure.

for metamaterials working in the microwave regime [127–129]. More importantly, the cylindrical structure will serve as a point of comparison to traditional rod GRIN lenses with regards to its focal length, which will be explored in chapter 6.

The cylindrical fishnet structure provides multiple ways to alter the geometry across the device including; changing the line width of the rings/spokes by altering the laser dose, changing the number of spokes within a particular region, and changing the length of the spokes (corresponding to the gap between each ring). To assess the suitability of the structure for fabrication using TPP, a non-graded cylindrical fishnet structure is fabricated. Next, demonstrations of the different unit cells are made by changing the spoke length, or by changing the laser power, for different densities of spokes. Then, a new dose test was performed to confirm or update the dose region found in chapter 3. Finally, a single layer concentric ring pattern with a 422 μm diameter was fabricated as a first attempt at stitching this structure to create larger areas.

4.3 Results

4.3.1 TPP Fabrication Investigation

Improving Structural Stability

Figure 4.3 is an SEM image of 10 woodpile structures. The top row shows woodpiles with a frame with increasing length from left to right, and the bottom shows woodpiles without a frame for the corresponding woodpile lengths. The slight charging (bright regions) around the outer edge of all of the structures provides an indication of the degree of shrinkage in the structure. This appears to be confined to the outer edges of the structure as expected. However, there is an apparent bulging around the inner edges of the frames which increases with increasing frame/woodpile length.

Figure 4.4 shows the same woodpile test structure printed on a silanized glass slide. Once again the brighter edges are an indication of the deformity around the outer edges. For the silanized slides, there is no bulging on the inner edges of the frame as with the glass slides. This indicates that the combination of silanized slides and the implementa-

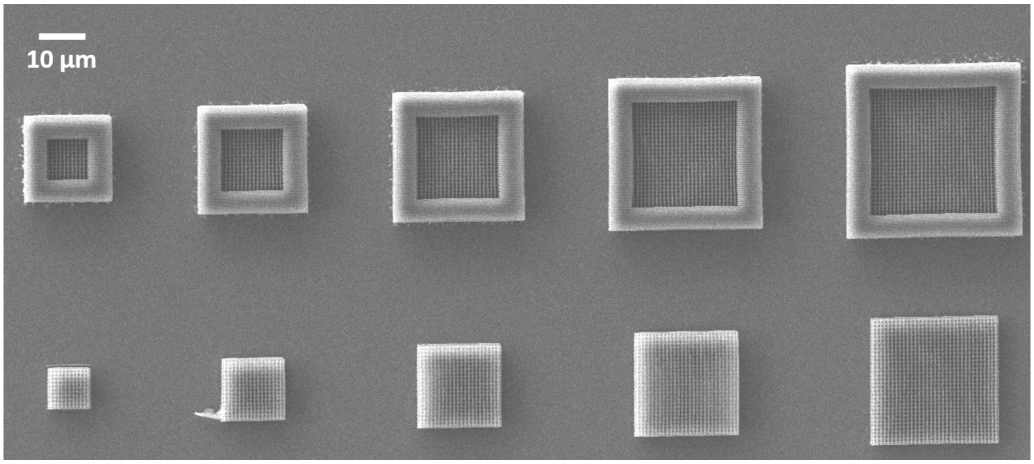

Figure 4.3: SEM image of woodpile arrays of increasing side length (10 μm to 30 μm in steps of 5 μm) printed onto a glass coverslip where the top row has a 5 μm boarder implemented.

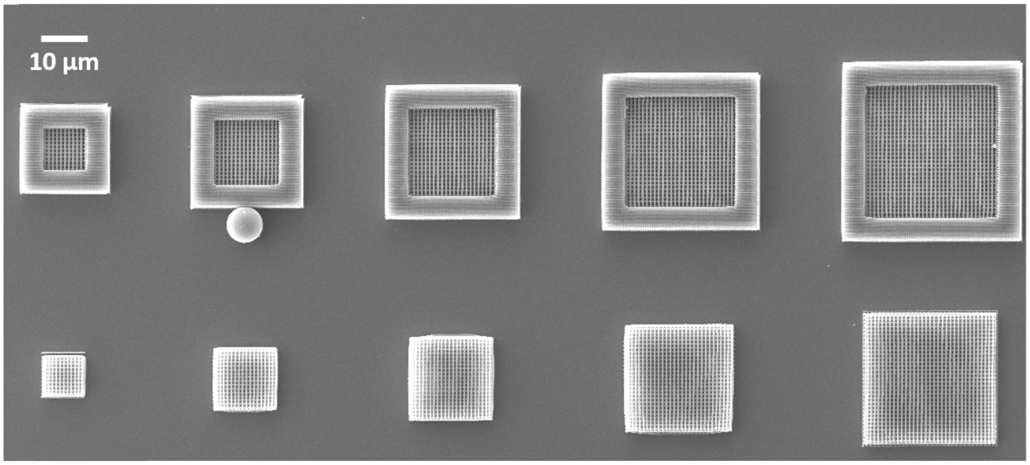

Figure 4.4: SEM image of woodpile arrays of increasing side length (10 μm to 30 μm in steps of 5 μm) printed onto a silanized glass coverslip where the top row has a 5 μm boarder implemented.

tion of frames would improve structural fidelity of the resulting prints.

The average percentage decrease in woodpile side length compared to the designed side length was found from figures 4.3 and 4.4. A line ruler in ImageJ was used to measure the size lengths manually. Table 4.1 shows the results of the overall percentage decrease in side length across woopiles of all side lengths, as well as the average percentage decrease in the x- and y-dimensions separately. Overall the shrinkage is less for the silanized substrate compared to the untreated glass substrate with a maximum difference of 3.8

Table 4.1: A table showing the average percentage decrease in structure size from the designed woodpile size length to the fabricated structures for the two substrate preparation techniques, for woodpiles with and without frames.

		Shrinkage (%)		
Sample Type		**Overall**	**x-direction**	**y-direction**
Glass	Frame	12.7 ± 1.6	12.1 ± 1.9	13.2 ± 1.0
	No Frame	11.6 ± 1.2	11.1 ± 1.3	12.1 ± 0.9
Silanized	Frame	9.3 ± 1.0	9.2 ± 1.1	9.4 ± 1.1
	No Frame	8.9 ± 1.7	8.5 ±2.0	9.4 ± 1.7

percentage points between framed woodpiles measured in the y-direction.

Figure 4.5 shows the outcome of using silanized slides for two arrays of the ascending scan pattern. In the first, the lines clearly fall and adhere “in place”, but the majority of the arrays were as in the second image (figure 4.5b) where, whilst the lines had adhered better than for the non-treated substrates, they were still bunched up and scattered.

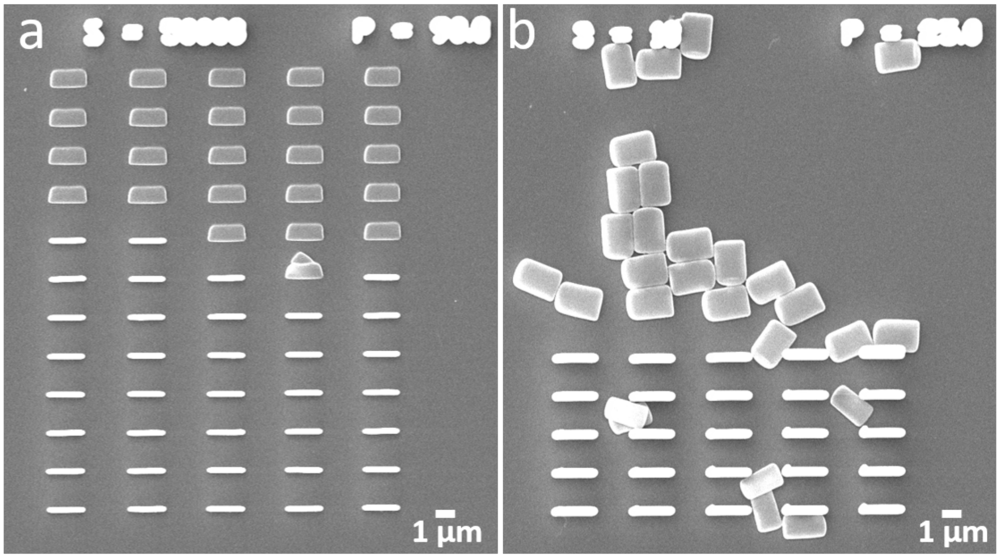

Figure 4.5: SEM image of ascending scan arrays printed on a silanized substrate for (a) SS = 50000 μm s^{-1} and LP = 45 mW showing good adhesion of fallen lines, and (b) SS = 10 μm s^{-1} and LP = 12.5 mW showing scattered but well adhered lines.

Stitching

Figure 4.6 shows two woodpile structures, (a) where each block is fabricated at once before moving to the next block, and (b) where each area in a layer is fabricated before moving to the next layer. The lack of bonding between each block is evident in figure 4.6a and further reiterated in figure 4.6c which shows a magnified image of the central region of the woodpile. The second woodpile in figure 4.6b, and the magnification in figure 4.6c, shows improved homogeneity with seams that are much less visible.

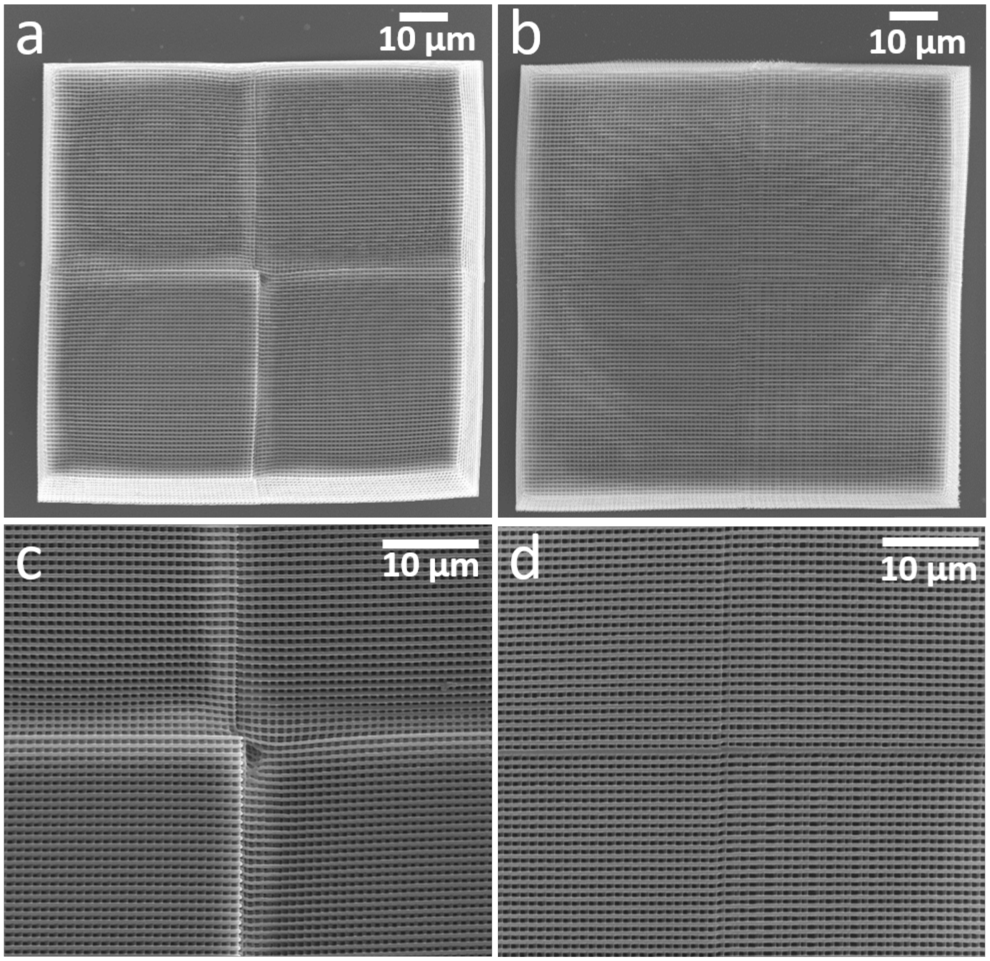

Figure 4.6: SEM images of (a) individual blocks of woodpiles fabricated subsequently, (b) a stitched woodpile where a layer was stitched together in one go, (c) magnified central region for the woodpile in (a), and (d) magnified central region for the woodpile in (b).

4.3.2 Geometry Alteration by Process Variation

Figure 4.7 shows layers of x-oriented lines with the two power profiles described in section 4.2.2. Figure 4.8 shows optical images of woodpiles where either x- or both x- and y-oriented layers are fabricated with these power profiles.

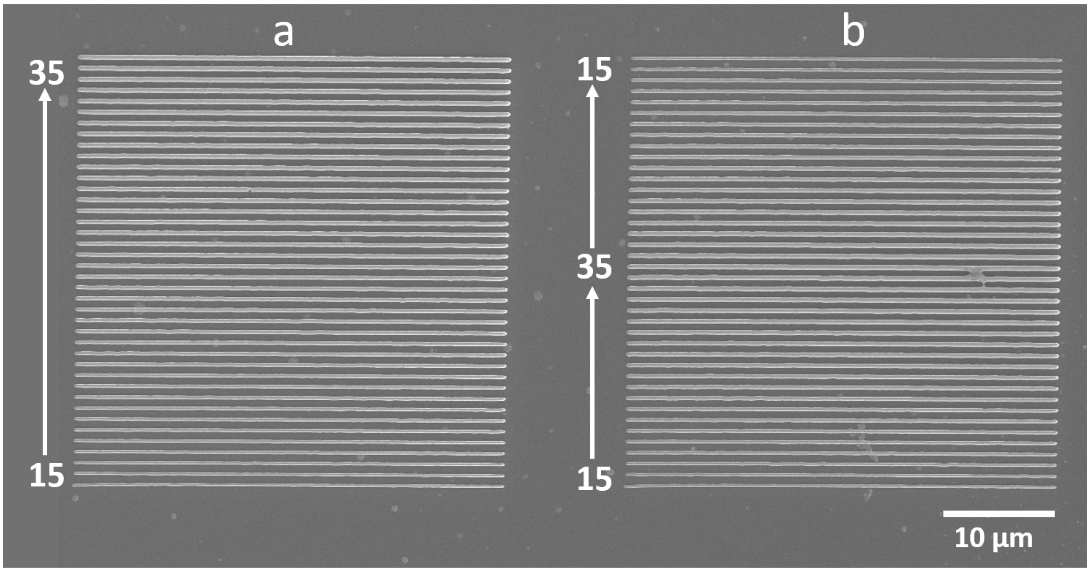

Figure 4.7: SEM images of x-oriented layers for the two power profiles with (a) LP increasing from 15 mW to 35 mW in 0.5 mW increments and (b) LP increasing from 15 mW to 35 mW back to 15 mW in 1 mW increments. Lines are fabricated at SS = 10 000 μm s^{-1}.

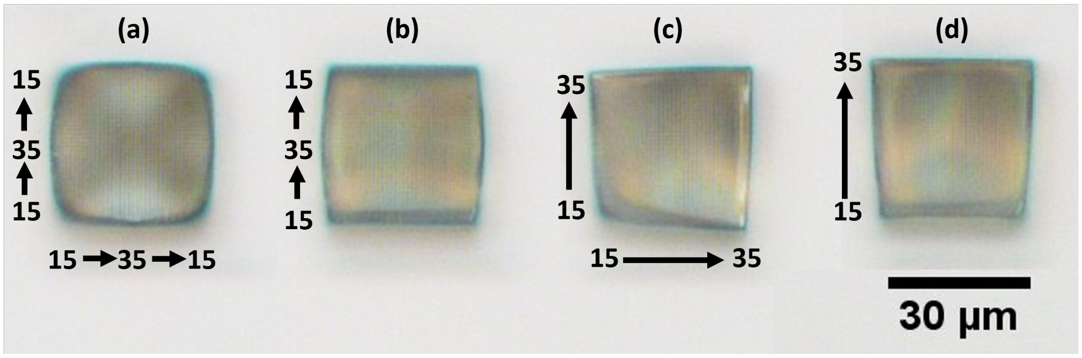

Figure 4.8: Woodpiles printed at SS = 10 000 μm s^{-1} where each line is written at a different LP. The black annotations show the linear power profile for each layer. For (b) and (d) only the x-oriented lines have a power change, y-oriented lines are fabricated at 25 mW.

Figure 4.9 shows the implementation of changing power along a single scan line. In figure 4.9a the line widths are changed using the 4th column method as discussed in section 4.2.2. Lines increase in width from left to right corresponding to lower to higher power. The resulting samples that was produced using a hyperbolic secant power profile is shown in figure 4.9b where the line width increases towards the centre and decreases again. There is a 0.1 μm overlap between the segments to create a more continuous line compared without the overlap as shown in figure 4.10.

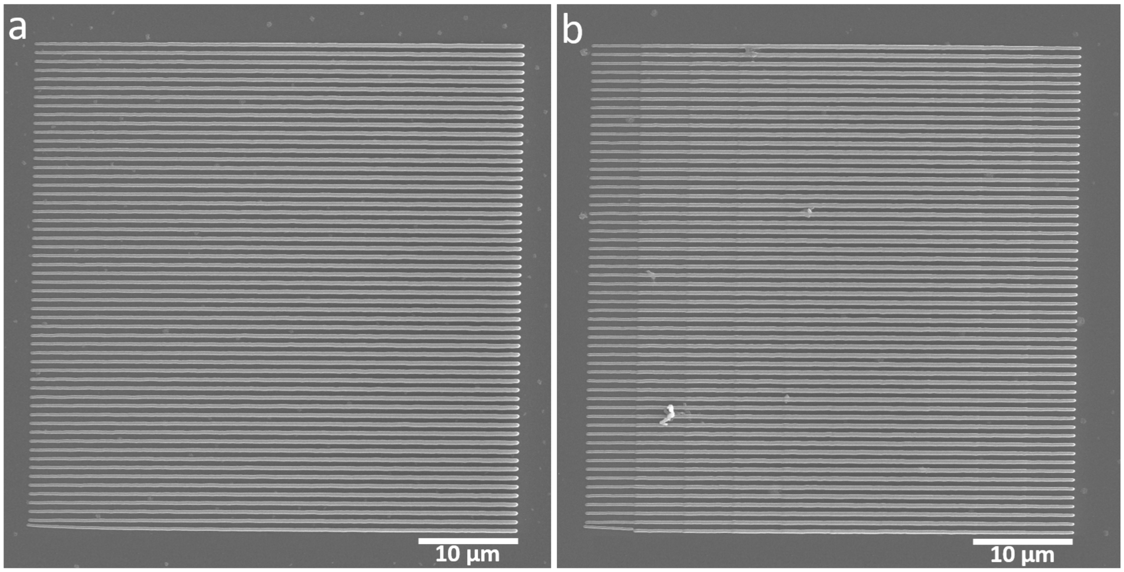

Figure 4.9: SEM images of gradient power lines fabricated at a scan speed of 10 000 μm s^{-1}. In (a) LP along the line increases from 20 mW to 35 mW using the in-build function. (b) LP is user defined hyperbolic secant profile with a minimum power of 20 mW rising to 35 mW and lowering back to 20 mW.

Full woodpile structures are fabricated out of the layer types shown above (linearly increasing power and the hyperbolic secant power profile) and the resulting samples are shown in figure 4.11. Figure 4.11a shows a brighter patch in the lower left corner corresponding to the section with the smallest line widths. Finally figure 4.11b shows a dark circular patch in the central region of the woodpile where the lines are at their widest.

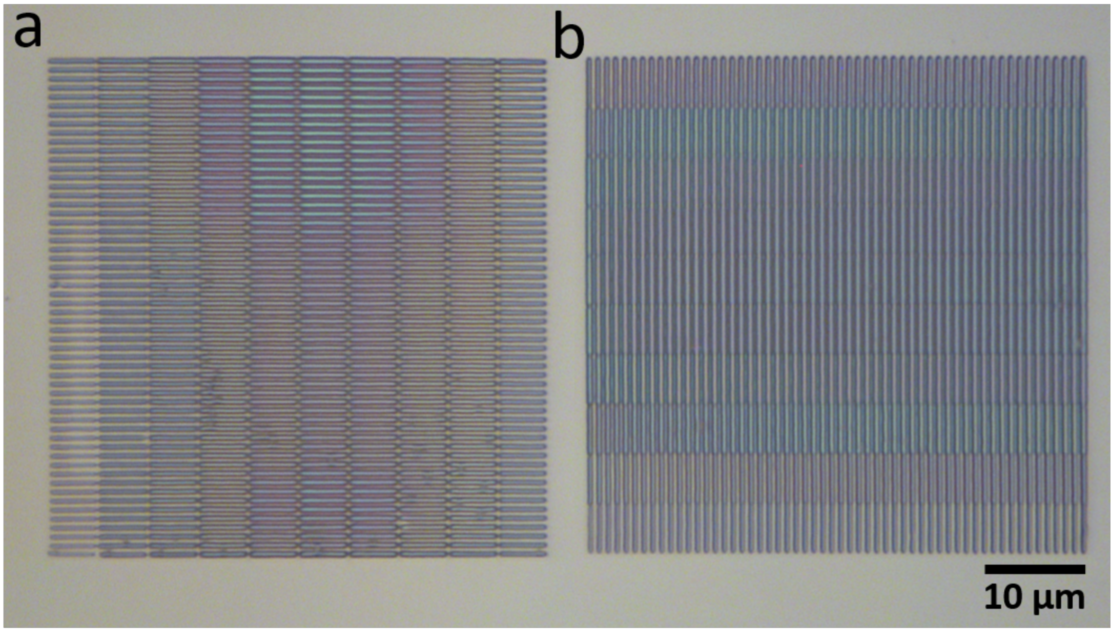

Figure 4.10: Optical images of user defined hyperbolic secant power profile for (a) x- and (b) y-oriented lines with no segment overlap.

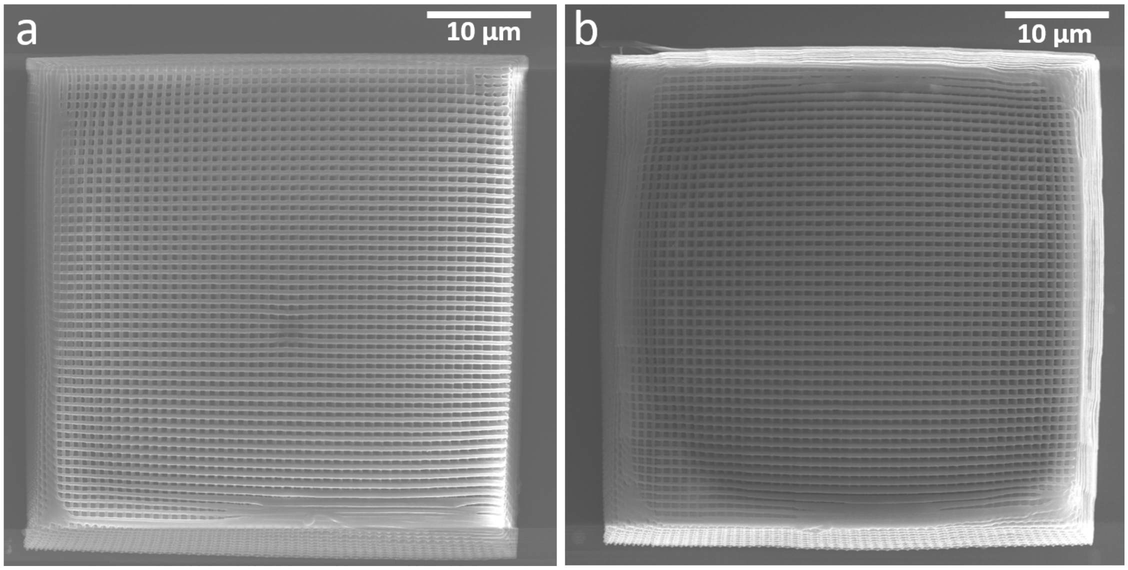

Figure 4.11: SEM images of woodpiles fabricated at a scan speed of 10 000 μm s^{-1} with different power profiles along them. In (a) LP along the line increases from 20 mW to 35 mW using the inbuilt function. (b) LP is user defined hyperbolic secant profile with a minimum power of 20 mW rising to 35 mW and lowering back to 20 mW.

4.3.3 Cylindrical Fishnet Metamaterial

Non-graded Cylindrical Fishnet

Figure 4.12 shows the first attempt at fabricating a 200 μm diameter 5-layer cylindrical fishnet structure printed at SS = 10 000 μm s^{-1} and LP = 25 mW. The structure is generally repeatable, however some prints suffered from separation between the rings. Figure 4.13 demonstrates this for both an unframed and a framed structure printed with the same parameters. Figure 4.13c is a magnified image of the outlined region in figure 4.13b, which shows misalignment of the spokes and rings in the region.

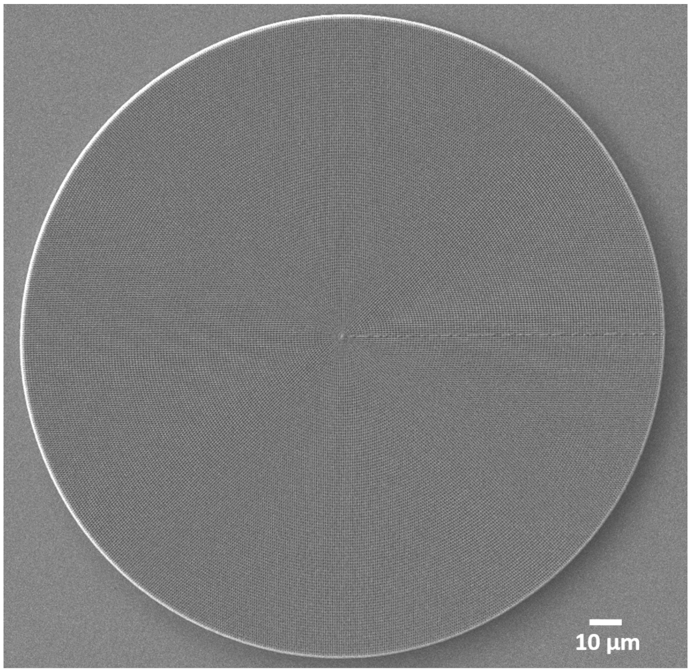

Figure 4.12: SEM image of a non-graded 5-layer cylindrical fishnet structure with diameter d = 200 μm, 1 μm spoke length, 8 starting spokes, with 0.7 μm layer spacing.

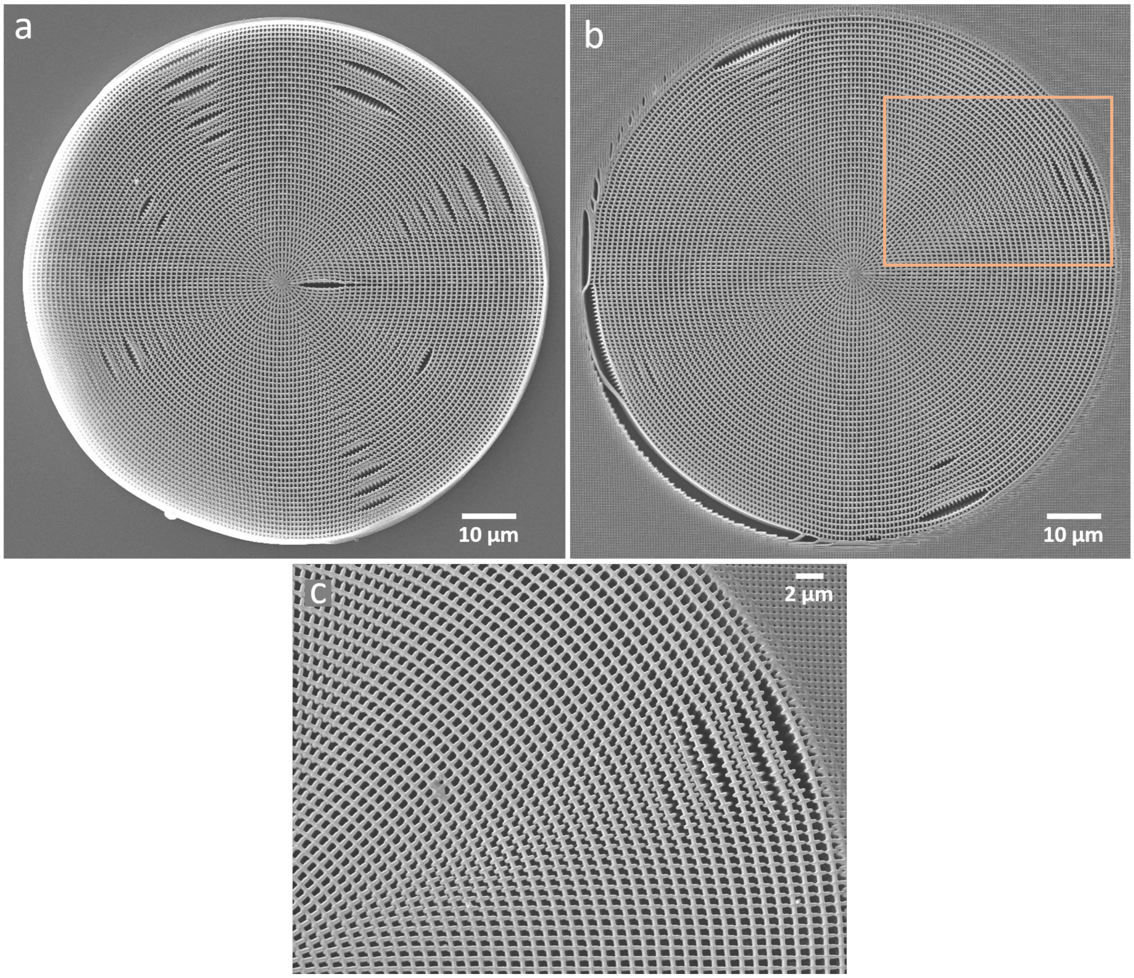

Figure 4.13: Cylindrical fishnet structures with diameter d = 200 μm, 1 μm spoke length, 8 starting spokes, and 5 layers with 0.7 μm layer spacing. (a) Without a frame, and (b) with a frame. Separation between the rings is present on both structures. (c) shows a magnified image of the outlined region in (b).

Cylindrical Fishnet Unit Cells

Figure 4.14 shows the unit cell variation achievable by changing the spoke length and the number of starting spokes. Similarly, figure 4.15 shows the geometry variation caused by changing the number of spokes as well as the laser power. This figure shows the need for the updated dose test as discussed in chapter 3 as the final 4 unit cells on the top row show micro-explosions caused by overexposure. In both figures, the unit cells consist of 6 layers with 0.7 μm layer spacing and are fabricated at SS = 10 000 μm s^{-1}.

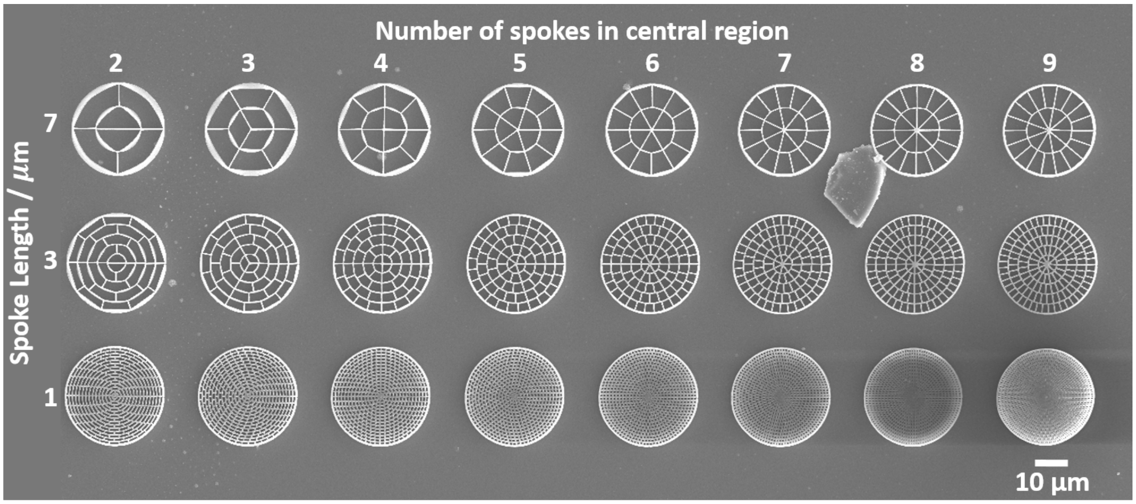

Figure 4.14: Cylindrical fishnet unit cells fabricated at SS = 10 000 μm s^{-1} and LP = 25 mW. Each column corresponds to the number of spokes in the central region, and each row is the length of the spokes, corresponding to the gap between the rings.

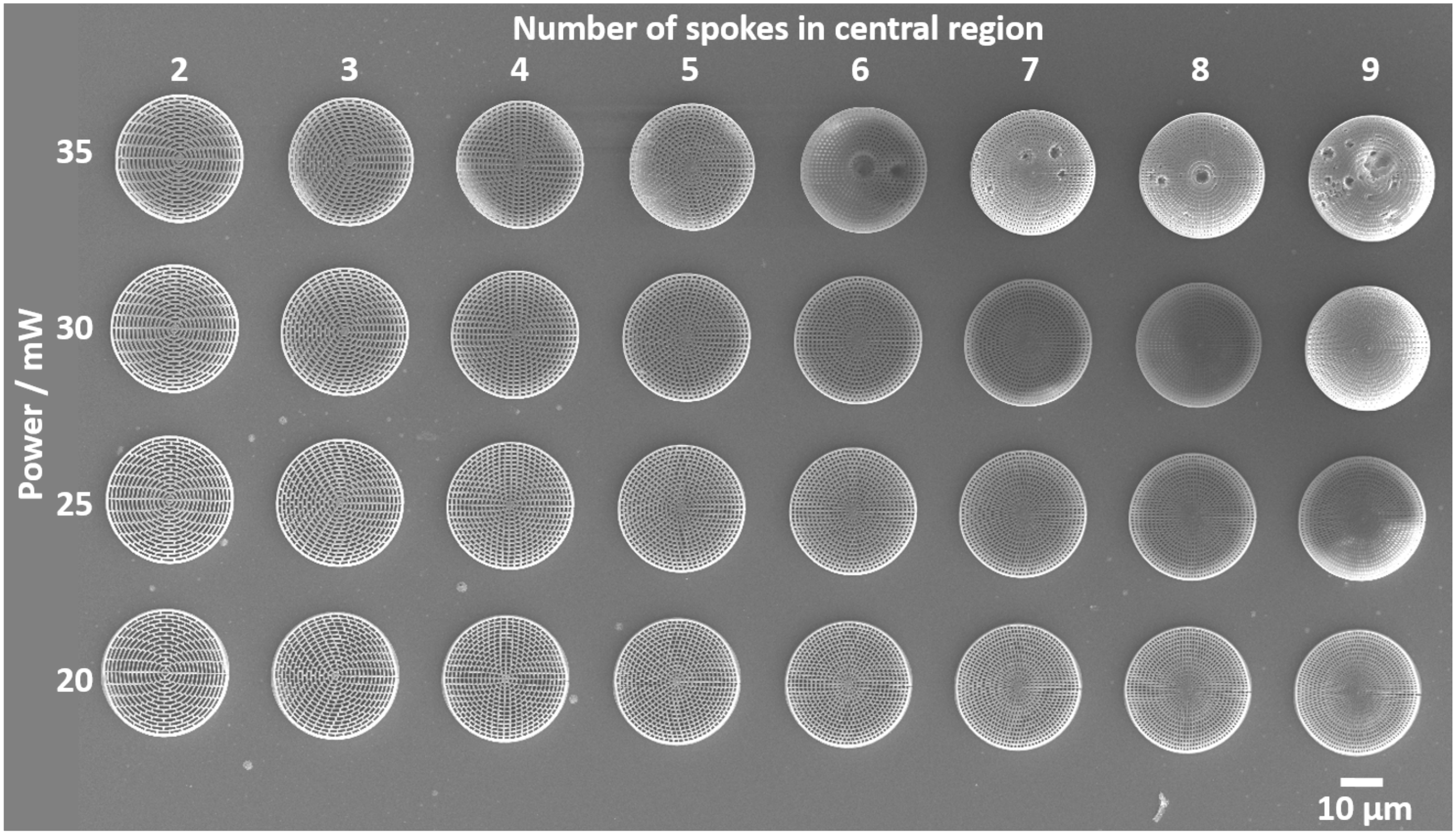

Figure 4.15: Cylindrical fishnet unit cells fabricated at SS = 10 000 μm s^{-1} with a 1 μm spoke length. Each column corresponds to the number of spokes in the central region, and each row is the laser power the structure was fabricated at.

Updated Dose Test

A new dose test was undertaken for the cylindrical fishnet structure of different spoke densities for all dose combinations outlined in chapter 3. After examining the structures, it was found that for the most part, the dose regions from chapter 3 were the same for the new structure. However, 17 combinations of scan speed, laser power and number of starting spokes were found to no longer produce good structures. Table 4.2 shows these combinations where the dose produced either underexposed (U) or overexposed (O) for that particular number of spokes. These combinations were removed from the analytical refractive index calculations in chapter 5.

Table 4.2: Table showing which scan speed, laser power, and number of spokes combination produced either underexposed (U) or overexposed (O) cylindrical fishnet structures.

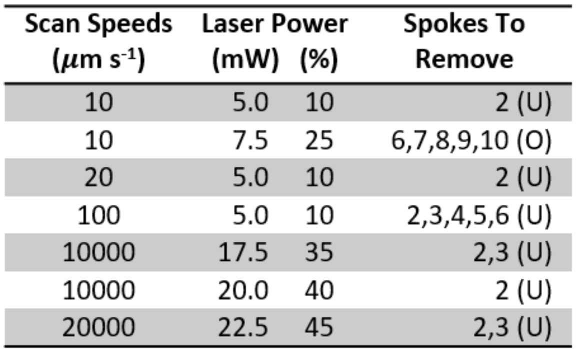

Scan Speeds (μm s^{-1})	Laser Power (mW)	(%)	Spokes To Remove
10	5.0	10	2 (U)
10	7.5	25	6,7,8,9,10 (O)
20	5.0	10	2 (U)
100	5.0	10	2,3,4,5,6 (U)
10000	17.5	35	2,3 (U)
10000	20.0	40	2 (U)
20000	22.5	45	2,3 (U)

Stitched Cylindrical Fishnet

Figure 4.16 shows an initial attempt at stitching a single layer concentric ring pattern with a 422 μm diameter. Each area is clearly visible and figure 4.16b shows the extent of the gaps between each segment for the lower right quadrant.

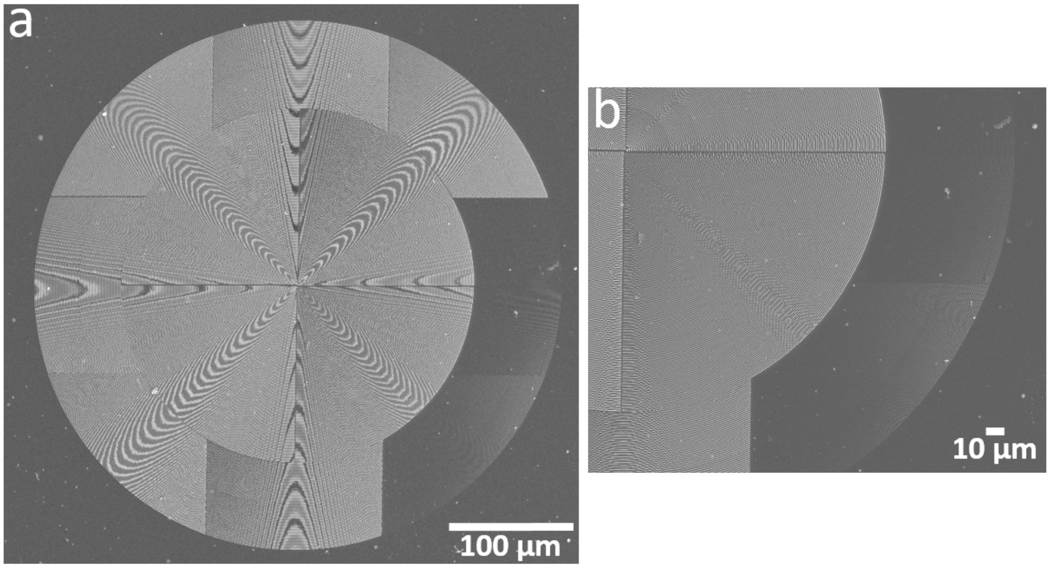

Figure 4.16: A single layer of a 422 μm diameter stitched concentric ring pattern, fabricated at SS = 10000 μm s^{-1} and LP = 25 mW. (a) Shows the full structure, and (b) is a magnification of the lower right quadrant.

4.4 Discussion

4.4.1 Fabrication Discussion

Shrinkage and Adhesion

The shrinkage results presented in table 4.1 show the difference in shrinkage between woodpiles with and without supporting frames printed on non-treated and treated glass substrates. The results show that the shrinkage is less for the silanized substrate compared to the untreated glass substrate with a maximum difference of 3.8 percentage points between framed woodpiles in the y-dimension. Additionally, there appears to be a difference in shrinkage between the x- and y-dimensions by as much as 1 percentage point, though the results are generally within 1 standard deviation of each other. The smallest difference between the two dimensions was for framed woodpiles on the silanized substrate with a 0.2 percentage point difference.

The shrinkage results show that the non-framed woodpiles appear to have less shrinkage for both samples compared to the framed woodpiles. The difference between framed and non-framed woodpiles is smaller for structures on the silanized substrate, since the silanized substrate appears to have addressed the bulging present in the inner edge of the framed structures on the non-treated substrate. While the numerical results make it appear that the frames have not helped to reduce shrinkage, the measurements taken did not account for the overlap between the woodpile and the frame. The outer edge of the woodpile is encompassed by the inner edge of the frame so that when measuring the side lengths there is a line width amount of discrepancy at each end. Looking at figures 4.3 & 4.4 there is clearly much less deformation in the woodpile structure itself with individual logs appearing evenly spaced throughout compared to the non-framed woodpiles where the outer edges have deformed due to shrinkage.

Overall these results show that frames are a viable strategy for reducing the shrinkage during development as shrinkage is contained to the outer edge of the frames rather than affecting the structure of interest. However, using a frame will increase both the fabrication time and the size of the structure. The impact on fabrication time can be reduced by printing the frame at higher scan speed than used here. Although, to keep frame stability the rod spacing will need be reduced to account for the smaller line dimensions. This means more lines would need to be fabricated to cover the same area potentially negating the faster speed.

The figures also suggest there is room to reduce the size of the frame while still containing the shrinkage which will reduce surplus fabrication time. A future investigation would be to look at the minimum frame needed to control shrinkage for different sized structures. The figures here show that the 5 μm extra border was suitable for the four woodpile sizes tested, however larger structures may need more support.

Issues may arise from frames implemented around stitched structures as it is likely misalignment at the joints will reduce the stability the frames afford. Changing from a fishnet-type structure to a solid block would reduce any alignment issues, once again with the trade off of additional fabrication time.

The use of silanized slides allowed for a more stable structure foundation and produced frames without the bulging of the inner edge. Since the woodpiles without the frames on the silanized substrate still showed signs of shrinkage, combining the two methods (frames and silanized slides) would be a simple way to reduce shrinkage for woodpile structures, with the trade off of increased slide preparation time.

As previously discussed in chapter 2, other ways to control shrinkage include precompensation for a known shrinkage rate within the design [98], by using resins with a higher molecular weight [100], or by carefully controlling the development process [102]. A potential avenue of investigation is to UV cure the structure while in the isopropanol bath to increase the tensile strength of the structure to reduce shrinkage. Oakdale et al. UV cured their structures with UV-A 365 nm light for 10 minutes while in a bath of isopropanol and 0.5 wt% Irgacure 651 and found dramatically improved visual results and a 50% increase in young's modulus [130]. Importantly, this curing step does not affect the as-printed feature sizes. To reduce the surface tension during the drying process, Maruo et al. use supercritical CO_2 drying and showed no collapse in their nanopillar array compared to air drying [131]. These would be further avenues of investigation if shrinkage proves to be a major barrier to metamaterial functionality.

Finally, the example ascending scan array in figure 4.5 shows improved adhesion of the fallen lines for both arrays. For figure 4.5a the lines have fallen in place and would allow simple measurement of line height through an automated process such as that outlined in section 3.2.3. For scattered arrays, such as in figure 4.5b, the line heights could still be measured by hand since it is clear that those lines belong to that particular array compared to prior investigations where they are scattered across the whole substrate. However, the lines have scattered on top of the lower offset lines hindering line width measurements and so other methods of line height measurement should still be sought.

Stitching

The stitching investigation showed that fabricating each block in succession produces visible seams, as per figure 4.6a & reffig:stitchingc. Imprecision in the stage movements, along with any strut movement within the uncured resin lead to misalignment when fabricating the next block. Since the blocks are not well adhered, when the stresses from polymerisation are released during development, deformities occur. Fabricating a full stitched layer in one go, as in figure 4.6b, produces less visible seams compared with printing each woodpile block individually, with the trade off of increased fabrication times due to additional movement phases within the print.

Stage movements are a large contributor to the inaccuracies when stitching. In Buena et al. they discuss changing the NA of the objective to alter the writing field to reduce the necessity of stitching [121]. However, they note that there is a trade off between writing field and line dimensions. Therefore, when small feature sizes (100 nm $-$ 200 nm) are needed they suggest working on optimising the stitching process using the 63X/1.4 NA lens. The stage repeatability of the Nanoscribe system is given as $<1.5\mu$m which an order of magnitude larger than the features needing to be aligned. This could be addressed by hardware and/or software upgrades, however upgrades such as a higher precision mechanical stage would be difficult to realise with a commercial system. Nanoscribe have recently introduced their Nanoguide online support system with useful advice for users. In their article regarding stage movements and stitching they recommend adding a backlash correction of 50 μm to take up the slack of the stage as it changes directions. This is an avenue of further investigation for this work when larger area lenses are required.

Nanoscribe have also recently launched their large feature set printing which uses a 10X objective to enable printing within a single 1 mm diameter area of structures up to 8 mm in height [132] removing the need for stitching most structures. However, this method requires the use of a new resin, IP-Q, which has a 12:1 voxel height to width ratio which is less suited to single line printing, in addition to having a larger voxel width which would increase the operational wavelength of the metamaterial. Other stitching methods could be used, such as Oakdale et al. who employed an interdigitated stitching method for woodpile structures [133]. A set of blocks with twice the desired pitch are fabricated next to each other, then blocks with a 0.5× dimensional offset were printed within the first set of blocks so that the stitching seams were completely enveloped producing more mechanically sound structures.

4.4.2 Geometry Alteration Investigation

In Figure 4.7 the lines clearly increase in width with increasing power as expected. The resulting shapes of the woodpiles in figure 4.8 are in line with expectations based on how line widths change with laser dose. Figure 4.8a shows a shape that bulges towards the central points on the perimeter where the power is higher and thus the line widths are bigger, this is also shown in figure 4.8b. In figure 4.8c and d the woodpiles taper towards the end where lines are fabricated with the lowest powers.

In figure 4.9b, it seems that the user defined power profile did not reach its minimum value at the end point as the final segment on the right is not as thin as the first segment on the left. Upon further investigation of the print file, the DeScribe rendering shows that the profile along the line is shifted so that the maximum is not in the central segment. Therefore, this issue should be fixed with more careful programming that accounts for there needing to be an equal number of steps up as there are down.

A segment overlap was implemented in figure 4.9b to improve continuity of the line compared with figure 4.10. In this figure, the x-oriented lines show clear divisions due to the rounded edges of the lines; these edges are due to the elliptical nature of the voxel. Yet, the separation is less pronounced in the y-oriented lines compared with the x-oriented lines. This may be due to differences in movement accuracies of the galvo-scanner in the two directions. A further investigation to allow a more thorough understanding of these differences would allow for more accurate precompensation in the design.

Despite the segment overlap in figure 4.9b, the different segments are still clearly visible due to the size mismatch of the voxels. Splitting the lines into smaller increments would allow for a smoother profile, however for metamaterial applications the length need only be as small as the unit cell size to avoid unnecessary processing.

The woodpiles in figure 4.11 have shapes in line with the power profiles implemented. In figure 4.11a, the woodpile tapers in the bottom left corner where the power is lower. And in figure 4.11b the tapering is around the whole outer edge, with a bulging centre where the larger line widths are. It should be noted that for figures 4.8 & 4.11 there is some uncertainty in the overall shape of the structure due to any shrinkage that would have occurred. A frame was not used here so as not to interfere with any alterations due to the power profiles.

While the woodpile structure is not the focus of this work, gradient woodpiles are useful within the field of electromagnetics research [134]. Nonetheless, the results in this section showed that TPP can create gradient structures by altering the laser parameters to alter the feature sizes.

4.4.3 Cylindrical Fishnet Discussion

The cylindrical fishnet structure was designed based on the results from the previous sections in this chapter. A circular structure was likely to be more resilient to the stresses released during development thus reducing the amount of shrinkage, however a pattern of concentric rings alone would collapse in on itself. Therefore, the spokes between the rings were added for stability. Initial calculations for a structure with 8 starting spokes and a line width of 500 nm showed that increasing the number of spokes between each successive ring by N ± 2 (where N = 8) held the filling fraction constant across the structure. The specific number of spokes to increase by varied ring-to-ring, and may also depend on the line width and number of starting spokes. Therefore, the decision was made to simplify the process to just increase by the number of starting spokes between each ring instead of calculating the specific increase between each ring for each dose and starting spoke combination.

The cylindrical fishnet in figure 4.12 shows good structural fidelity with little to no deformation during development. However, as shown in figure 4.13, there can sometimes be issues of separation within the print. A frame was used to see if this eliminated the problem but as per figure 4.13b it did not. The magnified image in figure 4.13c shows misalignment of the spokes and rings, whereby the centre of the spokes sits on a ring, rather than being attached to a ring at each end. This appears to get worse at the outer edge of the structure, and for spokes that are on a diagonal rather than a horizontal or vertical path.

For each layer in the structure, all rings are printed from the centre to the outer edge, followed by the spokes again starting at the centre. The separation may be due to inaccuracies realigning the laser to the centre of the structure causing increased misalignment from the centre outwards. Another reason may be warping as the number of layers increases, causing the rings to deviate from their programmed position. One way to fix this may be to change the scan pattern so that the spokes and rings are written in an alternating pattern rather than each at once. However, this will likely increase the fabrication time.

The cylindrical fishnet structure provides multiple ways to alter the geometry across the device including; changing the line width of the rings/spokes, changing the number of spokes within a particular region, and changing the length of the spokes (corresponding to the gap between each ring). Figures 4.14 & 4.15 show the geometry variation achievable by changing each of these parameters. The lower fill fraction resulting from longer spokes, fewer dividing spokes, and smaller line widths, should result in a lower RI, whereas a higher fill fraction would result in a higher RI. Of course, the geometry itself will also play a role in the resulting effective refractive index, values of which will be explored in chapter 5. Finally, while changing the spoke length is a legitimate strategy for altering the refractive index, it presents continuity issues in the structure if the gap between the rings means that there is not a discrete number of rings within the size of the RI region. As such, the spoke length / ring spacing is set at 1 μm, chosen so that both the cured lines and gap spacings are smaller than the operational wavelength while maintaining resolvability.

Figure 4.16 shows the stitched single layer of concentric rings as a first step towards a stitched cylindrical fishnet. As previously discussed, the stage movement inaccuracies present a large barrier to a homogeneous stitched structure. The patch work pattern is due to differences in finding the interface in each block so that an interface may be found lower into the substrate than a previous section resulting in height differences across the structure. This may cause issues when building upwards such that the second layer may not completely adhere to the first if the spacing between the layers is too large resulting in an unstable structure. Additionally, this is just a pattern of concentric rings, and building further out, as well as programming the spokes is a mathematical challenge for the programming of the structure which must be overcome for printing larger area cylindrical fishnet structures.

4.5 Summary

- The combination of frames for support and silanized glass slides for improved adhesion resulted in less shrinkage for woodpile structures.
- The silanized slides promoted better adhesion of fallen lines for the ascending scan pattern, however further methods of measuring line height should be sought as the scatter of the lines still prohibited both line width and height measurements.
- Stitching a whole layer in one go creates a more homogeneous structure than printing a full block at a time, with the trade off of increased fabrication time.
- The geometry of a structure fabricated by TPP can be altered by changing the laser scan speed and laser power. This can be done by changing the power between each line, or along a single scan line with either the in-built linear function or with a user defined power profile.
- The designed cylindrical fishnet structure shows less shrinkage compared to equivalently size woodpile structures with the benefit of multiple ways to alter the unit cell to change the RI. In addition, the cylindrical fishnet can be easily compared to traditional GRIN rod lenses for focal length analysis.

The main outcome of this chapter was an understanding of the structural fidelity and repeatability of structures fabricated by TPP. Since both a commercial system and resin were used there were limitations in what could be altered to address the problems exhibited surrounding stitching errors and shrinkage. In the future, the use of a home built system may be of interest to allow more control over the printing process, in addition to formulating a custom resin designed to combat shrinkage. The main results that have been taken forward is the design of the cylindrical fishnet structure which will be used as the basis for calculations and simulations in chapter 5, and the updated dose region (and thus available line widths) for this structure.

Chapter 5

Metamaterial Unit Cell Characterisation

5.1 Introduction to Unit Cell Characterisation

In order to design the GRIN lens, the effective RI (n_{eff}) of the unit cell (UC) should be known for each geometrical variation. In this chapter, analytical calculations are conducted using the Maxwell-Garnet theory [51] for cylindrical fishnet UCs, and a rectangular cut-out approximation, with different line widths and spoke distances. The analytical calculations are used to select a number of UCs to simulate in COMSOL allowing an understanding of how the geometry affects n_{eff} also. The analytical and simulated results are compared to the ideal stepped hyperbolic secant profile [13]. The main outcome of this chapter is a list of achievable n_{eff} values for different UC geometries.

5.2 Unit Cell Investigation Methodology

5.2.1 Analytical Calculations

A common approximation theory for effective optical parameters is the Maxwell-Garnett theory (MGT) [1] where the Maxwell-Garnett equation is given by,

$$\frac{(\varepsilon - \varepsilon_h)}{(\varepsilon + 2\varepsilon_h)} = \mathrm{ff}\frac{(\varepsilon_1 - \varepsilon_h)}{(\varepsilon_1 + 2\varepsilon_h)}, \tag{5.1}$$

where ε is the effective permittivity of the composite material, ff is the filling fraction, ε_h=1 is the relative permittivity of air and $\varepsilon_1 = \mathrm{n}_1^2 = 1.492^2$ is the relative permittivity of the IP-L at λ =1500 nm as in [135]. The geometry is a circular UC representing the cylindrical fishnet structure used in this work (figure 5.1a).

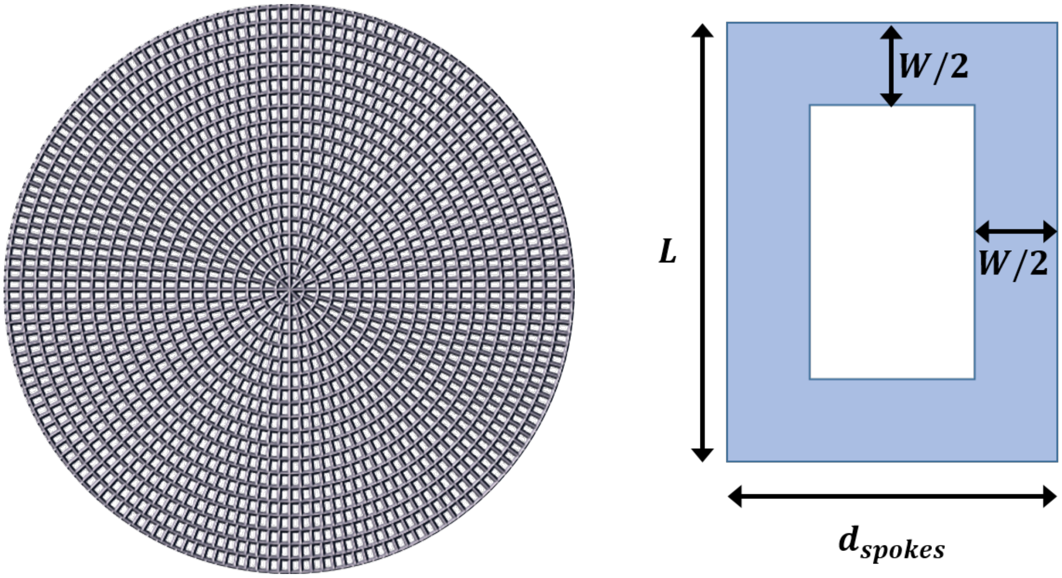

(a) (b)

Figure 5.1: (a) A rendering of the cylindrical fishnet structure (r = 20 μm for illustrative purposes). (b) Approximated rectangular cut out UC. L is the spoke length, d_{spokes} is the distance between adjacent spokes (defined in appendix B.2), and W is the line width.

A 2D matrix of n_{eff} values is created by rearranging equation 5.1 for $\sqrt{\varepsilon}$ and varying the fill fraction by changing the line width (W) and the number of starting spokes (S). The line width values are imported from the results in the study outlined in chapter 3. The spoke length, corresponding to the gap between each ring, is set to L = 1 μm. Finally, the number of starting spokes is varied between S = 2 to 10, and the number of spokes is increased by that same amount between each successive ring (as previously discussed in section 4.4.3).

The fill fraction is equal to the cross-sectional area of resin normalised to the full UC area. For the first UC type the area is a circle of diameter d = 200 nm corresponding to the largest print area possible in the TPP set up. The cross sectional area of the cylindrical fishnet lens is worked out using the calculation outlined in appendix B.1.

Using the analytical n_{eff} data set, four different hyperbolic secant (sech) profiles were created, corresponding to the four lenses to be investigated in chapter 6. For lens 1, the sech curve is normalised so that the maximum value corresponds to a solid block of resin (n = 1.492) and the minimum value is the smallest value in the data set. Lens 2 normalises the sech curve to the maximum and minimum values from the data set as calculated. Lens 3 changes the line width only and holds the “starting spokes” constant, and lens 4 changes the number of spokes in each region holding the line width constant. As such, for these last two lenses the data set was searched for the number of spokes (lens 3), or the line width value (lens 4), that provided the greatest difference in refractive index when changing the other parameter.

Following normalisation, one half of each sech curve is discretised into 7 values and the data set is searched for the closest matching value for each discrete region. Where two combinations produced the same result, the faster scan speed was chosen with increased fabrication efficiency in mind. The 4 sets of UCs were then taken forward to simulate in COMSOL.

The COMSOL simulations make use of a simplified geometry which is a rectangular UC with a rectangle cut out, shown in figure 5.1b, which is an approximation to the air region between two spokes. The analytical calculations are run again, using the area calculation for this geometry shown in appendix B.2. The RI values corresponding to the prior selected UCs are found to allow comparison between the two analytical results and the simulations.

5.2.2 Simulation and Retrieval Method

The COMSOL simulations are undertaken to get a more accurate representation of the effective RI compared to analytical calculations alone. However, care must be taken to ensure both the computational model and the parameter retrieval process are correct so that the results are trustworthy. Appendix C highlights the validation methods, where a uniform dielectric slab was simulated to ensure the retrieved RI is constant across the frequency range simulated. This section of work presents the final methods used to gather the UC results.

The COMSOL Model

While there are many electromagnetic field solvers on the market which can and have been used to simulate metamaterials, COMSOL was used in this work based on existing licence availability. The simulation was based on a webinar hosted by COMSOL [136]. Figure 5.2 shows the domains and boundary conditions applied to the model. The central grey chequered region contains the structure under investigation with the rest of the simulation domain being filled with air.

Floquet-periodic boundary conditions (PBCs) are used to simulate an infinite material and/or 2D array of UCs. The PBCs are set up so that opposing faces are paired as source and destination boundaries. This enables the physics-controlled meshing sequence to create identical surface meshes on the paired boundaries. All simulations used the "extremely fine" mesh setting to minimise errors across the simulation domain. The port boundary conditions are placed on the outside boundaries of the simulation domain to automatically determine the transmission (S_{21}) and reflection (S_{11}) coefficients for each frequency. The excitation is turned on in the upper port and has a power of $\mathbf{P_{in}}$ = 1 [W] and a linearly polarised electric field of $\mathbf{E_0}$ = 1 $\bar{\mathbf{x}}$ [V/m]. The bottom port is the listener port where the radiation is absorbed (excitation turned off). These ports are periodic, diffraction order and orthogonal polarization ports, representing plane waves propagating in the direction of the diffraction orders with respect to the Floquet periodicity.

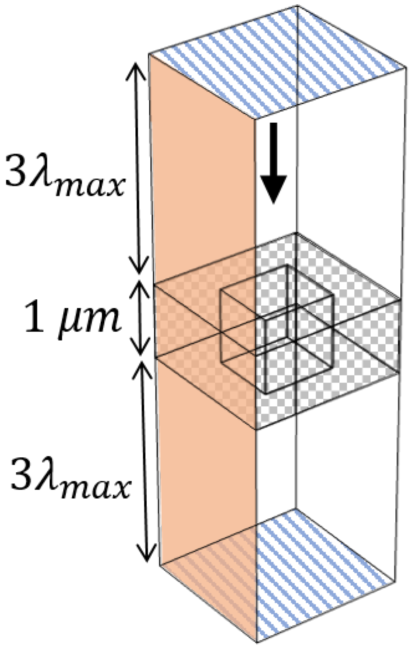

Figure 5.2: COMSOL boundary conditions. Blue stripes are the periodic ports exciting a wave travelling from top to bottom (indicated by black arrow). Orange shaded is the Floquet periodic boundary condition applied in pairs to opposing vertical faces. The grey chequered central region is the rectangular cut out geometry with IP-L material definition n = 1.492 [135], $\varepsilon = \text{n}^2$ and $\mu = 1$. There is a $3\lambda_{max}$ gap between the ports and the structure surfaces which is filled with air, and the thickness of the structure is 1 μm.

Parameter Retrieval Method

To obtain the effective parameters of the metamaterial, a parameter retrieval process is used on the transmission and reflection results from either computational or numerical calculations. The majority of papers in the literature use either the Smith [137] or Chen [138] retrieval methods. This work is based on the Chen method which will be described here.

For a plane wave at normal incidence on a homogeneous material slab of thickness d, S_{11} is equal to the reflection coefficient, and S_{21} is related to the transmission coefficient T by $S_{21} = Te^{ikd}$ where k is the wave number of the incident wave in free space. The S-parameters relate to the refractive index and the impedance by,

$$S_{11} = \frac{\mathcal{Z}(1 - e^{i2nkd})}{1 - \mathcal{Z}^2 e^{i2nkd}} \tag{5.2a}$$

$$S_{21} = \frac{(1 - \mathcal{Z}^2)e^{inkd}}{1 - \mathcal{Z}^2 e^{i2nkd}} \tag{5.2b}$$

where $\mathcal{Z} = z - 1/z + 1$. By inverting these equations the following is obtained,

$$z = \pm\sqrt{\frac{(1 + S_{11})^2 - S_{21}^2}{(1 - S_{11})^2 - S_{21}^2}} \tag{5.3a}$$

$$e^{inkd} = X \pm i\sqrt{1 - X^2}, \tag{5.3b}$$

where $X = 1/2S_{21}(1 - S_{11}^2 + S_{21}^2)$, allowing the calculation of z and n. As this work deals with a passive medium the signs are determined by the following requirements,

$$z' \geq 0 \tag{5.4a}$$

$$n'' \geq 0 \tag{5.4b}$$

where $(\cdot)'$ and $(\cdot)''$ denote the real and imaginary part operators. The refractive index is determined from equation 5.3b as,

$$n = \frac{1}{kd}\Big\{ \big[[\ln(e^{inkd})]'' + 2\pi m\big] - i\big[\ln(e^{inkd})\big]' \Big\} \tag{5.5}$$

where m is an integer value related to the branch index of n' arising due to the logarithmic function; resolving this will be discussed shortly.

It is common to determine z and n independently using equations 5.3a & 5.3b along with requirements the equations 5.4a & 5.4b. However, this may lead to issues when z' and n'' are close to zero as small perturbations in the S-parameters lead to unreliability in applying the sign requirements. Therefore, the relationship between z and n should be used to determine the signs.

In order to determine the correct sign of z there are two cases: (1) where $|z'| \geq \delta_z$ where equation 5.4a is applied, and (2) for $|z'| < \delta_z$. In the second case, the sign of z is determined so that n'' is non-negative or equivalently $|e^{inkd}| \leq 1$. Here, δ_z is a small positive number and is set to δ_z = 0.1 in this work. Additionally, a new equation for n is derived from equations 5.2a & 5.2b achieving,

$$e^{inkd} = \frac{S_{21}}{1 - S_{11}\frac{z-1}{z+1}}. \tag{5.6}$$

This allows the sign ambiguity in equation 5.3b to be avoided since it can be proved that only one sign of the imaginary part of equation 5.3b makes it equivalent to equation 5.6 [138].

The Chen method of resolving for the first branch requires a value of m to be found for which,

$$|n'z''| \leq n''z'. \tag{5.7}$$

However, while Chen discussed the existence of a resonance band for which no value of m satisfies this relationship, there are other frequencies outside of the resonance band for which m also cannot be found. As such, the Wang method [139] was used to resolve the branching in this work. For the first branch,

$$m_0 = \text{Round}\Big\{ -\frac{1}{2\pi}\big[\ln(e^{inkd})\big]''\Big\}, \tag{5.8}$$

where $Round\{\cdot\}$ is an operator that rounds its argument to the nearest integer value. The argument is defined as V_0 for simplicity. Having obtained the initial branch index and using equation 5.5 to calculate n_0, subsequent branch indices are found by,

$$V_i = -\frac{1}{2\pi}([\ln(e^{in_{i-1}k_{i-1}d}]'' - [\ln(e^{in_ik_id}]''), \tag{5.9a}$$

$$m_i = \text{Round}\{V_i\}, \tag{5.9b}$$

where i is the current branch being resolved at frequency f_i. This ensures continuity of the retrieved refractive index.

5.2.3 Computational Effective RI

Unit Cell Simulations

Simulating the full cylindrical fishnet structure was found to be too computationally expensive to run due to hardware limitations. As such, the simulations here use the rectangular cut out geometry shown in figure 5.1b. The simulation approximates an infinite 2D array of the rectangular cut out extruded to 1 μm depth, which is now a fishnet structure proper rather than the cylindrical fishnet. The simulation is run for each of the selected UCs for a frequency range between f = 100 THz to 300 THz in 1 THz steps with an "extremely fine" physics-controlled mesh. The results are saved in a text file to be imported into MATLAB for the parameter retrieval process. A graphs of the real RI vs frequency were plotted, allowing the identification of the effective region for the metamaterial for which the RI is constant. These simulation results are compared to the analytical results to assess how well the analytical predicted the simulation results.

Rotation Study

Since the simplification in geometry now simulates a square array rather than the circular cylindrical fishnet structure, an investigation is undertaken into how this might affect the resulting RI of the unit cells. In particular, in the cylindrical fishnet structure, UCs are rotated around the centre of the circle such that they will interact with linearly polarised light in different ways. To investigate this further, three UCs are selected with differing amounts of asymmetry, and linearly polarised light is rotated through 90° in steps of 0.01°. To do this, the electric field was changed to $\mathbf{E_0} = \cos\phi\,\mathbf{x} + \sin\phi\,\mathbf{y}$.

5.3 Results

5.3.1 Analytical Effective RI

The analytical effective RI results for the cylindrical fishnet structure are shown in figure 5.3. This is after the removal of the dose and spokes combinations presented in section 4.3.3. The maximum RI is n_{eff} = 1.4613 for S = 10 and W = 548 nm (SS = 100 μm s^{-1} & LP = 15 mW), and the minimum RI is n_{eff} = 1.1519 for S = 2 and W = 273 nm (SS = 50 μm s^{-1} & LP = 5 mW).

Figure 5.4 shows the resulting sech profiles and the RI for the selected UCs for each lens using the analytical RI results. Table 5.1 summarises the selected UCs, where a UC refers to a spoke and line width combination, for which 22 unique combinations were selected. The table also shows the corresponding analytical refractive index for the rectangular cut out approximation for comparison.

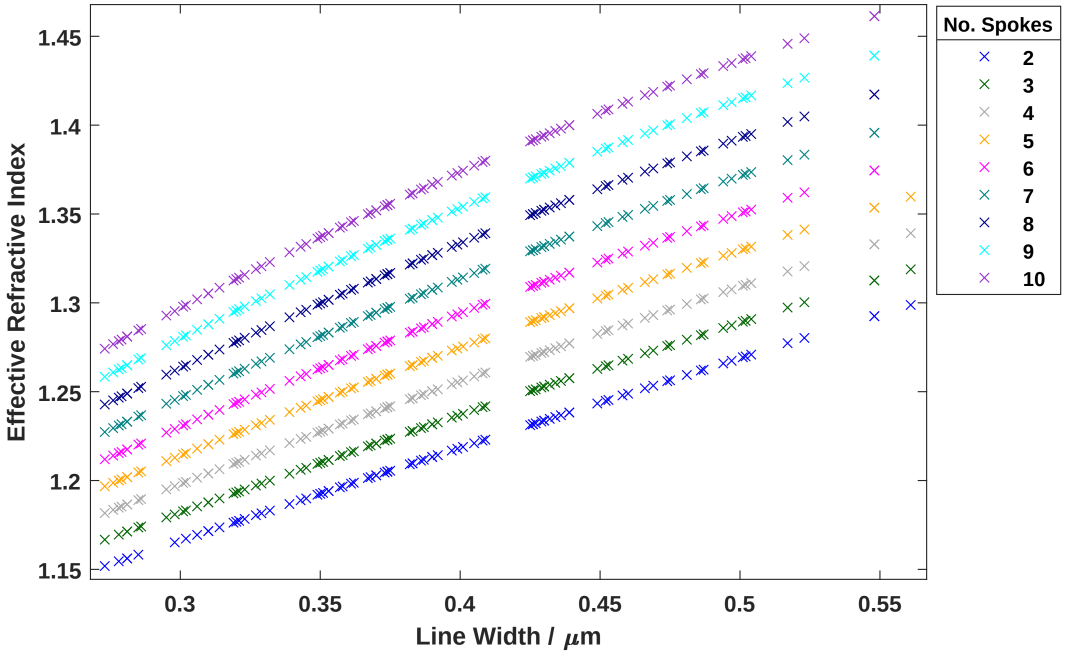

Figure 5.3: Analytical effective refractive index against line width for different numbers of starting spokes.

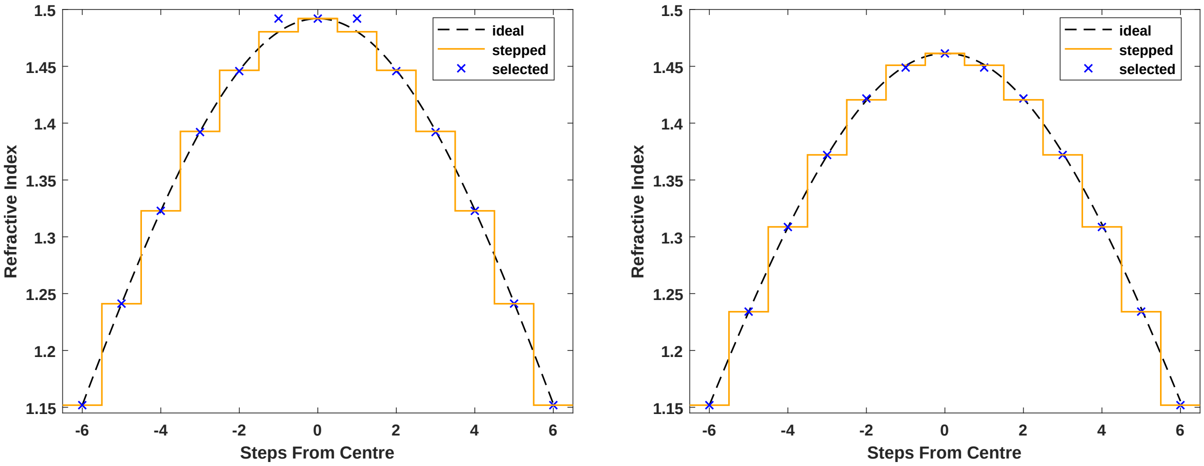

(a) Lens 1

(b) Lens 2

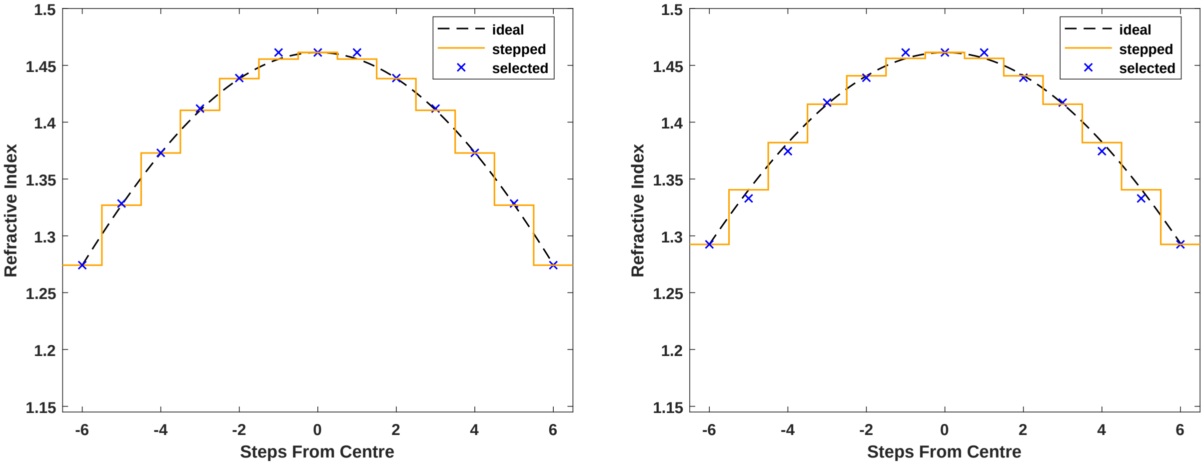

(c) Lens 3

(d) Lens 4

Figure 5.4: (a) – (d) show the ideal and stepped RI profiles along the y axis in steps of unit cell width, b. The corresponding RI values for the selected unit cells are shown also.

Table 5.1: A table showing the selected unit cells (spokes and line width combination) based on the analytically calculated effective refractive index values. The final column indicates which unit cells are a repeat and need only be simulated once where the number indicates which repeat it belongs to.

Lens	RI			Δn_{ideal}	Starting Spokes	Line Width (nm)	Repeat?
	Ideal	Selected	Rectangle				
1	1.492	1.492	1.492	0.340	Solid Block		R1
	1.480	1.492	1.492		Solid Block		R1
	1.447	1.446	1.441		10	517	
	1.393	1.392	1.388		10	427	
	1.323	1.323	1.320		5	487	
	1.241	1.241	1.239		4	374	
	1.152	1.152	1.151		2	273	R2
2	1.461	1.461	1.457	0.309	10	548	R3
	1.451	1.449	1.444		10	523	
	1.421	1.422	1.417		10	474	
	1.372	1.372	1.369		7	501	
	1.309	1.309	1.305		7	392	
	1.234	1.234	1.232		5	332	
	1.152	1.152	1.151		2	273	R2
3	1.461	1.461	1.457	0.187	10	548	R3
	1.456	1.461	1.457			548	R3
	1.438	1.439	1.434			504	
	1.411	1.412	1.407			458	
	1.373	1.373	1.369			399	
	1.327	1.329	1.324			339	
	1.274	1.274	1.271			273	
4	1.461	1.461	1.457	0.168	10	548	R3
	1.456	1.461	1.457		10		R3
	1.441	1.439	1.435		9		
	1.416	1.417	1.413		8		
	1.382	1.374	1.371		6		
	1.341	1.333	1.331		4		
	1.293	1.293	1.291		2		

5.3.2 Computational Unit Cell RI Results

Figures 5.5 $-$ 5.8 show the effective RI against frequency for each of the UCs relating to a particular lens. While not used for these lenses, the retrieved dielectric slab RI is also shown on figures for Lenses 2 $-$ 4 for comparison. On each figure the effective regime is clearly demonstrated by the continuous RI with a slight dispersion relation. This regime has a nominal cut off at around 200 THz, although some UCs have regions of resonance before that.

These figures also show the expected pattern of a decreasing UC RI with decreasing fill fraction (the legends list the UCs from highest to lowest filling fraction). UCs with smaller air gaps have a larger effective regime and smoother curves with fewer resonances within the effective regime. Table 5.2 provides the analytical and simulated UC results and the corresponding RI difference for that particular lens. Simulated results are taken from the data set at f = 150 THz, as this is comfortably in the effective region for all four lenses without being too close to any resonances.

Figure 5.9 shows the ideal (analytical) stepped RI profile for each of the four lenses with the analytical and the simulated UC results for each region. The simulated results are generally higher than expected at the outer edges, and closer to expected towards the central region. Figure 5.10 shows this discrepancy with respect to the fill fraction, where the simulated results are plotted with respect to the rectangular cut out fill fraction. For lower fill fractions the RI is higher than expected, but higher fill fractions see an RI close to predicted.

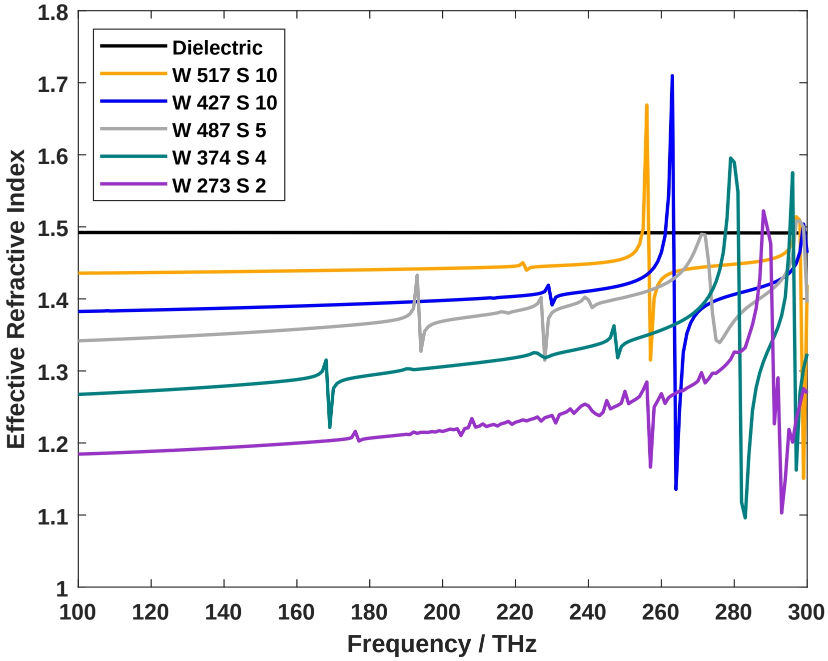

Figure 5.5: Effective RI for Lens 1 unit cells where W is line width and S is number of spokes

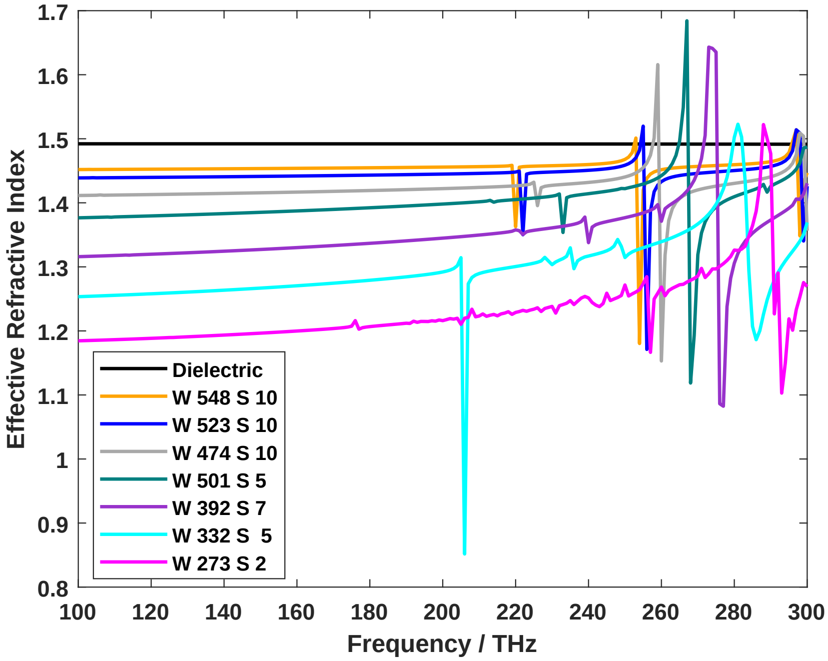

Figure 5.6: Effective RI for Lens 2 unit cells where W is line width and S is number of spokes (dielectric slab shown for comparison).

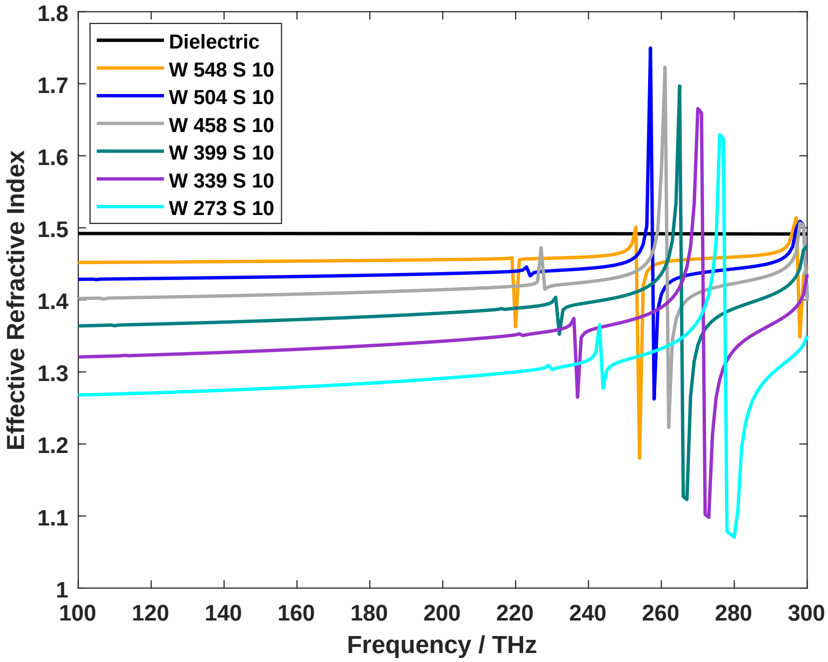

Figure 5.7: Effective RI for Lens 3 unit cells where W is line width and S is number of spokes (dielectric slab shown for comparison).

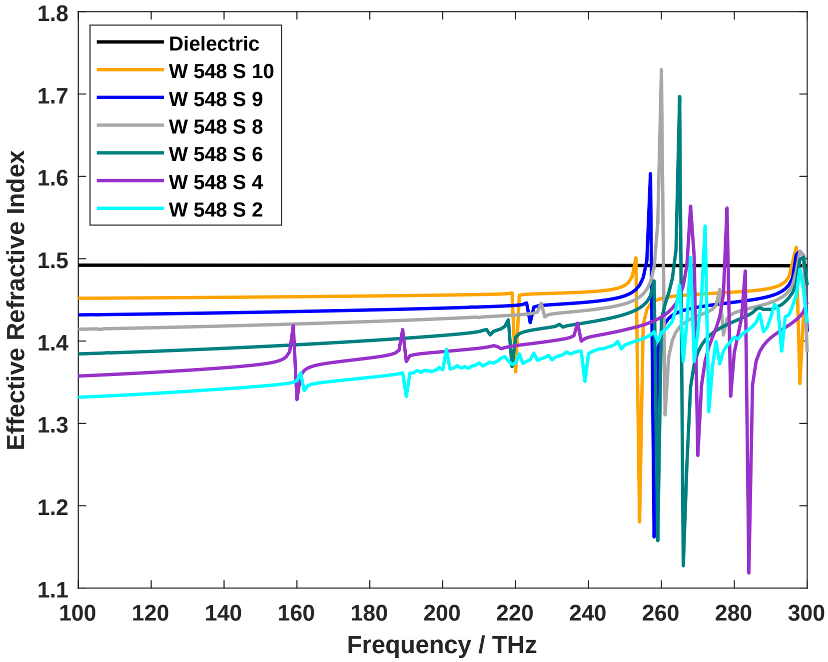

Figure 5.8: Effective RI for Lens 4 unit cells where W is line width and S is number of spokes (dielectric slab shown for comparison).

Table 5.2: A table showing the analytical and simulated unit cell results and the corresponding RI difference for each lens.

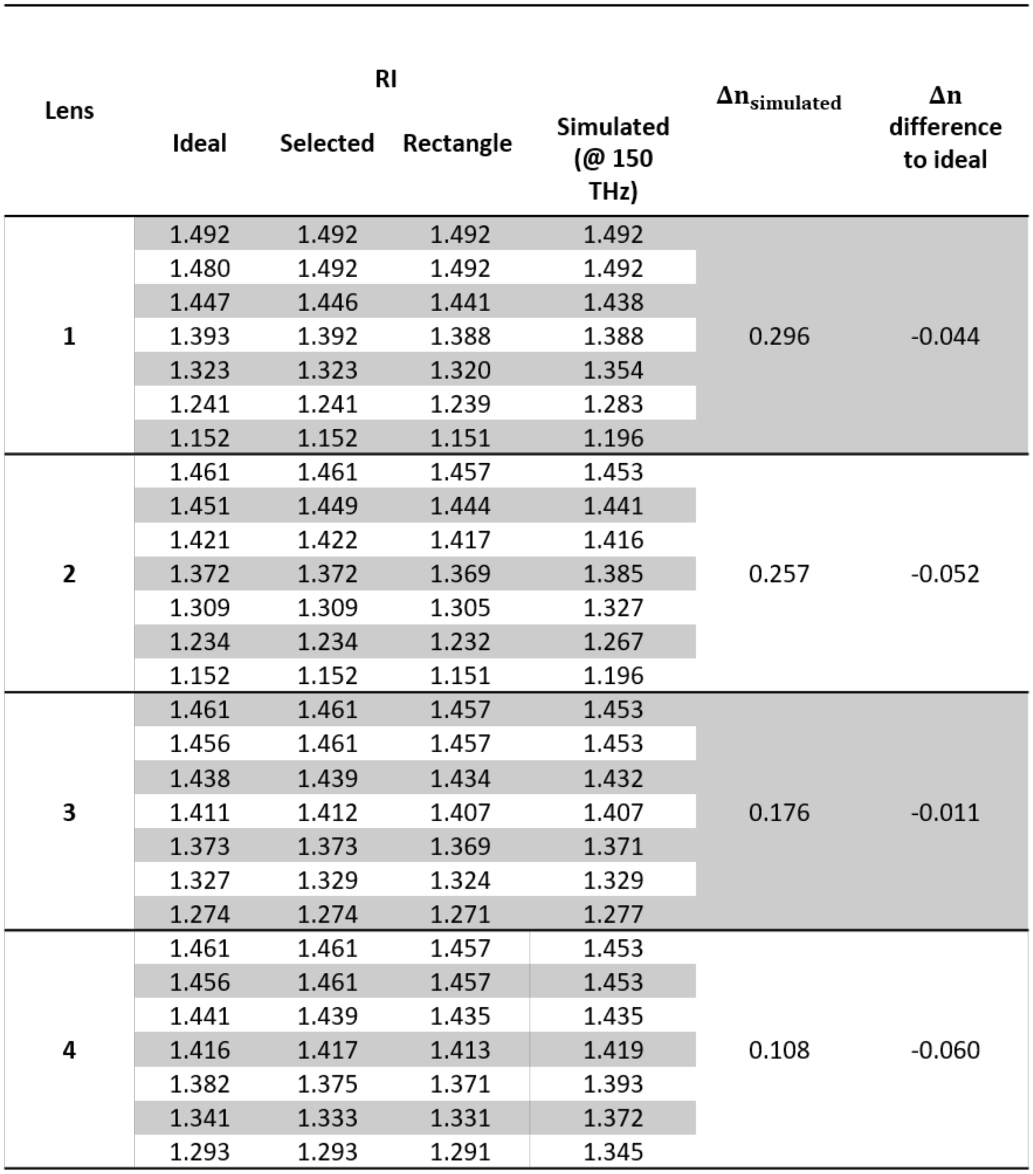

Lens	RI				$\Delta n_{simulated}$	Δn difference to ideal
	Ideal	Selected	Rectangle	Simulated (@ 150 THz)		
1	1.492	1.492	1.492	1.492	0.296	-0.044
	1.480	1.492	1.492	1.492		
	1.447	1.446	1.441	1.438		
	1.393	1.392	1.388	1.388		
	1.323	1.323	1.320	1.354		
	1.241	1.241	1.239	1.283		
	1.152	1.152	1.151	1.196		
2	1.461	1.461	1.457	1.453	0.257	-0.052
	1.451	1.449	1.444	1.441		
	1.421	1.422	1.417	1.416		
	1.372	1.372	1.369	1.385		
	1.309	1.309	1.305	1.327		
	1.234	1.234	1.232	1.267		
	1.152	1.152	1.151	1.196		
3	1.461	1.461	1.457	1.453	0.176	-0.011
	1.456	1.461	1.457	1.453		
	1.438	1.439	1.434	1.432		
	1.411	1.412	1.407	1.407		
	1.373	1.373	1.369	1.371		
	1.327	1.329	1.324	1.329		
	1.274	1.274	1.271	1.277		
4	1.461	1.461	1.457	1.453	0.108	-0.060
	1.456	1.461	1.457	1.453		
	1.441	1.439	1.435	1.435		
	1.416	1.417	1.413	1.419		
	1.382	1.375	1.371	1.393		
	1.341	1.333	1.331	1.372		
	1.293	1.293	1.291	1.345		

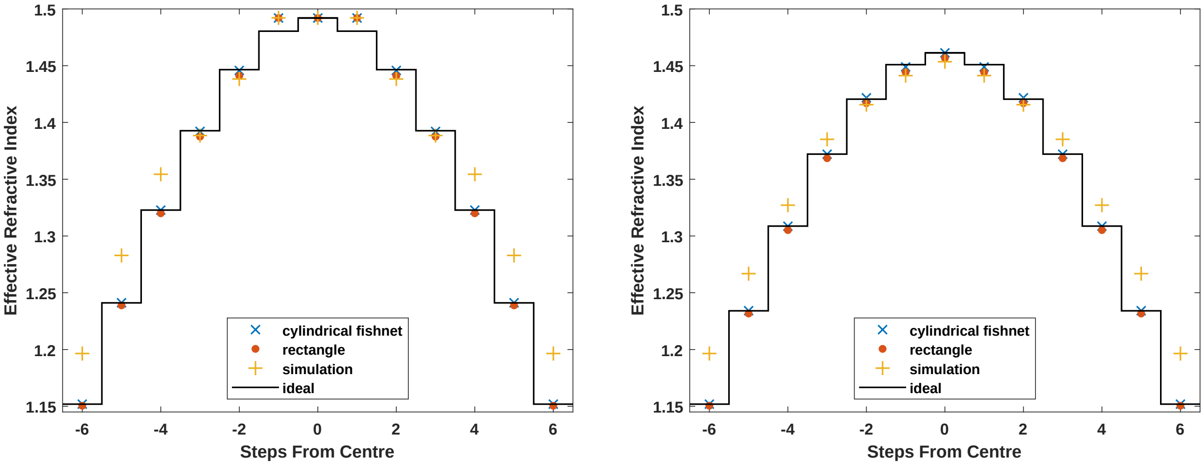

(a) Lens 1 (b) Lens 2

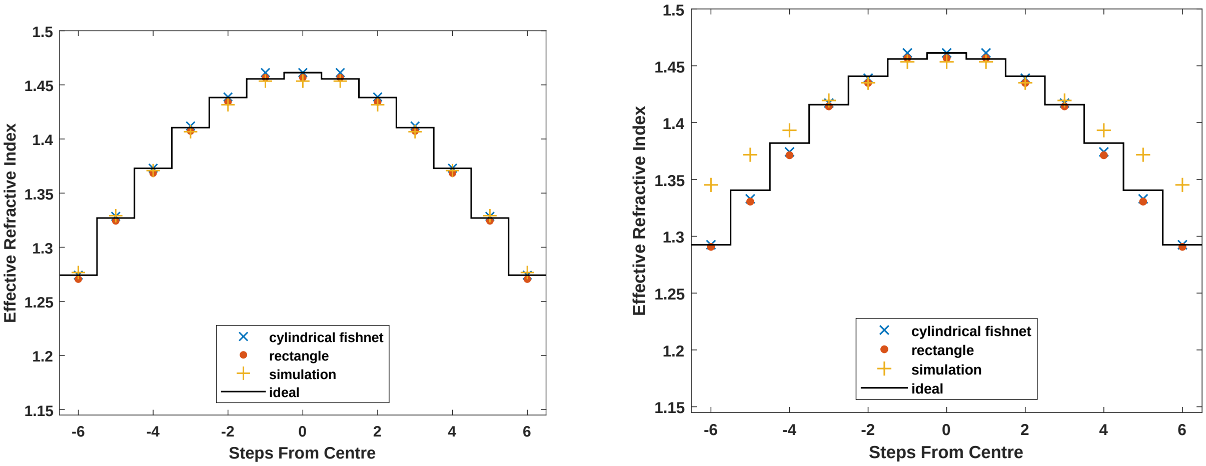

(c) Lens 3 (d) Lens 4

Figure 5.9: (a) – (d) show a comparison between the ideal stepped profile, the analytical results for the cylindrical fishnet and rectangular cut out approximation, and the simulated results at f = 150 THz.

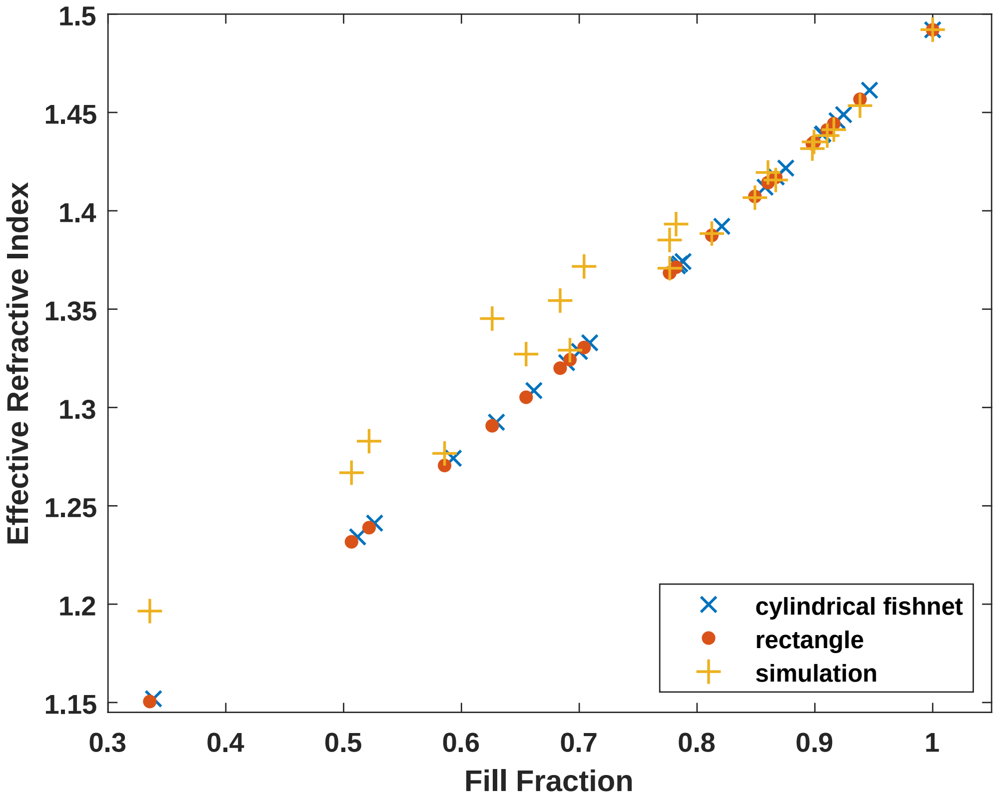

Figure 5.10: RI with respect to the unit cell fill fraction for the analytical and the simulated results.

5.3.3 Rotation Study

The three UCs used for the rotation study are shown in figure 5.11a−5.11c with the RI change against rotation angle shown in figure 5.11d. Table 5.3 shows the RI for ϕ = 0° and ϕ = 90° at f = 150 THz. Figures 5.12− 5.14 show the electric field norm for each of the unit cells for ϕ = 0° and ϕ = 90° at slices at 0 through the x,y, and z axis. The yellow regions show where the wave is tightly confined.

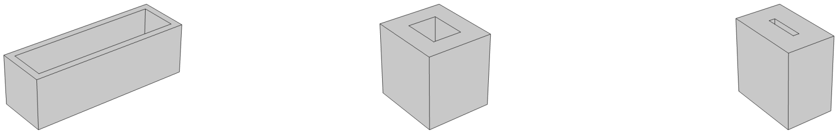

(a) W 273 S 2 (b) W 501 S 7 (c) W 548 S 10

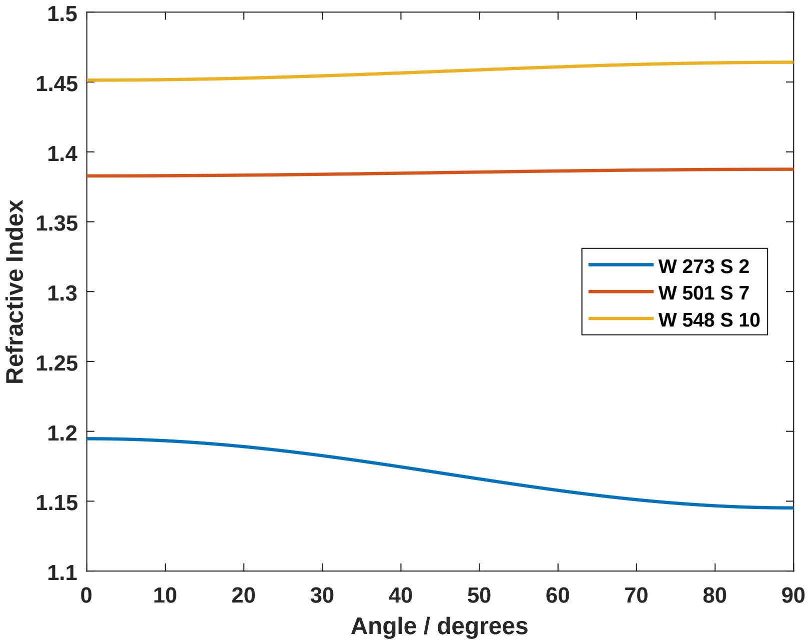

(d)

Figure 5.11: (a)−(c) unit cells used for rotation study undertaken at 150 THz, with retrieved RI against rotation angle shown in (d).

Table 5.3: RI at ϕ = 0° and ϕ = 90° for the three tested unit cells.

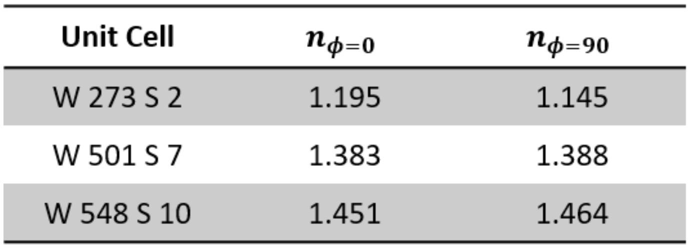

Unit Cell	$n_{\phi=0}$	$n_{\phi=90}$
W 273 S 2	1.195	1.145
W 501 S 7	1.383	1.388
W 548 S 10	1.451	1.464

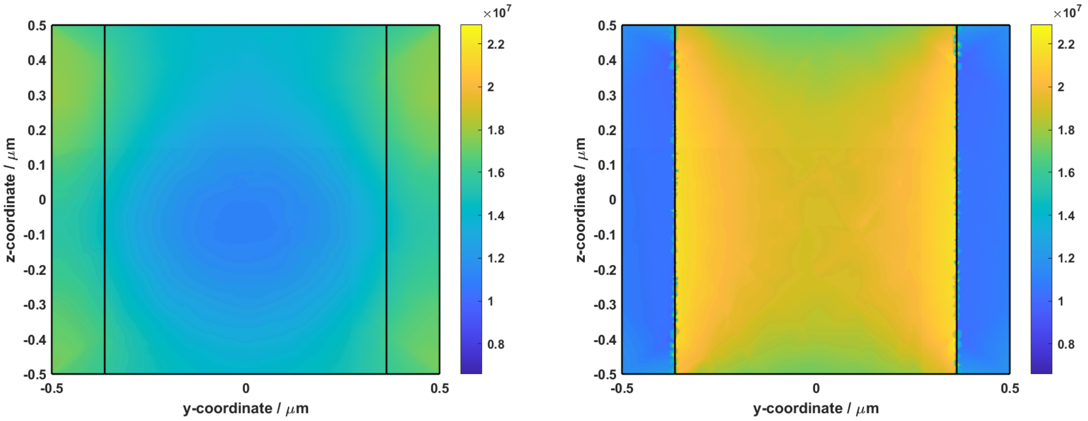

(a) x = 0, ϕ = 0° (b) x = 0, ϕ = 90°

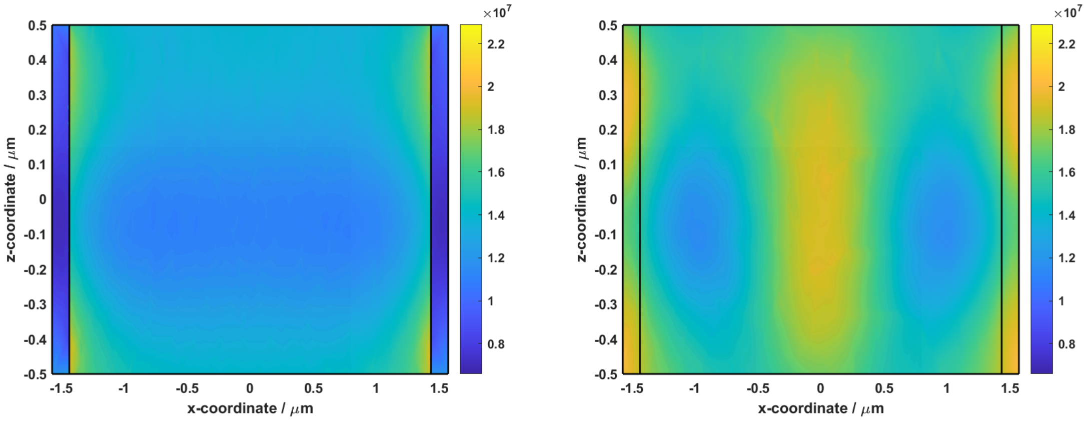

(c) y = 0, ϕ = 0° (d) y = 0, ϕ = 90°

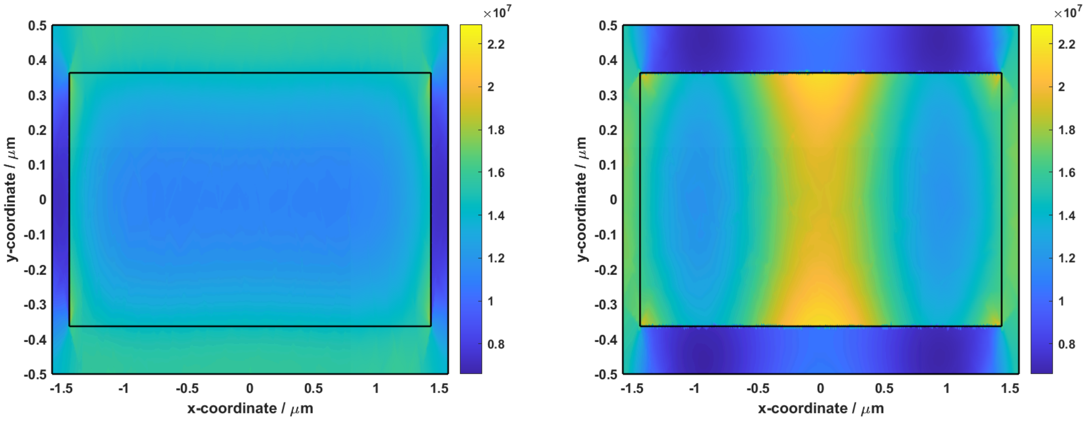

(e) z = 0, ϕ = 0° (f) z = 0, ϕ = 90°

Figure 5.12: Electric field normal for W 273 S 2 unit cell at $f = 150$ THz for slices through x = 0, y = 0, and z = 0 for both ϕ = 0° and ϕ = 90°.

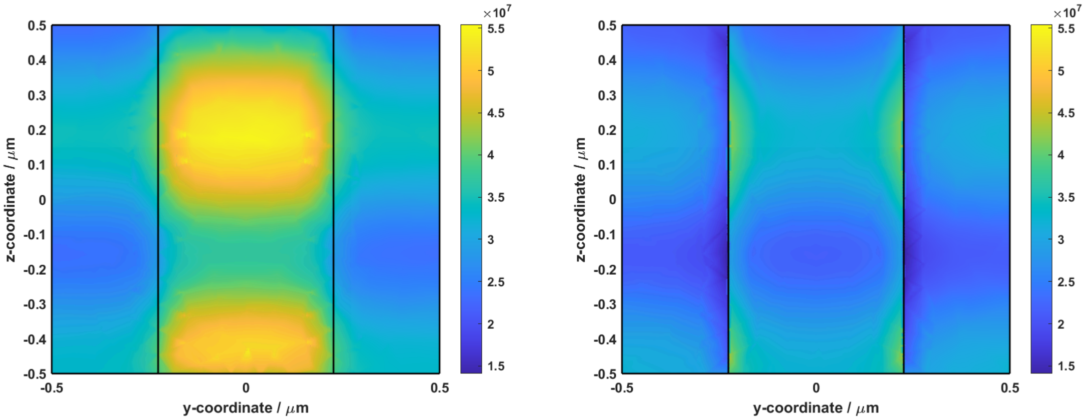

(a) x = 0, ϕ = 0°

(b) x = 0, ϕ = 90°

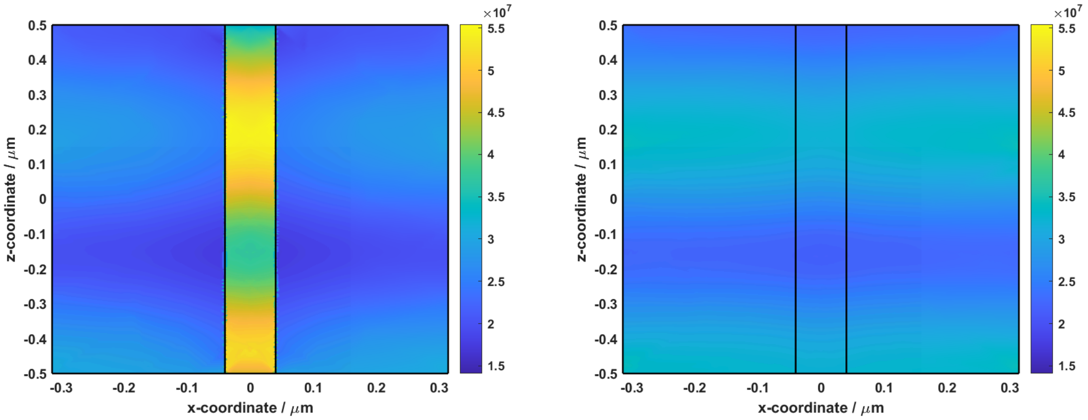

(c) y = 0, ϕ = 0°

(d) y = 0, ϕ = 90°

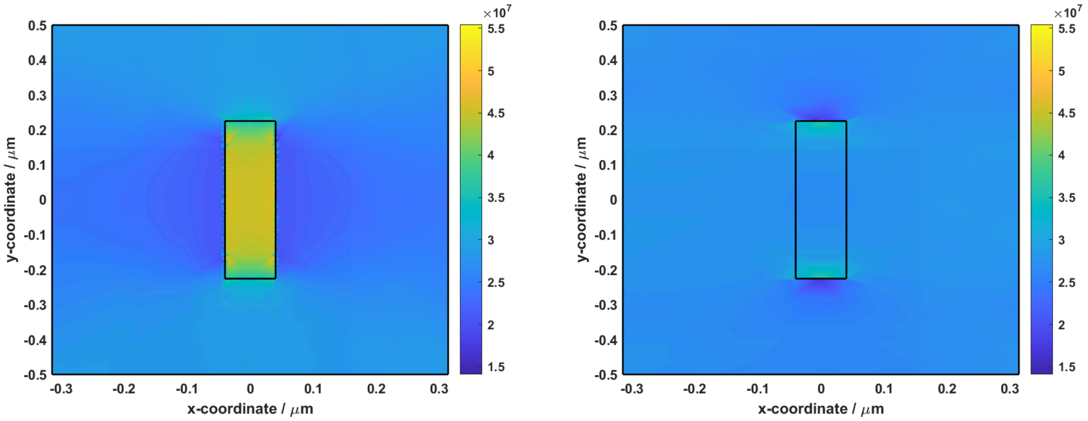

(e) z = 0, ϕ = 0°

(f) z = 0, ϕ = 90°

Figure 5.13: Electric field normal for W 548 S 10 unit cell at f = 150 THz for slices through x = 0, y = 0, and z = 0 for both ϕ = 0° and ϕ = 90°.

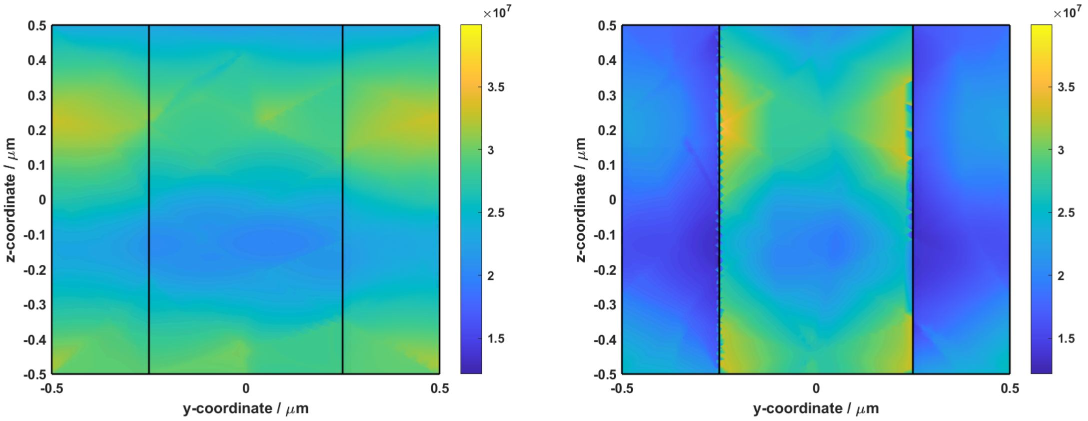

(a) x = 0, ϕ = 0° (b) x = 0, ϕ = 90°

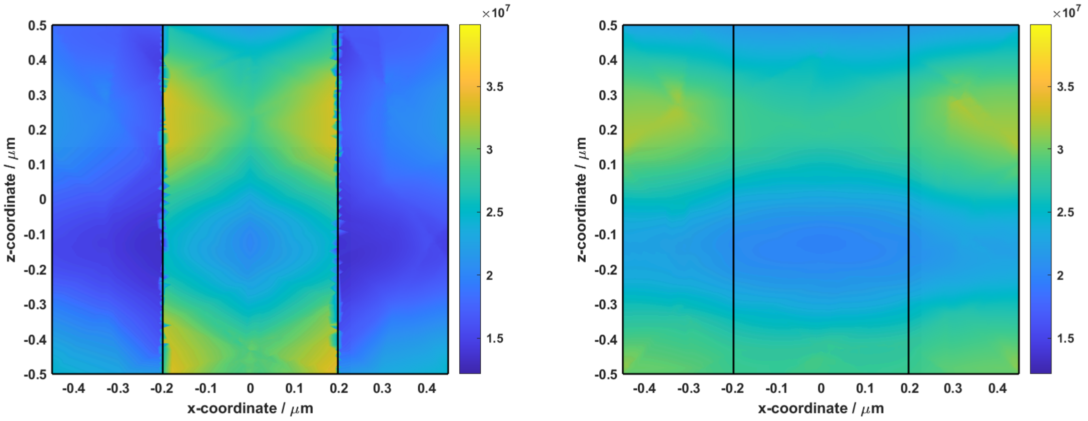

(c) y = 0, ϕ = 0° (d) y = 0, ϕ = 90°

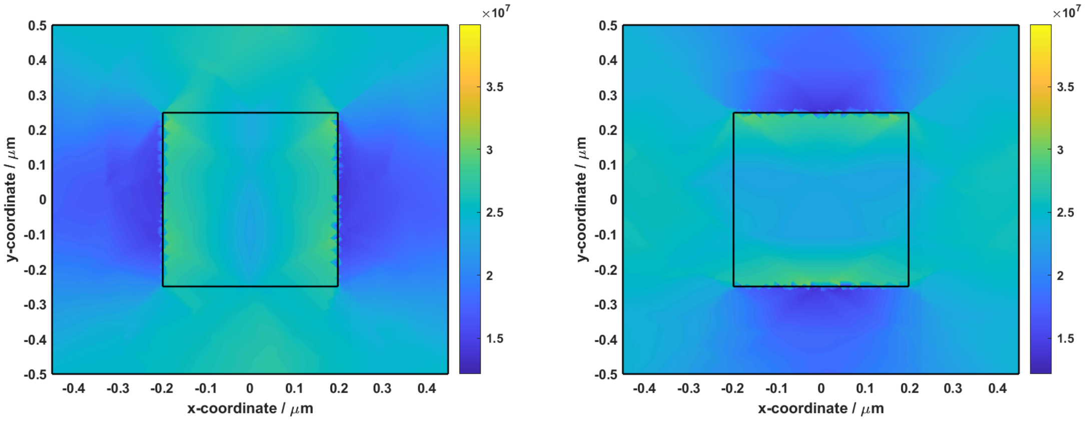

(e) z = 0, ϕ = 0° (f) z = 0, ϕ = 90°

Figure 5.14: Electric field normal for W 501 S 7 unit cell at $f = 150$ THz for slices through x = 0, y = 0, and z = 0 for both ϕ = 0° and ϕ = 90°.

5.4 Discussion

5.4.1 Analytical RI Calculations

The analytical effective RI results in figure 5.3 are as expected; as the line width and number of spokes increases, the fill fraction increases thus the RI increases. While MGT does not take into account the geometry of the metamaterial, these results provided a good basis for narrowing down the scope of the COMSOL UC investigation. Finding closest matching UCs for the four lenses designed in figure 5.4 narrowed down the 837 line width and spokes combinations to a more reasonable 22 unique combinations (where three UCs were shared across the lenses and thus only needed simulating once).

The lens profiles in figure 5.4 have the same y-axis scale for ease of comparison, and are as expected based on how Δn changes for each lens. Lens 1 has the highest Δn at 0.340 and has a steeper gradient, while Lens 4 has the smallest at $\Delta n = 0.168$ with the shallowest slope. A smaller Δn will increase the focal length of the resulting lenses, which will be investigated further in chapter 6.

Lenses 1, 3 & 4 all repeat their maximum RI UC for the first step outwards as there was not a lower closest matching value. This is likely to have an affect on the way the lens works and requires further investigation. This could be resolved by filling in the gaps in the range of achievable line width values, visible clearly in figure 5.3, particularly around the 0.5 μm to 0.55 μm range for these higher RI values. This would require an extension to the study in chapter 3, either experimentally by creating ascending scan arrays at more speed and power combinations, or by developing a suitable function to predict line widths as discussed in section 3.3.3.

The mean absolute difference between the ideal and selected RI values across all four lenses is 0.002±0.003 where the largest contribution is due to the re-selection of the maximum RI UC, where Lens 1 contributes a 0.012 difference for that first step out from the centre. Outside of this, Lens 4 has the largest selection differences with a mean difference of 0.005±0.003 across the UCs. These differences will alter the profile in the lens, potentially affecting its operation which will be investigated further in chapter 6.

The analytical results for the rectangular cut out approximation are all smaller than those for the cylindrical fishnet structure with a mean difference of $-(0.004\pm0.001)$ (with repeated UCs excluded). This will be due to the approximation breaking down towards the central region of the cylindrical fishnet structure. In this region, the gaps between the rings and spokes are more trapezoid, and thus create a denser structure. This limitation will also be present in the simulation results.

Since MGT does not consider the geometry of the structure, one potential avenue of investigation is deriving an analytical solution for the RI that takes into account the cylindrical fishnet geometry. Zhang and Wu developed an EMT for anisotropic metamaterials consisting of a rectangular array of elliptic cylinders [140]. Their analytical results found good agreement to simulated results for lower aspect and filling ratios, but at higher aspect ratios and filling ratios the results deviated from simulations due to the lack of inclusion of higher order angular momentum terms. While a new EMT would reduce the heavy computational resource requirements, the time and mathematical expertise required to incorporate the complexities of the cylindrical fishnet structure may outweigh the benefits provided.

5.4.2 Simulated RI Discussion

Unit Cells

The simulation results shown in figures 5.5−5.8 show some of the same characteristics when compared to other fishnet structures in the literature. In [141] their Silicon fishnet structure has a large resonance peak at $\sim$ 550 THz where the RI dips below zero after the peak. Similarly in this investigation, the RI is lower after a resonance, but no negative RIs have been reached. One reason for this may be due to the larger RI of Silicon, leading to larger differences at resonance overall. Figures 5.5−5.8 also showed the larger resonance peaks (after 200 THz) shift towards higher frequencies with decreasing UC fill fraction. Gaufillet et al. [142] showed similar results by decreasing the side length of square pillars of TiO_2. Their RI vs frequency plot showed resonance peaks that shift towards higher frequencies for decreasing side length, which is equivalent to decreasing the fill fraction.

The resonances found in this work tend to be wider with larger UC asymmetry, particularly when the major axis is aligned with the direction of wave propagation. Looking at appendix E, figures E.1− E.4 show the geometries of the UCs for each lens. The UCs for Lens 1 (figure E.1), show that UC-E.1a (W 517 S 10) and UC-E.2b (W 523 S 10) are asymmetric, but the major axis is aligned perpendicular to the wave propagation in the x-direction. These two UCs have fewer resonances across the frequency range, where resonances also occur at a higher frequency overall. In contrast, UC-E.1c (W 487 S 5), UC-E.1d (W 374 S 4), and UC-E.1e (W 273 S 2) are all asymmetric with the major axis along the x-axis, parallel to the propagating wave. These three UCs have resonances starting from ∼170 THz repeating more frequently along the spectrum. In particular UC-E.1e no longer has an effective regime at all after ∼190 THz.

This pattern is repeated for Lenses 2 and 4, where the asymmetric UCs with the major axis parallel to the x-direction show more resonance regions starting at lower frequencies compared to the other UCs in those lenses. For Lens 2 the specific UCs are UC-E.2f and UC-E.2g corresponding to W 322 S 5 and W 273 S 2 respectively. For Lens 4 the specific UCs are UC-E.4e and UC-E.4f corresponding to W 548 S 4 and W 548 S 2 respectively. In all cases these are also the UCs with the lowest RI for that lens. Furthermore, Lens 3 has the smoothest group of plots (figure 5.7), and looking at the UCs (figure E.3), all are asymmetric with their major axis in the y-direction. This is likely due to commensurability effects where the waves peak in either the ring of material or in the air gap itself.

An important consideration here, is that in the cylindrical fishnet structure these UCs are oriented around a circular axis, therefore these resonance peaks are likely to be different when the UC is rotated 90° compared to their single orientation in this study. In addition, as mentioned in section 5.4.1, this rectangular cut out approximation is less representative of UCs towards the central region of the cylindrical fishnet structure. Therefore, future work should look to solving the computational resource requirements to allow simulations of the full cylindrical fishnet structure. This includes making use of symmetries in the structure to reduce the overall simulation domain, or increasing hardware specifications.

The resonance peaks indicate which frequencies to avoid for lens operation, however these results are limited by material definition within the COMSOL simulation. A single RI value was used which is not indicative of the RI of the material across the full frequency range. From [135], IP-L is shown to have a decreasing RI between λ = 1 μm to 1.5 μm which should be accounted for in the model. In [143] the complex dielectric function of IP-L was investigated across a spectral range of 1.67 μm to 40 μm, which found a weak absorption feature at around 2.8 μm (107 THz). However, [143] used UV light to cure the polymer rather than TPP and so the material properties may not be equivalent due to the different degree of cure. To improve the simulation results presented in this thesis, a study should be undertaken to obtain the complex optical properties of IP-L across the whole frequency range used in this work, using a method such as spectroscopic ellipsometry as in [135] and [143].

A further consideration is the changing RI with laser dose, as found in [144]. As Lenses 1−3 make use of dose changes to alter the line widths, the material properties will have slight differences between each RI region. One difficulty with directly measuring the optical properties of a TPP material is that proximity affects [119] mean the slicing and hatching parameters will also have an affect on material properties. This means the creation of a bulk structure large enough to measure with ellipsometry will already have different optical properties compared to a single line of resin. Implementing the UV curing step for development from [130] discussed in chapter 4 may help to reduce any differences across dose region by creating a more uniform degree of cure across the structure.

The RI differences across the designed lenses are shown in table 5.2, showing the expected decrease from Lens 1 to Lens 4. These results are smaller than expected based on the analytical results (table 5.1), yet they are still larger than achievable with traditional GRIN optics [4]. The base material will have a large contribution to what is achievable in terms of Δn, therefore implementing a multimaterial TPP process, as discussed in chapter 2, with a second higher RI material will enable larger RI contrasts. Another method may be to include Germainium in the resin, which has a high RI (n = 4.0449 at λ = 2 μm [145]) and is transparent in the infrared region. Malinauskas et al. [146] created a hybrid germanium silicate material which was printed successfully using TPP. Yet, while the material is transparent in the 400 nm$-$1600 nm spectral region, the material was found to have an RI of only 1.581 at $\lambda = 632$ nm which will be smaller still in the RI region investigated in this work. This offers little benefit over other commercially available resins offered by Nanoscribe, namely IP-n162 with an RI of 1.6016 at $\lambda = 1000$ nm [147].

Figure 5.9 shows the simulated results with respect to the designed lens profile, in addition to the two sets of analytical results. Lens 3 is the closest to the expected profile with little deviation from the ideal, with the analytical calculations predicting the UC RI well. This is likely related to the orientation of the major axis with respect to the EM radiation as previously discussed, and results may be different if the simulations were to be run with a 90 degree rotation (discussed further in section 5.4.2). The other three lenses show larger deviations from the ideal profile, where UCs at the outer edge (lower RI) are further from the ideal profile compared to UCs at the centre of the lenses. This is further demonstrated in figure 5.10, where the lower fill fraction UCs are generally further away from the trend line. Once again these effects may be different with rotation of the UCs, or by simulating the full cylindrical fishnet structure. Additionally, the rectangular cut out analytical results did not predict the simulated results better than the cylindrical fishnet analytical results, despite being accurate to the actual fill fraction of the simulation geometry.

Based on the limitations above and the discussion in appendix C, it is difficult to say for sure the results presented in this section are representative of how the structure will behave. Therefore, experimentally measuring the metamaterial will help to validate the results if both show similar characteristics across the frequency range. Experimental measurements can be undertaken with ellipsometry, which would require the fabrication of a large area fishnet structure. The cylindrical fishnet itself can also be measured in this way which would help eliminate the need for the computationally heavy simulations for that structure.

Finally, there are experimental uncertainties to account for due to line width uncertainties during fabrication. These uncertainties will alter the fill fraction and thus change the resulting RI. These differences can be nominally accounted for by running simulations at plus and minus the standard deviation of the experimental line widths. However doing this for every UC would be time resource heavy and it may be more prudent to investigate select UCs.

Unit Cell Rotation

The UC with the largest asymmetry (W 273 S 2) produced the largest RI difference when rotated through 90°, while the most symmetric UC (W 501 S 7) produced the smallest RI difference. Figures 5.12 to 5.14 show the electric field for slices through the structure in all three axes for the two different rotation angles. In all cases there is evidence of modal resonances, shown by the bunching of the wave across the simulation region. Similar modal patterns can be seen in figure 1 in [148] where the electric-field components of the first 6 spatial modes for their rectangular core waveguide are presented.

In figure 5.12 for UC W 273 S 2 the wave is strongly confined in the air gap for the ϕ = 90° rotation, potentially explaining the lower RI at this angle due to the stronger interaction in the lower RI material. Similarly in figure 5.13 for UC W 548 S 10 the wave is tightly confined in the air gap for the ϕ = 0° rotation, once again potentially leading to the lower RI. However, there are no clear differences in the field pattern between the rotation angles for UC W 501 S 7 shown in figure 5.14 which is consistent with there being only a small change in the RI between the two angles. The modal pattern swaps between x and y slices for the different angles, however the wave is not tightly confined to one particular material. The size of the air region for this UC is 0.406 μm $\times$ 0.499 μm giving length scales of $< \lambda/4$. These results for UC W 501 S 7 suggest the metamaterial is truly working in the effective regime for both polarisations.

It should be noted that the RI values for ϕ = 0° are lower than those calculated for these UCs in the full UC study in table 5.2. This is likely due to the results of the full study relying on the prior value for calculation (using equation 5.9b). Overall, these results show a strong polarisation dependence particularly for more asymmetrical unit cells. This is likely to affect the way the cylindrical fishnet structure operates further requiring the need for an experimental investigation.

5.5 Summary

- The analytical results predicted a large RI difference of Δn = 0.340 for a lens with a solid material centre and decreasing the number of spokes/line width radially outwards.
- Four lenses were designed based on a normalised sech curve and 7 unit cells were selected for each lens to take forward to simulate in COMSOL. This narrowed down the 837 line width and spokes combinations to a more reasonable 22 unique UC combinations for simulation.

- The simulated UC results showed the expected decrease in RI with decreasing fill fraction, and the more asymmetrical UCs produced larger resonances when their major axis was aligned with the direction of wave propagation.
- The simulations found a maximum RI difference of Δn = 0.296, 0.044 lower than predicted analytically. However, the more asymmetric UCs are strongly polarization dependent with the lowest fill fraction UC (W 273 S 2) reducing from n = 1.195 to n = 1.145 with a 90° rotation.
- An experimental investigation into the complex RI of the resin should be sought to improve the reliability of the simulated results. Additionally, experimentally investigating the cylindrical fishnet structure would allow an understanding of how the orientation of the UCs affect the resulting RI based on the strong polarisation dependence.

This chapter has provided a list of achievable RI values for different unit cells by undertaking frequency domain simulations across the 100 THz to 300 THz range. The results have shown that there is an effective region between 1 THz $-$ 1.5 THz where after this there are frequent resonances for all unit cells. These results are used in the next chapter where the RI values will be used to simulate the propagation of light within the the designed lenses in order to find the focal length.

Chapter 6

Lens Investigation and Fabrication

6.1 Introduction to Lens Investigation and Fabrication

Using the results from the previous three chapters, simulations of the four lenses are undertaken in addition to fabricating proof of concept lenses. The focal length and spot size of each lens is investigated through 2D COMSOL simulations using the ideal, simulated and stepped RI profiles from the preceding chapter. These focal lengths dictate the length-/height of the fabricated structure needed to bring light to a focus and are the figure of merit (FoM) for this work. Proof of concept lenses are printed for each of the four lenses using the fabrication parameters dictated by the selected line widths. The outcome of this chapter is an understanding of what is currently achievable for a TPP metamaterial lens as well as what still needs to be done to improve the fabrication of such a cylindrical fishnet lens.

6.2 Lens Design Methodology

6.2.1 Focal Length Calculations & Simulations

Using the sech RI profile from equation 2.2, the RI distribution constant α can be defined as,

$$\alpha = \frac{1}{\mathrm{r}_0} \cosh^{-1}\left(\frac{\mathrm{n}_0}{\mathrm{n}_{\mathrm{r}_0}}\right), \tag{6.1}$$

where n_0 is the central (maximum) RI, $\mathrm{n}_{\mathrm{r}_0}$ is the outer (minimum) RI and r_0 is the radius of the lens. For a self-focusing lens, the focal length is defined as the quarter-pitch of the sinusoidal wave within the medium [13] so that,

$$F = 2\pi/4\alpha. \tag{6.2}$$

The pitch is defined as the length it takes a ray to complete one sinusoidal period while travelling in the lens. Using equations 6.1 & 6.2, the analytical focal length for each of the four lenses was calculated based on the the ideal and simulated maximum and minimum refractive index values as discovered in chapter 5. This provided the height of fabrication needed in order to produce a lens with a back-plane focus.

COMSOL simulations were undertaken to investigate the resulting focal length further. The model was based on the "Defining a Mapped Dielectric Distribution of a Material" file provided by COMSOL [149]. Figure 6.1 shows the domains and boundary conditions used within the model. This is a 2D model consisting of a rectangular region defining the metamaterial lens (blue gradient) surrounded by a rectangular air domain (white) bounded by a PML (orange stripes) on all sides. A Gaussian beam is modelled entering from the left side using a surface current excitation at the interior boundary (black

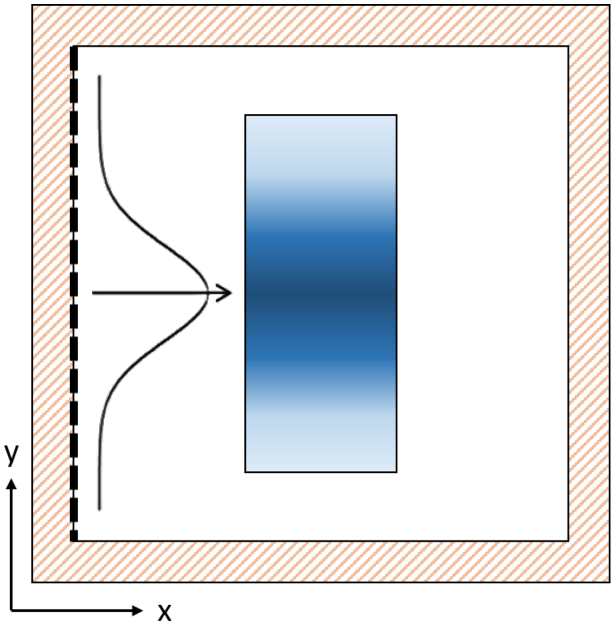

Figure 6.1: Schematic showing the COMSOL model domain. It consists of the metamaterial lens (blue gradient) in an air domain, surrounded by a PML (orange stripes), with a Gaussian beam incident from the left inside boundary (black dashed).

dashed line) which is defined as,

$$\mathbf{J}_{s0} = \exp\left(-\left(\frac{y}{w_0}\right)^2\right) \tag{6.3}$$

where the beam waist at the boundary is w_0 = 20 μm to ensure good coverage of the lens. The excitation creates a wave propagating in both directions along the x-axis, so that the PML perfectly absorbs the wave in the negative x-direction, and the lens diffracts the wave moving in the positive x-direction. The RI distribution is defined along the y-axis modifying equation 2.2 to a 2D distribution such that,

$$n(y) = \mathrm{n}_0 \operatorname{sech}\left(\frac{\pi y}{2F}\right), \tag{6.4}$$

which is then used as the user defined RI for the Wave Equation domain for the lens. The model solves for the out-of-plane electric field and results in a plot of the electric field norm which is focused within the lens structure. This model does not use the deformed geometry defined in the example file [149].

The model is run for an r_0 = 35 μm radius lens at f = 150 THz (λ = 2 μm). The length of the lens is changed according to the focal length results for the corresponding radius in table 6.1. Three different RI profiles are run for each lens; the ideal profile based on the analytical cylindrical fishnet RI results, and a stepped and smoothed RI profile based on the simulation results. For the ideal and smooth curves, equation 6.4 is used to create a continuous curve based on the maximum and minimum RI values. A piecewise function is used to define the stepped RI based on the simulated unit cell results.

For the smooth and stepped simulated RI profiles, the x-coordinate of the maximum intensity value in the data set is found, which corresponds to the focal length. The intensity values in y at this x-coordinate are plotted against their corresponding y-coordinates. For the smoothed profile results, a Gaussian fit is applied to the data and from this the $1/e^2$ focal width is found.

6.2.2 Fabrication of Lenses

Four GRIN lens structures are produced based on the selected unit cells from section 5.3.1. Each structure consists of 7 regions within which the necessary line width and number of spokes is produced, figure 6.2 is a schematic for visualisation, annotated to show the region boundaries. Each region is 5 μm in width and consists of 5 sets of rings and spokes, so that the overall structure is 35 μm in radius. The layer spacing is 0.7 μm. Two sets of the four lenses are produced; one set with 5 layers, and the second with the number of layers equal to the focal length of the ideal analytical results (1 layer per micrometer). All structures are printed on a silanized glass slide using the procedure outlined in section 4.2.1.

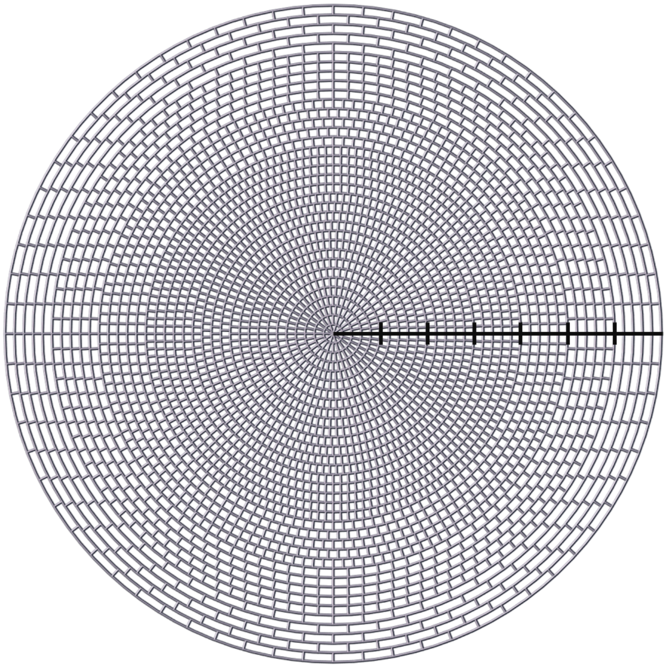

Figure 6.2: A rendering of a GRIN cylindrical fishnet structure where the density of spokes is changed for each of the 7 discrete regions. In this example a region is 5 μm corresponding to 5 ring/spoke pairs per region where the boundaries have been annotated with black lines for visualisation.

6.3 Results

6.3.1 Focal Length and Spot Size

Table 6.1 shows the analytical focal length results for each lens based on two sets of RI values. The analytical results use the cylindrical fishnet max and min RI for two different lens radii, and the simulated results show the focal length for one lens radius. The r_0 = 100 μm radius is based on the maximum printable area before stitching (as per chapter 4) whereas the r_0 = 35 μm radius was based on the chosen radius for the printed lenses. A smaller Δn results in a larger focal length.

Figures 6.3−6.6 show colour maps of the electric field intensity within the simulation boundary, with the colour bars normalised to 840 Vm^{-1} across all plots. For the continuous RI profiles, a clear focal spot is produced, however this is not the case for the stepped RI profiles.

Figure 6.7 shows the electric field intensity at the simulated focal position for the smooth RI profile based on simulated unit cell results, and figure 6.8 shows the same but for the stepped RI profile. The stepped profile produces a less defined focal spot compared to the smooth profile. Table 6.2 provides the simulated focal lengths for the smooth and stepped profiles, and the $1/e^2$ focal spot width for the smooth simulated profile for each lens.

Table 6.1: Analytical focal length results for the maximum (n_0) and minimum (n_r) refractive indices for each lens. RI ideal is the maximum and minimum analytical RI results, and RI simulated are the simulated results at 150 THz.

Lens	**RI Ideal**				**RI Simulated**		
	n_0	**n_r**	**f/μm** **r = 100 μm**	**f/μm** **r = 35 μm**	**n_0**	**n_r**	**f/μm** **r = 35 μm**
1	1.492	1.152	209.2	73.2	1.492	1.196	79.7
2	1.461	1.152	218.9	76.6	1.453	1.196	85.3
3	1.461	1.274	293.3	102.7	1.453	1.277	105.9
4	1.461	1.293	310.6	108.7	1.453	1.345	138.1

Table 6.2: Comparison of analytical (RI simulated) focal lengths (table 6.1), to the simulated focal lengths for the smooth and stepped profiles. The $1/e^2$ spot size is included for the smooth curve.

		Smooth Profile			**Stepped Profile**	
Lens	**Analytical Focal Length (μm)**	**Focal Length (μm)**	**ΔF (μm)**	**$1/e^2$ Width (μm)**	**Focal Length (μm)**	**ΔF (μm)**
1	79.7	79.9	0.2	3.113±0.009	95.7	16.0
2	85.3	85.5	0.2	3.395±0.018	83.9	−1.4
3	105.9	106.10	0.2	4.235±0.002	104.5	−1.4
4	138.1	138.7	0.6	5.468±0.028	125.0	−13.1

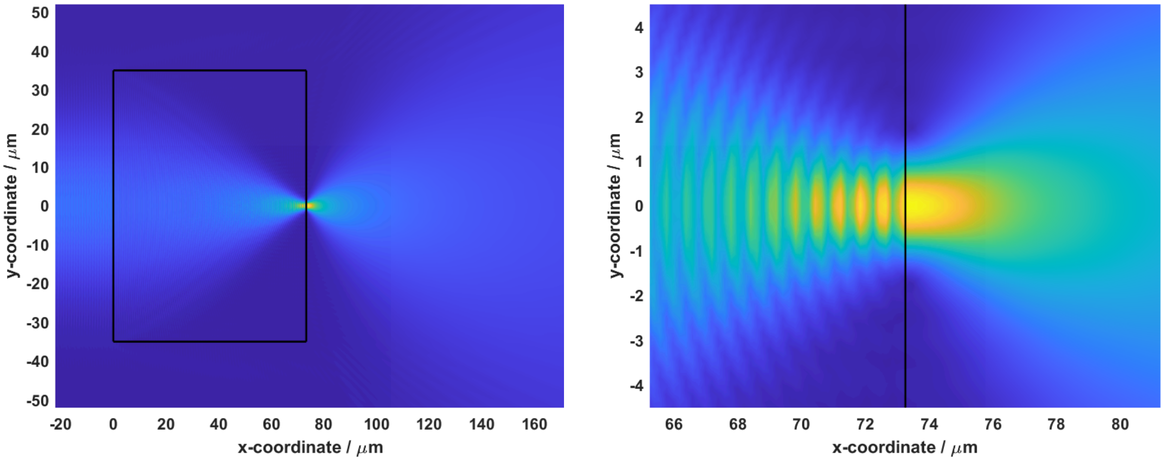

(a) Ideal RI Profile (b) Ideal RI Profile at Focal Position

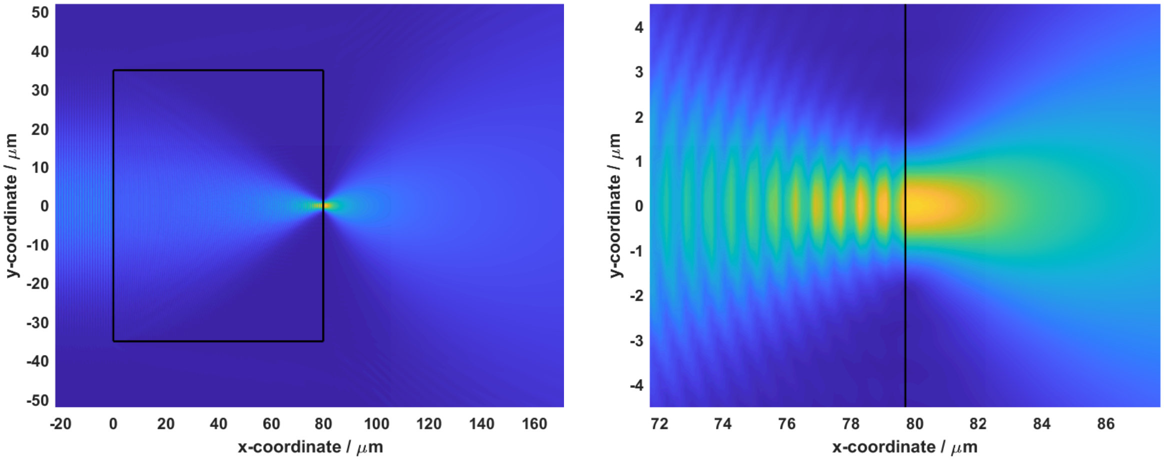

(c) Smoothed RI Profile (d) Smoothed RI Profile at Focal Position

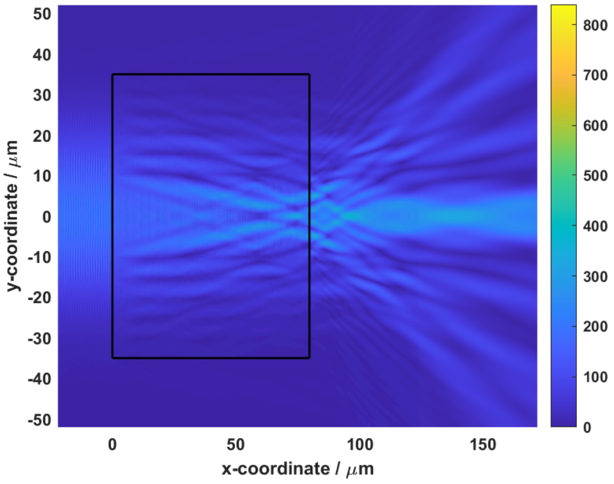

(e) Stepped RI Profile

Figure 6.3: Lens 1 simulations.

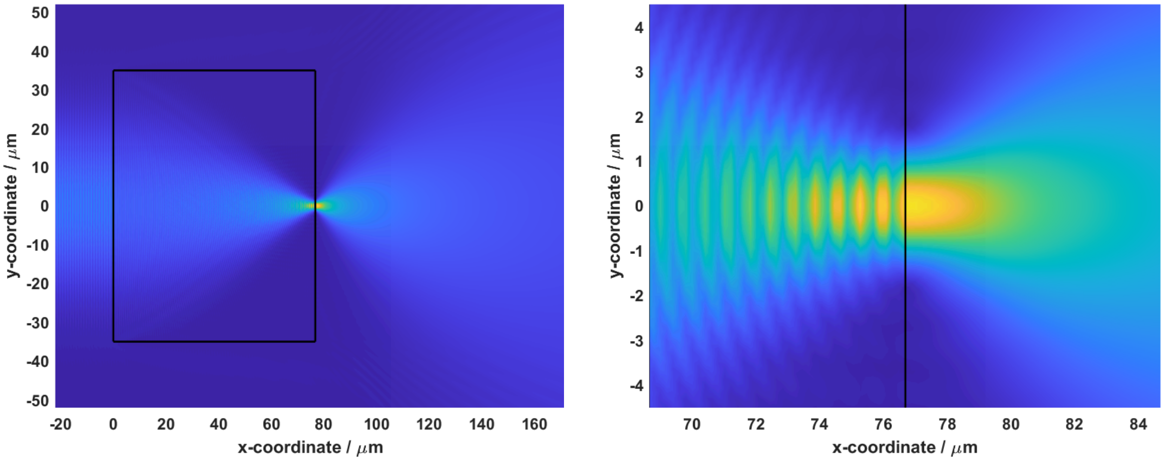

(a) Ideal RI Profile (b) Ideal RI Profile at Focal Position

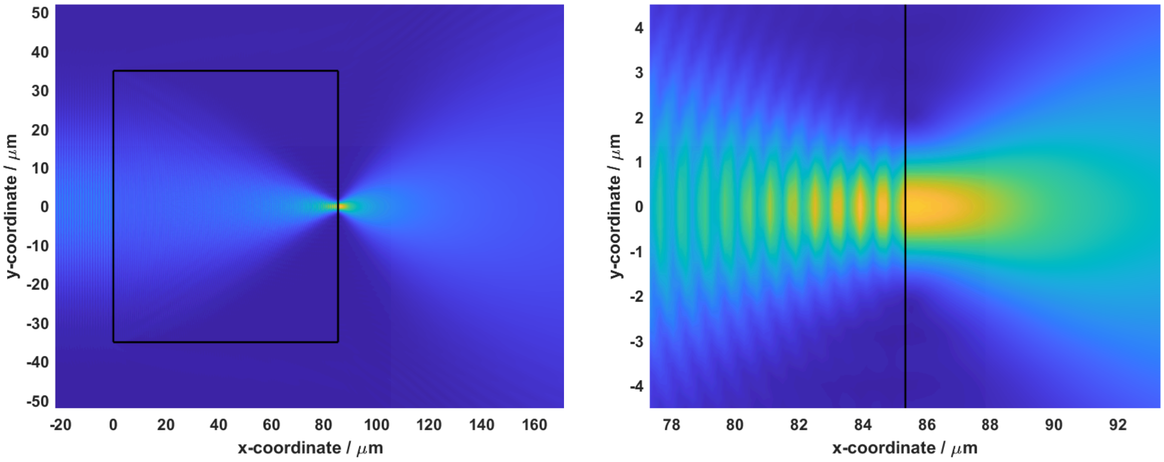

(c) Smoothed RI Profile (d) Smoothed RI Profile at Focal Position

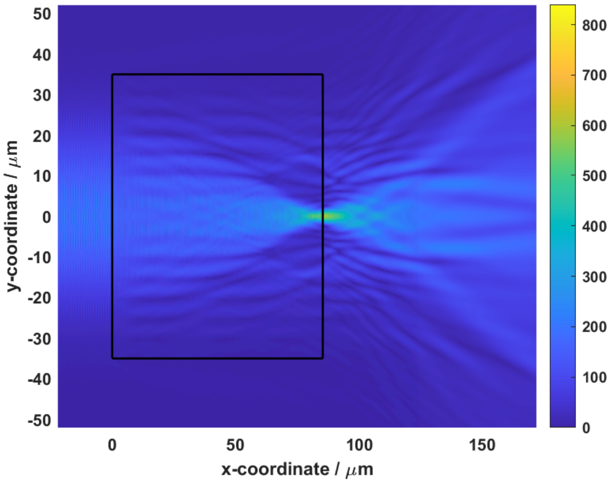

(e) Stepped RI Profile

Figure 6.4: Lens 2 simulations.

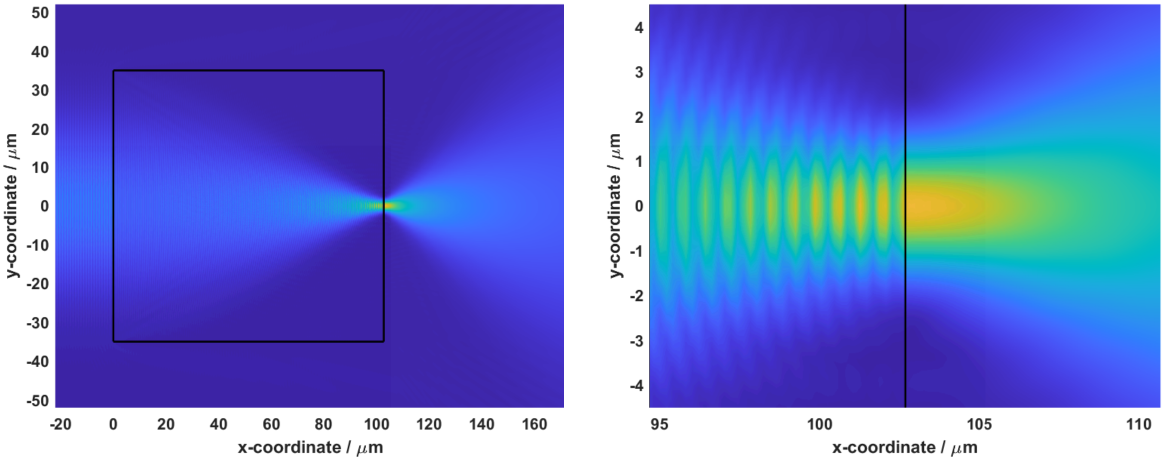

(a) Ideal RI Profile (b) Ideal RI Profile at Focal Position

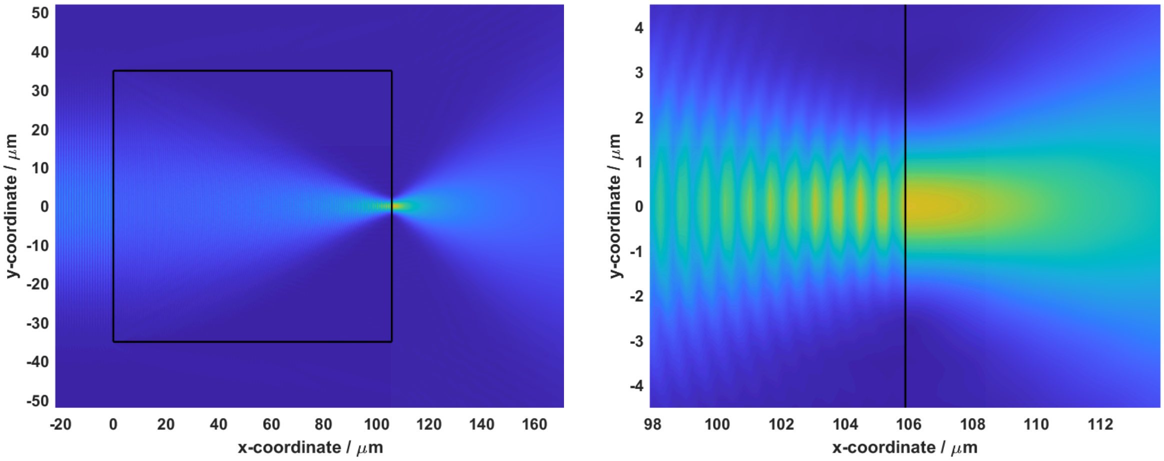

(c) Smoothed RI Profile (d) Smoothed RI Profile at Focal Position

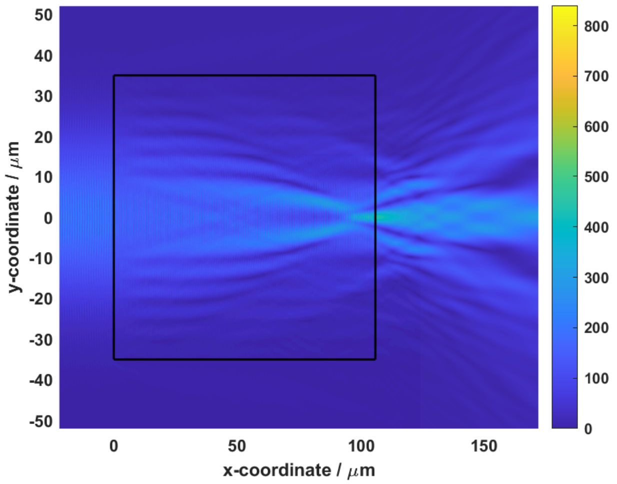

(e) Stepped RI Profile

Figure 6.5: Lens 3 simulations.

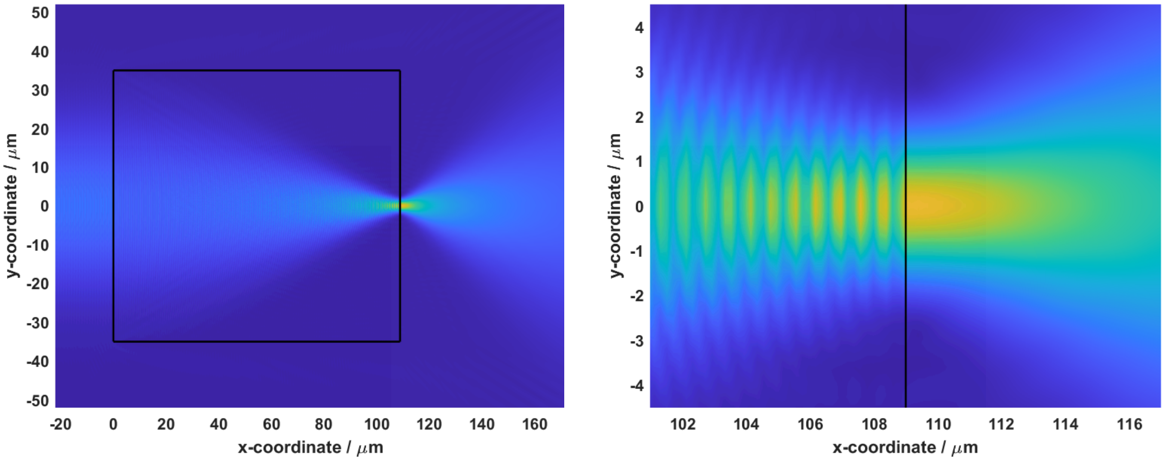

(a) Ideal RI Profile (b) Ideal RI Profile at Focal Position

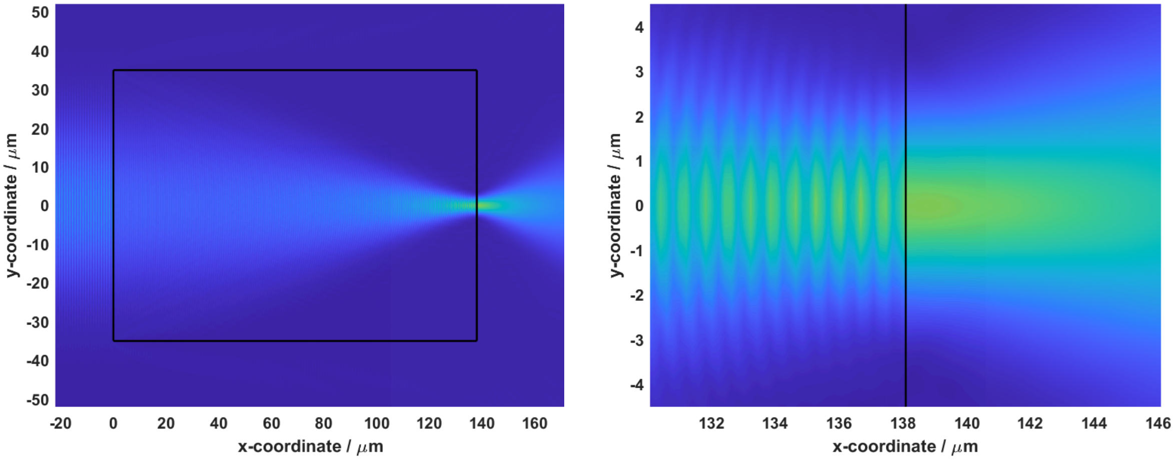

(c) Smoothed RI Profile (d) Smoothed RI Profile at Focal Position

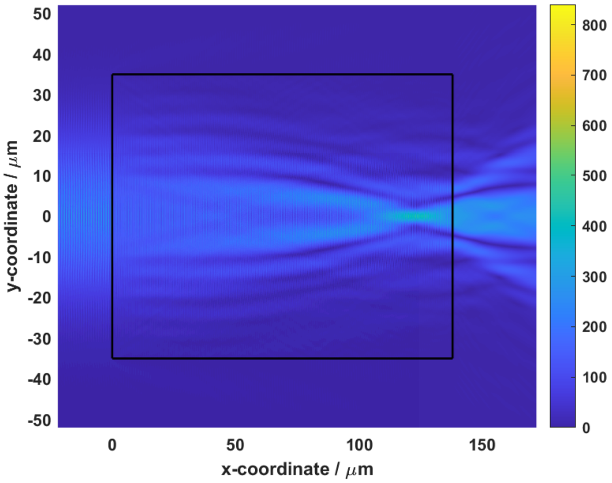

(e) Stepped RI Profile

Figure 6.6: Lens 4 simulations.

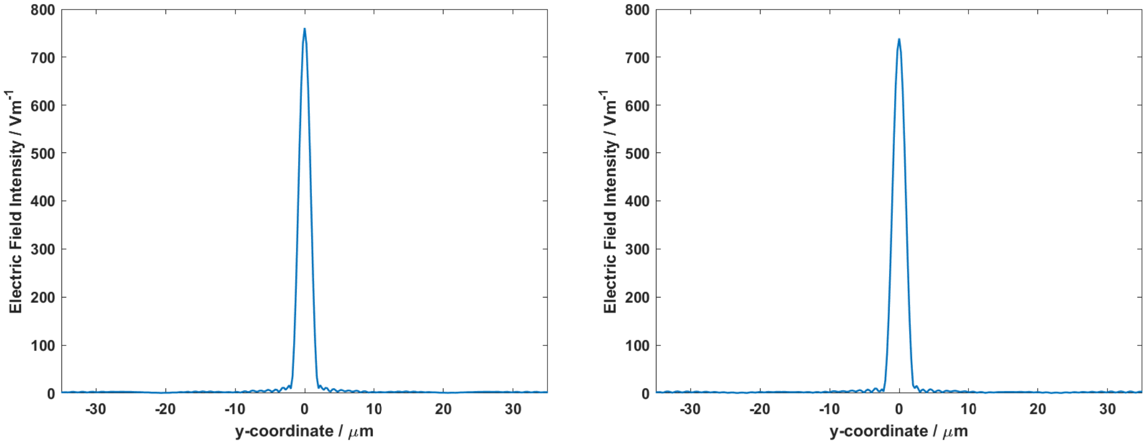

(a) Lens 1

(b) Lens 2

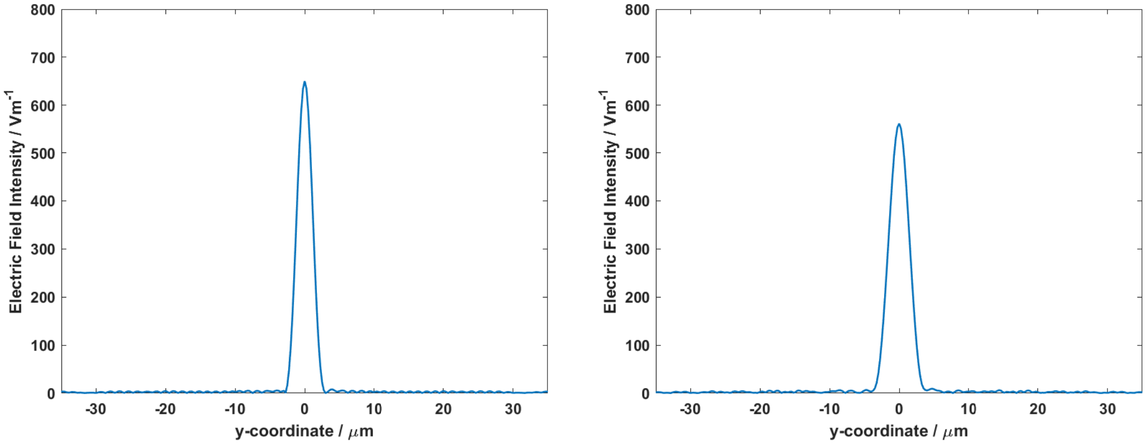

(c) Lens 3

(d) Lens 4

Figure 6.7: (a) – (d) Electric field intensity across the focal position for the smoothed simulated profile.

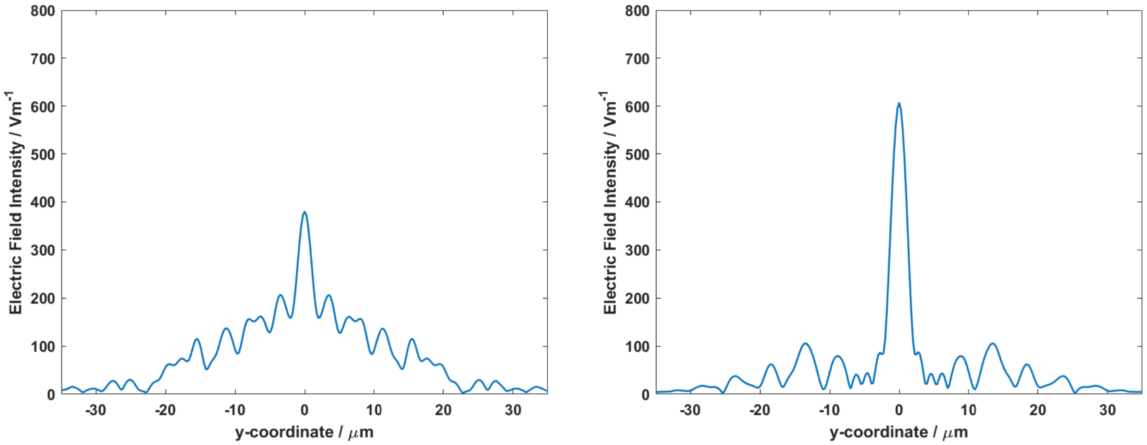

(a) Lens 1

(b) Lens 2

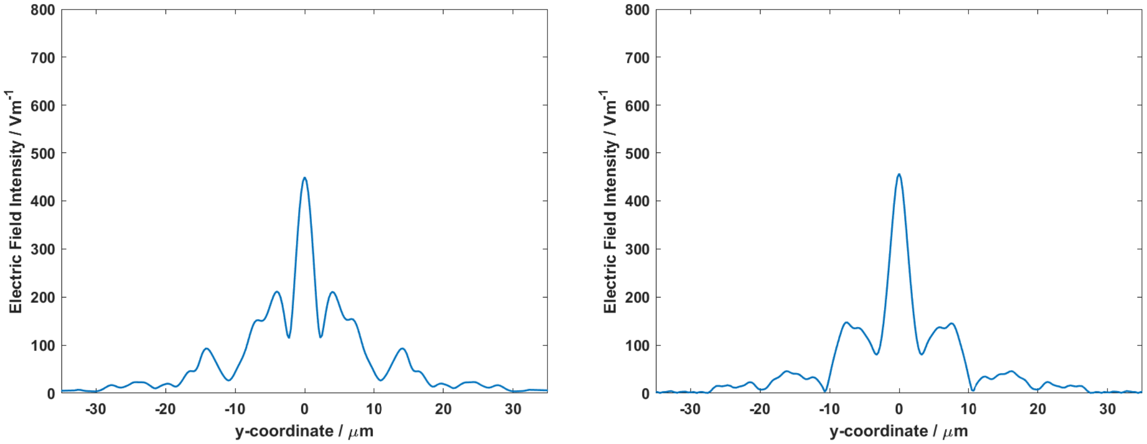

(c) Lens 3

(d) Lens 4

Figure 6.8: (a) – (d) Electric field intensity across the focal position for the stepped simulated profile.

6.3.2 Fabricated Lenses

Table 6.3 shows the fabrication parameters used for each of the RI regions in the designed lenses in addition to their corresponding ideal (discretised sech curve) and simulated RI values for reference.

Table 6.3: Fabrication parameters for the unit cells in each of the designed lenses.

Lens	RI Ideal	RI Simulated (@150THz)	Starting Spokes	Line Width (nm)	Scan Speed (µm s^{-1})	Laser Power (%)
1	1.492	1.492	Solid Block		10 000	50
	1.480	1.492	Solid Block		10 000	50
	1.447	1.438	10	517	50	25
	1.393	1.388	10	427	1000	30
	1.323	1.354	5	487	2000	50
	1.241	1.283	4	374	100 000	120
	1.152	1.196	2	273	50	10
2	1.461	1.453	10	548	100	30
	1.451	1.441	10	523	20	25
	1.421	1.416	10	474	500	35
	1.372	1.385	7	501	1000	45
	1.309	1.327	7	392	5000	45
	1.234	1.267	5	332	100 000	105
	1.152	1.196	2	273	50	10
3	1.461	1.453	10	548	100	30
	1.456	1.453		548	100	30
	1.438	1.432		504	200	30
	1.411	1.407		458	2000	45
	1.373	1.371		399	50 000	115
	1.327	1.329		339	50 000	80
	1.274	1.277		273	50	10
4	1.461	1.453	10	548	100	30
	1.456	1.453	10			
	1.441	1.435	9			
	1.416	1.419	8			
	1.382	1.393	6			
	1.341	1.372	4			
	1.293	1.345	2			

Figure 6.9 shows SEM images of the four lenses fabricated with 5 layers. In (a) to (c) some of the same issues discussed in chapter 4 are present, with regards to ring separation. In addition, the thinner and wider spaced regions at the edge of lenses 1 and 2 show collapsing of the rings. Lens 4 however, only shows slight shrinkage in the outer most ring and is otherwise the as designed structure.

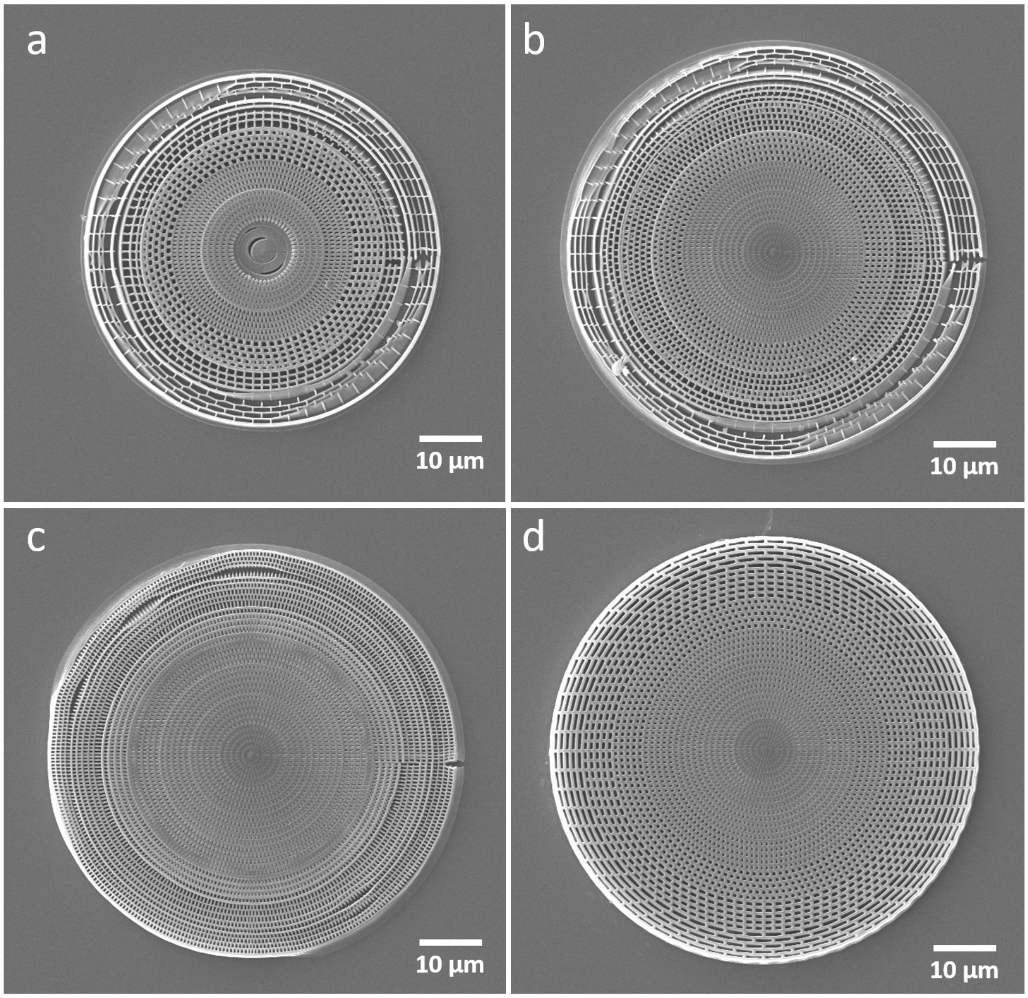

Figure 6.9: (a) to (d) show 5-layer printed structures of Lenses 1 to 4 respectively.

Figure 6.10 shows the four lenses printed with the number of layers equal to their focal length. A frame was used with a view to aiding structural stability as verticality was added. However, all structures have failed to print successfully. This was expected for lenses 1 to 3 given the issues with the 5-layer structures, but while it has faired better, lens 4 is still no longer usable at this height.

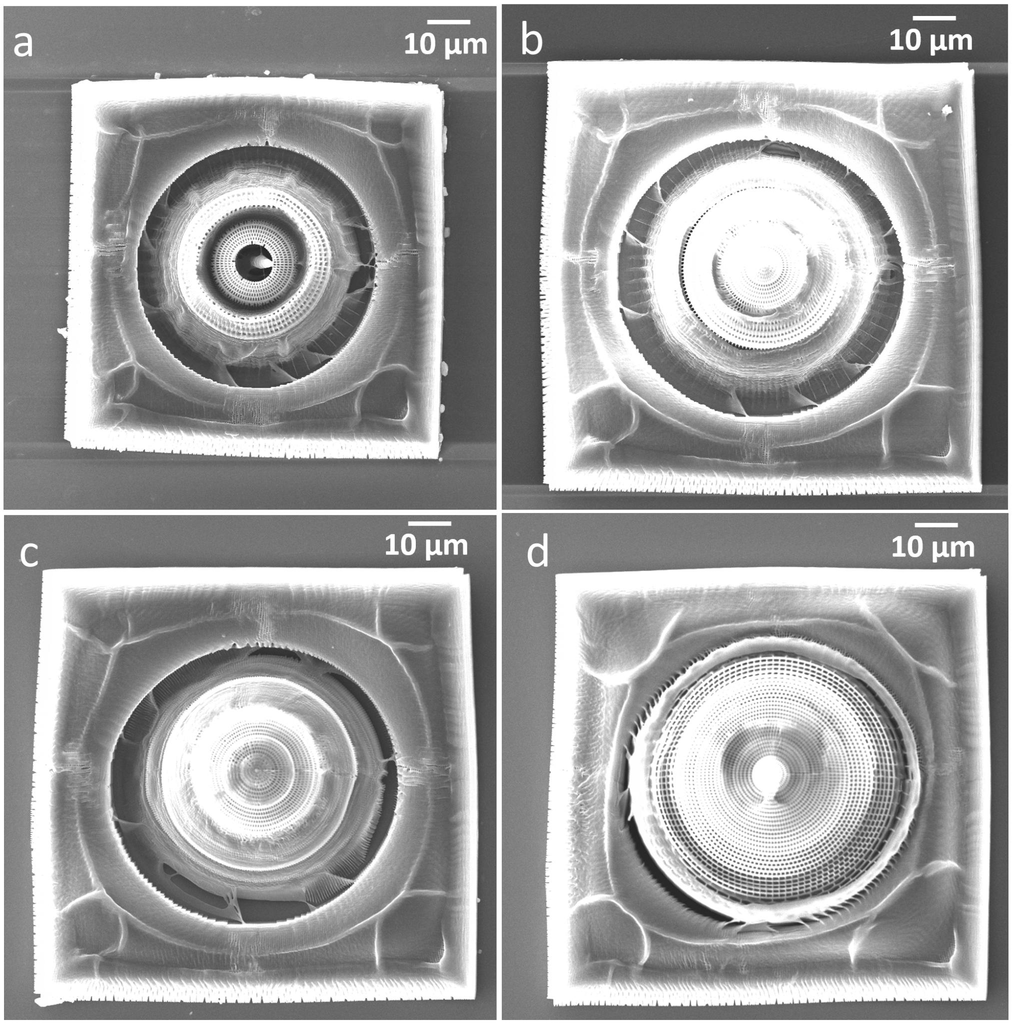

Figure 6.10: (a) to (d) show framed printed structures of Lenses 1 to 4 respectively with the number of layers equal to their respective focal lengths.

6.4 Discussion

6.4.1 Focal Length and Spot Size

Figures 6.3−6.6 show the electric field intensity throughout the simulation domain for Lenses 1 to 4. A magnified image of the focal spot is shown for the continuous curves ((b) and (d) in each figure), and from these it is clear that the intensity decreases from Lens 1 to Lens 4 as the shade shifts from yellow to green. This is shown again in figure 6.7 as the height of the Gaussian focal spot profile decreases from Lens 1 to Lens 4, while also broadening at the base. The reduction in power for each lens profile is likely due to the longer propagation lengths leading to more losses along the length of the structure.

The electric field intensity of the stepped profiles are shown in (e) of figures 6.3−6.6. These colour maps show that the light is not brought to a clean focus, with diffraction evident throughout the structure, likely due to the large index steps between the boundaries refracting the waves. Figure 6.8 shows the intensity distribution at the "focal length" of these lenses once again demonstrating this diffraction. Comparing these to the focal length profiles in figure 6.7, suggests that the RI profile needs to be smoother for optimum functioning of the lens, and so more discrete regions should be added to have smaller RI steps across the structure.

The analytical focal lengths in table 6.1 show numerically that the focal length will increase with increasing lens radius, or decreasing Δn. Table 6.2 shows that for the smooth profile the focal length is larger than the analytical values. Lenses 1 to 3 have the same difference in focal length (ΔF) of 0.2 μm while Lens 4 is 0.6 μm larger. The difference here may be due to how close the longest lens is to the boundary of the system, and any unintended reflections at the PML may affect the result more than the other lenses. Creating a larger air domain around all of the structures should avoid any unwanted reflections at the edges.

The focal lengths of the stepped profiles are very different from predicted, with Lens 1 being 16 μm larger than expected, while Lenses 2 to 4 have focal positions inside the lens itself. Although these are the positions of the maximum intensity of the beam, it may be inappropriate to treat them as true focal lengths for comparison.

A difference between analytical and simulated focal lengths is expected due to the simulation taking into account the physical effects in the system, such as reflections, scattering and using a Gaussian beam that interacts with the system rather than isolated rays. In addition, the wavelength of the light will affect the pitch of the lens as that will determine how long (in space) it will take to complete one sinusoidal period.

Shrestha et al. present their work on dielectric metasurface lenses made from silicon by EBL which operate in the 1.2 μm to 1.65 μm wavelength range [150]. Their "M1A" lens has a diameter of 100 μm and an experimentally measured focal length of 200 μm which is larger than the focal lengths found in this work. However, their "M3" lens also with a diameter of 100 μm has a focal length of 30 μm which is considerably below what can be attained by the GRIN metamaterial lens designed in this work. This suggests that a metasurface approach may be more attractive for applications where the shortest possible focal length is required.

The broadening of the Gaussian intensity plots shown in figure 6.7 is reflected in the $1/e^2$ focal spot size in table 6.2. Lens 1 provides the minimum beam width at 3.113 μm ± 0.009 μm which corresponds to 1.56λ. This is similar to the results obtained in [151] for their metamaterial GRIN lens working at 1.3 THz. This quantity is important for coupling into optical fibres, as careful mode matching between the focused beam and the fibre core is needed to ensure maximum power transfer [152].

These results are a good guide for what is expected based on the RI gradients of the designed lenses in terms of both an ideal continuous curve and the real world stepped profile. However, a major limitation is that the simulation did not simulate the cylindrical fishnet metamaterial itself which, as discussed in the previous chapter, is likely to have different responses to the wave at different positions. Therefore, creating a 3D simulation of the structure will provide more accurate results overall. Additionally, the meshing of the simulation domain will likely generate sources of error. An extra-fine physics controlled mesh was used here, where COMSOL automatically calculates a mesh based on the wavelengths involved in the simulation. A finer mesh may be created using a user-defined mesh, which will increase the simulations times but allow a more accurate result.

Although simulations are a useful guide, they do not take into account real world inefficiencies, or fabrication defects. Therefore, an experimental investigation should be undertaken to understand the actual focal length of these lenses using a method and optical set up such as the one outlined in [82]. However, there are a number of fabrication considerations to overcome first which will be discussed in the next section.

6.4.2 GRIN Fabrication

The 5-layer printed structures for Lenses 1 to 3 had structural deformities as shown in figure 6.9. For Lens 1, the gaps in the solid centre are likely due to the way the region was fabricated. This central region was produced by scanning rings with a radius increase of 0.35 μm between each ring, at SS = 10 000 μm s^{-1} & LP = 25 mW. The gaps are likely due to suboptimum spacing between the rings leading to a lack of adhesion. As a note, the central region should be twice as large based on the analytical results as the solid region was the closest match for the next step out also, this is a user programming error. The next three discrete regions of Lens 1 are well made but there are clear height differences between each section due to the differences in the laser dose between the regions (see table 6.3).

The outer regions seem to have suffered from misalignment issues, where rings are not evenly spaced, and there are overlaps between sections. The outermost RI region has collapsing ring walls, likely due to a lack of structural stability with how thin the line widths are in that region. Lens 2 shows a similar issues, where the structure is deformed in the outer two RI regions, especially at the interface between sections. This is likely due to the large structural gradient between these two areas and may be resolved by having more discrete regions to alleviate the stresses across the structure. However, to preserve the focal length, the size of the regions should be smaller to ensure the RI gradient is not reduced overall. This need for a smoother geometrical gradient goes well with the need for a smoother RI gradient, as discussed in the previous section.

Lens 3 has ring separation issues in the outer regions, but generally the structure is better that the previous two. Once again the height disparities in each region due to dose differences is clear. In addition, there are misalignment issues and a lack of adhesion along the joining seam of the rings. Rings are fabricated anticlockwise starting from the 3-o'clock position on the structure, which explains the gaps in the rings along that section. Adding in more of an overlap may help reduce the visible seem in this region.

Lens 4 is well fabricated, with good interfacing throughout and no height mismatches between the regions. This will be due to being fabricated at one laser dose, thus reducing any stresses between RI regions. However, based on the previous results, this lens will produce the smallest RI gradient, and thus need the longest focal length to bring light to a focus. In addition, the results suggest less focal power at the focal position also. Therefore, priority should be given to resolving the fabrication issues for the previous three lenses in order to utilise the larger achievable RI gradients.

The issues with the fabricated lenses are amplified for the tall lenses shown in figure 6.10. Height mismatches within a single layer, warping, peeling and collapsing issues will all be magnified as more layers are added. Therefore, failed prints were expected for Lens 1 to 3, but since lens 4 had no issues at shorter heights, this indicates other issues may be at play. In the oil-immersion configuration, the structure height is limited to

$<$190 μm due to the working distance of the objective, yet all these structures are below this height.

In Rovira et al. [153] they suggested that aberrations increase with height, especially when focusing through a thick layer of cross linked photoresist. The almost conical shape of the lenses shown in figure 6.10 is similar to that shown figure 6(c) in Rovira's work. Their suggestion is to use dip-in (DiLL) mode instead where the objective is lowered into the resin itself and the structure printed downwards, similar to a conventional vat photopolymerisation process. In this mode, structures can be printed with a height $>$300 μm. This requires the use of a more viscous resin, for which many exist in Nanoscribe's catalogue, however this presents more challenges for developing small features. While the transition from oil-immersion to DiLL was a natural progression in order to fabricate larger area lenses that have larger focal lengths, changing resin will require the dose region and line width study conducted in chapter 3 to be repeated for the new resin.

Further work should look at the boundary where the number of layers starts to degrade the structure. The alignment of each layer will play a big part in structural stability during the print. While TPP is generally a self-supporting process, the use of a more viscous resin for DiLL mode may help reduce some of the walls collapsing during fabrication.

6.5 Summary

- Focal lengths depend on the RI gradient of the lenses, where a larger radius with the same RI difference will produce a longer focal length.
- Analytical and simulated focal lengths are similar for the smoothed profile with at most a 0.6 μm difference between the two values.
- The stepped RI gradient with 7 discrete regions does not produce a well defined

focus for any of the four lenses, with diffraction evident throughout the structure.

- The focal spot sizes for the smoothed profile range from 1.6λ to 2.7λ.
- Lenses 1 to 3 showed structural issues when fabricated with only 5 layers, while Lens 4 was as designed with only minor shrinkage on the outermost ring.
- All of the tall lenses were failed prints. While structures under 190 μm tall should be possible to print, the increase in aberrations as the laser focused through the cured polymer may be too much for such a structure.

This chapter has demonstrated how the size of the refractive index gradient affects the resulting focal length of a GRIN metamaterial lens. The gradient should be as smooth as possible across the structure to reduce unwanted reflections at each RI boundary. Implementing a smoother RI profile by adding more discrete regions may also reduce fabrication errors as there will be fewer stresses in the structure at each interface. The main outcome of this chapter has been to show the successful fabrication of a 5-layer GRIN metamaterial structure (lens 4) with simulations to show it could achieve a focal length of 125 μm if fabrication difficulties are overcome to print a structure of this height.

Chapter 7

Conclusions and Future Work

This thesis has presented experimental work undertaken to investigate the use of two-photon polymerisation for fabricating metamaterial lenses. The first two results chapters presented the work undertaken to assess the commercial TPP system used. The final two results chapters were concerned with the metamaterial design and final proof of concept lenses. This chapter will summarise the results obtained in each chapter and present the future direction and potential applications for this work.

7.1 Summary

In chapter 3 the achievable feature sizes of a commercially available resin was investigated. This involved performing a dose test, by changing the laser power and scan speed, to find the workable range of the resin. Woodpile structures were printed and assessed for whether they were under-polymerised, over-exposed, or just right. Using faster scan speeds and lower powers results in under-polymerised structures, whereas slower scan speeds and higher powers result in over-exposed structures, a region between these produces well polymerised structures. By altering the laser dose, one can control the resulting line width of the features in the print. As expected the results showed that lower laser doses produces smaller line widths, and higher laser doses produced larger widths. Work in this chapter also looked at the theoretical fitting function for line width vs laser power as discussed frequently in the literature. This work found that the theoretical fit overestimates the line width for lower powers while underestimating for higher powers. Overall this chapter found that altering the laser dose could provide a large range of line widths as a means to creating gradient structures.

Chapter 4 was concerned with repeatability and accuracies of structures printed using TPP. Shrinkage and adhesion are important considerations as they will cause deviations from the design and thus affect the performance of the structure. Frames can be implemented to contain the shrinkage to within the frame region, leaving the structure of interest intact. Using silanized glass slides promoted adhesion of the structure to the substrate, providing a solid foundation and a reduction in shrinkage. The combination of frames and silanized slides produced the best results. Further work looked at stitching larger area structures together, but stitching errors remain a large obstacle to overcome.

Woodpile structures were fabricated by changing the laser power between scan lines, and along individual scan lines. This produced structures with a geometry gradient and provided proof of principle for creating a GRIN metamaterial in this way. The cylindrical fishnet structure was suggested as the geometry to use in this work, due to the circular nature producing less shrinkage creating a more faithful print compared to the design. This allowed more ways to implement a gradient change, by also changing the number of spokes in a region, as well as the length of the spokes/gap between the rings, although only the former was investigated in this work. Overall, the cylindrical fishnet was a reproducible structure, but there are alignment issues to consider when adding more layers.

The cylindrical fishnet structure was investigated for its use as a metamaterial in chapter 5. Analytical calculations of the effective refractive index of the metamaterial allowed a surface understanding of the refractive index gradients achievable. Four lenses were designed using different maximum and minimum RI values to normalise a hyperbolic secant curve, and 7 closest matching unit cells from each were selected to simulate in COMSOL. The COMSOL simulations used a rectangular cut out approximation for the geometry rather than the cylindrical fishnet. The simulations found that there is a strong orientation dependency for this geometry where the orientation of the unit cell major axis with respect to the propagating wave will affect the resonances and the resulting RI value. Nonetheless, the unit cell simulation results found evidence of a large effective region for which a lens could function over a large bandwidth.

Finally, chapter 6 calculated the expected focal lengths of the four designed lenses using an analytical equation, and extracting the results from a 2D simulation. The focal length will increase with decreasing refractive index gradient due to the longer length needed to guide the light to a complete focus. However, with these longer lengths comes a reduction in focal power and an increase in focal spot size due to losses while propagating through the structure. A stepped RI profile using only 7 unit cells does not bring light to a good focus due to excessive diffraction between the boundaries, therefore a smoother profile with more unit cells should be used. This chapter also presented proof of concept fabricated lenses which showed that from a fabrication perspective a smoother RI gradient is also necessary to alleviate the stresses between the mismatched regions. Lens 4 produced the as designed structure when printed with 5 layers, however all structures failed when printed with layers equal to their focal length showing room for further development.

The aim of this work was to produce, using TPP, a metamaterial GRIN lens to operate in the 1 μm $-$ 2 μm waveband. The results in chapter 5 have shown that GRIN lenses made from the unit cells tested would be able to operate between 3 μm $-$ 2 μm if particular regions of resonance are avoided. The fabrication of a TPP GRIN metamaterial was demonstrated in chapter 6 and simulations predicted a focal length of 125 μm which is considerably less than the millimetre focal lengths achievable by traditional GRIN optics, but on par or greater than that of other metamaterial lenses. The investigation into the fabrication of metamaterials using TPP has indicated several key areas of improvement, and the use of any such TPP GRIN metamaterial lenses are likely to stay within research rather than commercial applications for the foreseeable future.

7.2 Future Direction

Before any of the lenses presented in this work (or otherwise) can be used commercially or within other research areas, there are a number of considerations to be met. This section presents three main areas of further research to be undertaken with respect to potential applications.

The current glass substrate is an issue as refraction at the interface will alter the path of the incoming rays. Further work could look to designing the lens to account for the phase shift of the wave, as in [154]. However, a more pragmatic solution would be to print directly onto the intended final object, such as on the end of a fibre [155]. This work found silanized glass slides produced better structures, which is not possible for some substrates, however silanized fibres can be produced [156]. For other substrates the use of a lower shrinkage resin or by altering the development process, as discussed in chapter 4, will remove the need for silanization. Alternative substrates will also necessitate the move to dip-in mode where structures are printed downwards, away from the substrate, rather than upwards with the light focused through it. This will require further work creating a new line width catalogue for the new resin as undertaken in chapter 3. Furthermore, the use of optical fibres as the printing substrate would require significant modifications to the Nanoscribe machine in order to position the fibre correctly, potentially necessitating the creation a home-build system.

A nominal frequency of 150 THz ($\lambda = 2$ μm), was chosen to investigate the lenses in this work, since this was away from the majority of resonances found from the simulations. Recent work has looked at mid-infrared quantum systems [157], and since this is not a widely used band, optical components working in this region are likely harder to come by. Therefore, the lenses in this work could position themselves well for such applications. However, further unit cell simulations, or an experimental investigation should be undertaken to understand how the cylindrical fishnet structure behaves in common communications wavelength regions such as 1.5 μm and 1.3 μm. Though the results from chapter 5 suggest these regions may be too close to resonances. Further work should once again look at the resin used to enable smaller line widths to be created, pushing the region of operation further towards shorter wavelengths.

The focal length of the lens is important to understand so that the lens length can be tailored to different applications. In this work, a quarter-pitch lens was designed which can be used to collimate a point source, or bring a collimated beam to a focus. A 0.23-pitch lens will do the same with the focal length at a working distance from the surface of the lens. Half-pitch lenses will create an inverted image on the back plane, of an object on the entrance surface. Finally, a 0.29-pitch lens will focus a point source from one side of the lens to the other, useful for coupling between fibres. Being able to freely alter the height of the lens will enable all these functionalities to open up. Further work is needed to produce good prints for these longer propagation lengths as discussed in chapter 6.

Additional work should look at experimentally investigating the spot size of the lenses. The results in this work suggested that longer propagation lengths, resulting from a shallower RI gradient, broadened the focal spot which could allow tailored mode matching for more efficient coupling [152]. However, longer propagation lengths will lead to more losses, so understanding the insertion losses of a coupling system will enable more power to be delivered where it needs to go. This is of particular interest to the quantum sensing field where preserving power across the system will enable lower power portable devices [158].

Appendices

Appendix A

Line Width Extraction Macro

This appendix provides the ImageJ macro used to extract the line measurements of each ascending scan array as discussed in section 3.2.3. The code can be pasted into the “batch processing by macro” dialogue box where it will process all images from your input folder, save the processed images to your output folder, and save the numerical results to an excel document.

There are several changes you will need to make which are highlighted in bold. Firstly, you may need to change the coordinates in “makeRectangle” so that the image is cropped within your desired area. Secondly, be sure to update the file extensions of the input images to match the file type of your images, here they are currently **.tif**. Next, you will need to input your specific file path (**FilePathResults**) and the name (**ResultsFile**) of the excel document you wish to save the results to. There is no need to create the excel file before hand, it will be created automatically when the function is first called and then auto-populated for each subsequent image. Finally when saving your images with the “saveAs” command, update the file type (“**Jpeg**”) and extension (.**jpg**) you wish to use along with the file path (**FilePathImages**). Note that wherever the macro says “filename” this will be auto-populated from the name of your file and thus does not need changing.

This work has used Fiji as the installation of ImageJ as it bundles a lot of plugins required for scientific image analysis. For further help using Fiji see reference [159]. The macro is as follows:

```
setBatchMode(false)
filename = getTitle();
dotIndex = indexOf(filename, “.”);
filename = substring(filename, 0, dotIndex);
makeRectangle(0, 0, 1280, 968);
run(“Crop”);
run(“8-bit”);
run(“Median...”, “radius=2”);
run(“Auto Threshold”, “method=Huang white”);
run(“Analyze Particles...”, “ display clear add”);
run(“ROIs to Label image”);
run(“Oriented Bounding Box”,“label=ROIs2Label_”+filename+“.tif ...
    show image=”+filename+“.tif”);
selectWindow(“Results”);
run(“Close”);
wait(1000);
Table.rename(“ROIs2Label_”+filename+“-OBox”,“Results”)
run(“Read and Write Excel”, “file=[C:/FilePathResults/ResultsFile.xlsx]”);
selectWindow(filename+“.tif”);
saveAs(“Jpeg”, “C:/FilePathImage/”+filename+“.jpg”);
wait(1000);
close(“*”);
```

Appendix B

Fill Fraction Calculations

This appendix provides the area equations used in the analytical effective refractive index calculations of this work. Section B.1 provides the area for the full cylindrical fishnet lens, and Section B.2 provides the area for the simplified rectangular cut out approximation. At the end of each section the MATLAB code is also provided to show full implementation of the analytical calculations.

B.1 Spoke-Ring Lens Area

This section outlines the area calculation for the cylindrical fishnet lens in order to calculate the fill fraction, where W is the line width, L is the length of a spoke/the distance between each ring and S is the number of starting spokes in the central circle. The total area enclosing the cylindrical fishnhet structure is,

$$A_{total} = \pi\left(R + \frac{W}{2}\right)^2,$$

where R is the radius of the full spokes lens (100 μm). The area calculation is split into two parts: calculating the area of the central ring and spokes followed by the area of all subsequent rings and spokes.

B.1.1 Central Spokes Region

For the central region calculation,

$$A_{inner\_total} = \pi\left(L + \frac{W}{2}\right)^2,$$

is the total area enclosing the central ring. To simplify the problem, the area of the empty space between each spoke is calculated and subtracted from A_{inner_total} as shown in figure B.1. The following expressions are introduced:

$$a = W/2,$$
$$r_1 = L - a,$$

where r_1 is the length of the inner radius of annulus.

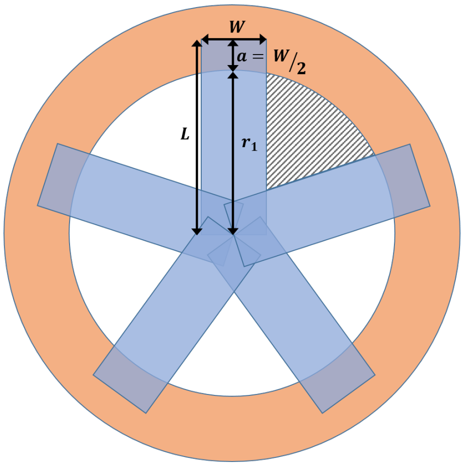

Figure B.1: Diagram of central region of cylindrical fishnet structure. Grey stripes shows the area to be derived.

Area of segment

Firstly it is necessary to recall the area of a segment of a circle subtended at the centre by a given angle. Figure B.2 provides the relevant notation, where the angle is 2ϕ radians, and the area of the relevant segment is area AXBC. The area is found from the area of the sector ACBO upon subtraction of the area of the triangle AXBO. Area ACBO is given by,

$$A_{ACBO} = \frac{\pi r_1}{2\pi} 2\phi = r_i^2 \phi.$$

The area of the triangle AXBO has area ABO given by,

$$A_{ABO} = \frac{1}{2} \cdot AB \cdot XO = \frac{1}{2} \cdot 2r_1 \sin\phi \cdot r_1 \cos\phi = r_1^2 \sin\phi \cos\phi.$$

Thus, the desired segment area is,

$$\begin{aligned} A_{AXBC} &= r_1^2(\phi - \sin\phi\cos\phi), \\ &= \frac{1}{2} r_1^2 \left(2\phi - \sin 2\phi\right). \end{aligned}$$

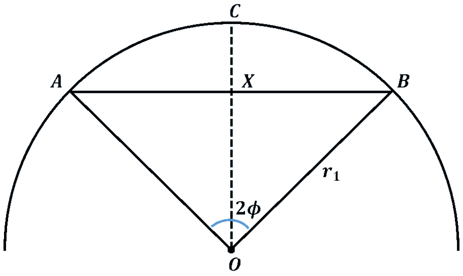

Figure B.2: Diagram providing notation for area of segment derivation.

Empty space between two spokes

Figure B.3 depicts two spokes of the structure separated by angle θ radians. The half circle shown has a radius r_1 which forms the inner edge of the structure annulus. The empty space between the spokes is the shaded shape with area given by A_1PA_2F which is to be derived.

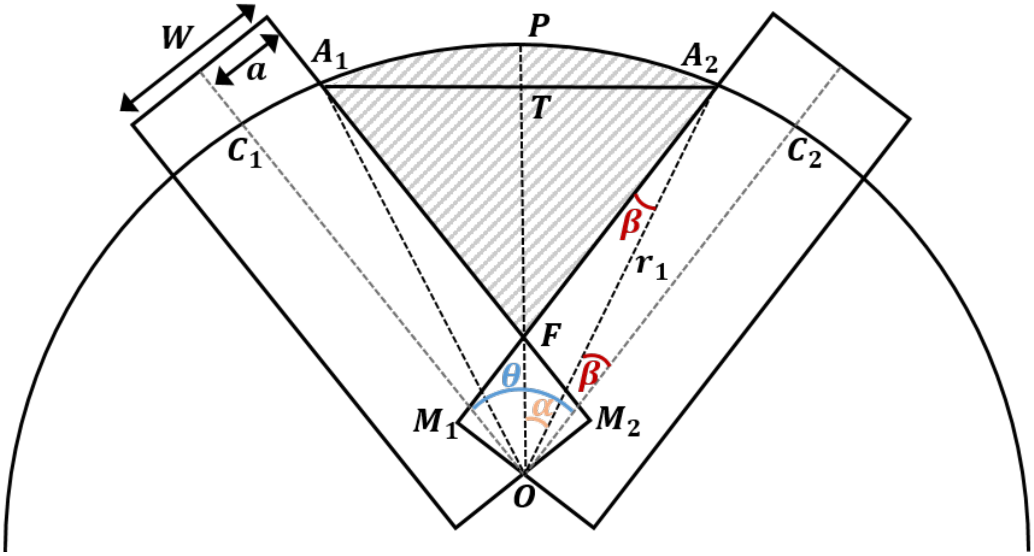

Figure B.3: Diagram providing notation for derivation of empty space between two spokes.

The construction OP is the bisector of angle θ. O is the centre of the circle from which lines OA_1 and OA_2 connect to the intersections A_1 and A_2 of a side of the spoke with the circle. Angle α and β are defined in the positions shown with respect to the constructions OA so that,

$$\alpha + \beta = \theta/2.$$

In addition, β is known from,

$$\sin\beta = a/r_1.$$

From the prior section, the area of the segment A_1PA_2T is,

$$A_{A_1PA_2T} = r_1^2(\alpha - \sin\alpha\cos\alpha).$$

This area must be added to the triangle A_1A_2F, therefore the lengths TA_2 and TF must be defined. In the triangle TA_2O we have,

$$TA_2 = r_1 \sin\alpha.$$

Now,

$$TF = TO - FO,$$

where TO is defined from triangle TA_2O as,

$$TO = r_1 \cos\alpha.$$

Angle $\widehat{OFM_2}$ equals $\theta/2$, hence in triangle OFM_2 we have,

$$FO = a \operatorname{cosec}\theta/2,$$

so that TF can be defined by,

$$TF = r_1\cos\alpha - a\operatorname{cosec}\theta/2.$$

Hence, area $\mathrm{A}_1\mathrm{A}_2\mathrm{F}$ is given by,

$$\begin{aligned} A_{A_1A_2F} &= 2 \times \frac{1}{2} TA \times TF, \\ &= r_1 \sin\alpha \left(r_1 \cos\alpha - a \operatorname{cosec}\theta/2 \right). \end{aligned}$$

The total area of a single segment of empty space between two spokes is given by,

$$\begin{aligned} A_{A_1PA_2F} &= A_{A_1A_2F} + A_{A_1PA_2T} \\ &= r_1 \sin\alpha \left(r_1 \cos\alpha - a \operatorname{cosec}\theta/2 \right) + r_1^2(\alpha - \sin\alpha\cos\alpha), \\ &= r_1^2\alpha = ar_1 \sin\alpha \operatorname{cosec}\theta/2. \end{aligned}$$

Eliminating α and β gives the explicit equation,

$$A_{sector} = \left(r_1^2 \frac{\theta}{2} + a^2 \cot\theta/2 \right) - \left(r_1^2 \arcsin a/r_1 + a\sqrt{r_1^2 - a^2} \right).$$

For a full circle with S equally spaced spokes, the circle is divided in to S arcs each separated by angle θ such that,

$$\theta = 2\pi/S,$$

so that the total empty area is,

$$A_{empty} = S \times A_{sector},$$

unless $\theta \leq 2\beta$ in which case $A_{empty} = 0$. Therefore the area of the central region A_{inner} is,

$$A_{inner} = A_{inner\_total} - A_{empty}.$$

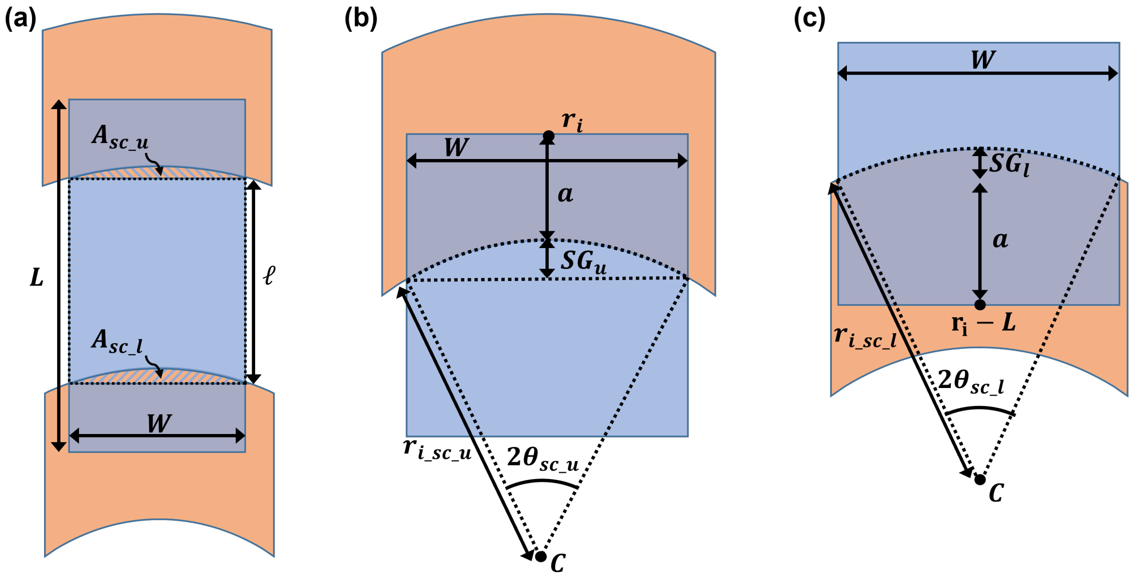

Figure B.4: Diagram and definitions of the areas and lengths for the overlap between the spokes (blue) and rings (orange). C represents the the centre of the overall structure.

B.1.2 Outer Rings and Spokes Calculation

The area of the rest of the spokes structure is calculated iteratively adding the area of each new ring and set of intervening spokes to a cumulative area ($A_{cumulative}$). Here, r_i is defined as the current ring radius which increases by L for each step, and S_i is the current number of spokes, increasing by S for each step. Each iteration starts by calculating the area of the annulus between the current ring and the ring preceding it using,

$$A_{inner\_annulus} = \pi\left(\left(r_i - a\right)^2 - \left((r_i - L) + a\right)^2\right),$$

where a was previously defined as $W/2$.

Following this, the area of a single spoke is calculated. While simplifying the calculation to a rectangle with an area of L×W would be appropriate for the outer regions of the lens, non-negligible differences are created towards the central regions of the lens where the overlaps are proportionally larger. Therefore, each spoke is modelled as a curved rectangle accounting for the overlap of the rings at each end of the spoke. Figure B.4 demonstrates the situation graphically, as well as defining the key parameters used for the calculation.

To begin, the area of the upper semicircle is calculated by,

$$A_{sc\_u} = \frac{1}{2} r_{i\_sc\_u}^2 \times (2\theta_{sc\_u} - sin(2\theta_{sc\_u})),$$

where,

$$r_{i\_sc\_u} = R - a,$$

is the radius measured from the center of the spokes lens to the bottom of the current ring and

$$2\theta_{sc\_up} = \sin^{-1}(\frac{W}{2r_{i\_sc\_u}}),$$

is the angle of the circular segment with a chord length of W. The sagita of the upper semicircle is given by,

$$SG_{sc\_u} = r_{sc\_u} - \sqrt{r_{i\_sc\_u}^2 - a^2}.$$

The same values are defined for the lower semicircle so that,

$$\begin{aligned} A_{sc\_l} &= \frac{1}{2} r_{i\_sc\_l}^2 \times (2\theta_{sc\_l} - sin(2\theta_{sc\_l})), \\ r_{sc\_l} &= (r_i - L) + a, \\ 2\theta_{sc\_l} &= \sin^{-1}(\frac{W}{2r_{i\_sc\_l}}), \\ SG_{sc\_l} &= r_{i\_sc\_l} - \sqrt{r_{i\_sc\_l}^2 - a^2}. \end{aligned}$$

After this, a new rectangle is defined as having side length ℓ given by,

$$\ell = L - (a + SG_{sc\_u}) - (a - SG_{sc\_l}),$$

so that the area of a single spoke is given by,

$$A_{single\_spoke} = (\ell \times W) + A_{sc\_u} - A_{sc\_l},$$

and the area of all spokes for this iteration is,

$$A_{all\_spokes\_i} = A_{single\_spoke} \times S_i.$$

The following condition is then applied,

$$A_i = \begin{cases} A_{ring\_i} + A_{inner\_annulus} & A_{inner\_annulus} \leq A_{all\_spokes\_i} \\ A_{ring\_i} + A_{all\_spokes\_i} & A_{all\_spokes\_i} < A_{inner\_annulus}, \end{cases}$$

where the upper condition corresponds to overlapping spokes so that you need only add the inner annulus area to the current ring annulus (A_{ring_i}). Else, the area for this iteration is the sum of the spokes area ($A_{all\_spokes\_i}$) and (A_{ring_i}),

$$A_{ring\_i} = \pi((r_i + a)^2 - (r_i - a)^2).$$

This area is then added to the cumulative area until each ring/spokes pair is calculated leading to a final area calculation of,

$$A_{spokes} = A_{cumulative} + A_{inner}.$$

This is then passed back into the main code for further calculations to work out the fill fraction by dividing A_{spokes} by A_{total} as defined at the beginning of this section. The full code used to calculate the effective refractive index is as follows:

```
%% Maxwell Garnett Analytical Calculations for Refractive Index
   %%
```

```
% This code will calculate the analytical refractive index for a
   range of line widths and starting spokes for the CYLINDRICAL
   FISHNET lens.
clc; clear all; close all;

%% Define Parameters

% Loop Parameters
Lv = 1;                      % Ring Radius/voxel length
Sp = 2:1:10;                 % "starting" number of spokes
Wv = load('linewidthresults.mat'); % Line Width (nm)

% Lens parameters
diameter = 200;
radius = diameter/2;

% Material Properties
n_0 = 1.492;
eps_0 = n_0^2; % polymer
eps = 1;       % air

%% Calculate Maxwell Garnet Neff %%

FFlens = zeros(size(Wv,1),size(Sp,2));

for i = 1:size(Sp,2)
    for j = 1:size(Wv,1)
        if isnan(Wv(j))
            FFlens(j,i)  = NaN;
        else
            UnitCellArea = pi*((radius+(Wv(j)/2))^2); %Circle
            LensArea = spokesarea(Sp(i),Wv(j),Lv,radius);
            FFlens(j,i) = LensArea/UnitCellArea;
        end
    end
end

MG_neff = MGT(eps_0,eps,FFlens);

%% Functions %%

function totalarea = spokesarea(S,W,L,radius)
    % Area Calculation for Spokes Lens %

    % Calculate Area of Central Region
```

```
Area = pi*((L+(W/2)))^2; % Total area of central region
a = W/2;
ri = L-a;
theta = (2*pi)/S;
beta = asin(a/ri);
if theta <= 2*beta
    empty = 0;
else
    sector_area = (ri^2*(theta/2) + a^2*cot(theta/2))  -  ...
        (ri^2*asin(a/ri) + a*sqrt(ri^2 - a^2));
    empty = (sector_area)*S;
end

Ainnerspokes = Area - empty;

% Calculate Area of Successive Rings
current_spokes = S*2;
Area_cum = 0;
for r = 2*L:L:radius %radii of each ring

    inner_annulus_area = pi*((r - W/2)^2 - (r-L+W/2)^2);

    % calculate area of single spoke
    % upper semicircle
    r_upper = r-(W/2);
    angle_upper = asin(W/(2*r_upper));
    area_upper = 0.5*r_upper^2*(2*angle_upper - sin(2*
       angle_upper));
    sagitta_upper = r_upper - sqrt(r_upper^2 - (W/2)^2);

    % lower semicircle
    r_lower = (r-L)+(W/2);
    angle_lower = asin(W/(2*r_lower));
    area_lower = 0.5*r_lower^2*(2*angle_lower - sin(2*
       angle_lower));
    sagitta_lower = r_lower - sqrt(r_lower^2 - (W/2)^2);


    % enclosing rectangle length
    distance_upper = (W/2) + sagitta_upper;
    distance_lower = (W/2) - sagitta_lower;
    adjusted_length = L - distance_upper - distance_lower;

    % area spoke
    single_spoke_area = (adjusted_length*W) + area_upper -
```

```
               area_lower;

            % area total spokes
            spokes_area = single_spoke_area*current_spokes;

            % if spokes area > annulus area set area to add as
               annulus
            if inner_annulus_area <= spokes_area
                annulus_area = pi*((r + W/2)^2 - (r_lower)^2);
                Area_cum = Area_cum + annulus_area;

                % if gaps between spokes, add spokes area + upper
                   ring area
            else
                ring_area = pi*((r+W/2)^2-(r-W/2)^2);
                Area_cum = Area_cum + spokes_area + ring_area;
            end
            current_spokes = current_spokes+S;
        end
        totalarea = Area_cum + Ainnerspokes;
end

function n = MGT(epsi,epsh,FF)
    % Maxwell Garnet Calculation %
    bracket = (epsi - epsh) / (epsi + 2*epsh);
    num = epsh.*(1 + 2.*FF.*bracket);
    den = 1 - FF.*bracket;
    epse = num./den;
    n = sqrt(epse);
end
```

B.2 Rectangular Cut Out Area

This section outlines the area calculation for the rectangular cut out approximation. As with the previous section W is the line width, L is the length of a spoke/the distance between each ring and S is the number of starting spokes in the central circle. For this approximation the unit cell is assumed to be at the outer edge of the corresponding cylindrical fishnet with radius R (= 100 μm) so that:

$$S_{total} = S \times (R - L),$$

is the total number of spokes in the outer ring. Therefore the distance between each spoke is,

$$d_{spokes} = \frac{2\pi R}{S_{total}}.$$

This gives the total area enclosing the unit cell as,

$$A_{Total} = L \times d_{spokes},$$

and the area of the inner rectangle or air gap between each spoke is,

$$A_{air} = (L - W) \times (d_{spokes} - W).$$

To calculate the area of the unit cell we apply the condition,

$$A_{UC} = \begin{cases} A_{total} & A_{air} < 0 \\ A_{total} - A_{air} & 0 \leq A_{air}, \end{cases}$$

where $A_{air} < 0$ corresponds to overlapping spokes leading to a fill fraction of 1 as there is no empty space. As before the fill fraction is then calculated as,

$$F = A_{UC}/A_{total}$$

ready to be used in Equation 5.1. The full MATLAB code is as follows:

```
%% Maxwell Garnett Analytical Calculations for Refractive Index
   %%
% This code will calculate the analytical refractive index for a
```

```
   range of line widths and starting spokes for the RECTANGULAR
   CUT OUT approximation.
clc; clear all; close all;

%% Define Parameters

% Loop Parameters
Lv = 1;                       % Ring Radius/voxel length
Sp = 2:1:10;                  % "starting" number of spokes
Wv = load('linewidthresults.mat'); % Line Width (nm)

% Lens parameters
diameter = 200;
radius = diameter/2;

% Material Properties
n_0 = 1.492;
eps_0 = n_0^2; % polymer
eps = 1;       % air

%% Calculate Maxwell Garnet Neff %%

FF_square = zeros(size(Wv,1),size(Sp,2));

for i = 1:size(Sp,2)
    for j = 1:size(Wv,1)
        if isnan(Wv(j))
            FF_square(j,i)   = NaN;
        else
            FF_square(j,i)  = square_ff(Sp(i),Wv(j),Lv,radius);
        end
    end
end

MG_neff = MGT(eps_0,eps,FFlens);

%% Functions

function fill_fraction = square_ff(S,W,L,radius)
    % Fill Fraction for Square Cut Out %
    no_spokes = S*(radius - L);
    spoke_distance = (2*pi*radius)/no_spokes;
    Outer_Square = L * spoke_distance;

    Inner_Square = (L-W)*(spoke_distance - W);
```

```
    if Inner_Square < 0
        area = Outer_Square;
    else
        area = Outer_Square - Inner_Square;
    end

    fill_fraction = area/Outer_Square;
end

function n = MGT(epsi,epsh,FF)
    % Maxwell Garnet Calculation %
    bracket = (epsi - epsh) / (epsi + 2*epsh);
    num = epsh.*(1 + 2.*FF.*bracket);
    den = 1 - FF.*bracket;
    epse = num./den;
    n = sqrt(epse);
end
```

Appendix C

Simulation and Parameter Retrieval Setup

This appendix presents an investigation into two different COMSOL simulation set ups, using a dielectric slab to benchmark the correct parameter retrieval and simulation methods. A discussion is undertaken into considerations for the parameter retrieval method.

C.1 COMSOL Model Comparisons

Two simulations using the RF module were adapted from COMSOL documentation. The first model (Sim 1) used the "Frequency Selective Surface" application file provided by COMSOL [160], and the second (Sim 2) was based on a webinar hosted by COMSOL [136]. Figure C.1 show the domains and boundary conditions applied to each model. In both, the central grey chequered region contains the structure under investigation with the rest of the simulation domain being filled with air.

In each case, floquet-PBCs are used to simulate an infinite material and/or 2D array

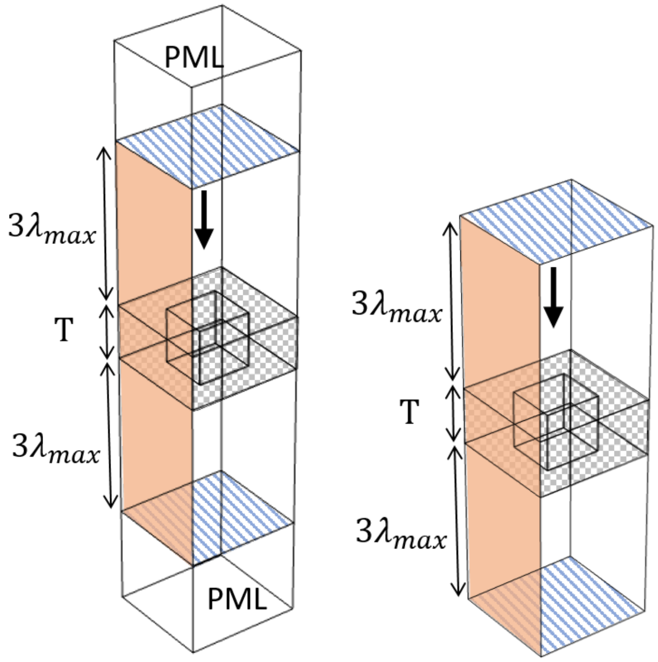

(a) (b)

Figure C.1: COMSOL simulation domain for (a) Sim 1 and (b) Sim 2. Blue stripes are the periodic ports exciting a wave travelling from top to bottom (indicated by black arrow). Orange shaded is the floquet periodic boundary condition applied in pairs to opposing vertical faces. The grey chequered central region is the rectangular cut out geometry with IP-L material definition n = 1.492 [135], $\varepsilon = n^2$ and $\mu = 1$. There is a $3\lambda_{max}$ gap between the ports and the structure surfaces which is filled with air, and the thickness of the structure is T = 1 μm.

of unit cells. PBCs are set up so that opposing faces are paired as source and destination boundaries. This enables the physics-controlled meshing sequence to create identical surface meshes on the paired boundaries. The port boundary conditions are placed either on the interior boundaries of the perfectly matched layers (PMLs) (Sim 1), or on the outside boundaries of the simulation domain (Sim 2). These automatically determine the transmission (S_{21}) and reflection (S_{11}) coefficients for each frequency.

In Sim 1, since the ports are on an interior boundary the slit condition is applied. For the example COMSOL provided, the combination of Domain-backed type slit port and PMLs is used as higher order diffraction modes were not of interest. Whereas in Sim 2, there are no PMLs, and a Diffraction order port is auto-added for each diffraction order and polarisation. A 1 μm$\times$0.8 μm$\times$1 μm (length, width, thickness) dielectric slab was simulated using both models and the results are shown in figure C.2. Figure C.2a shows the results of Sim 1 with a clear interference pattern in the results, whereas figure C.2b shows a smoother line using Sim 2.

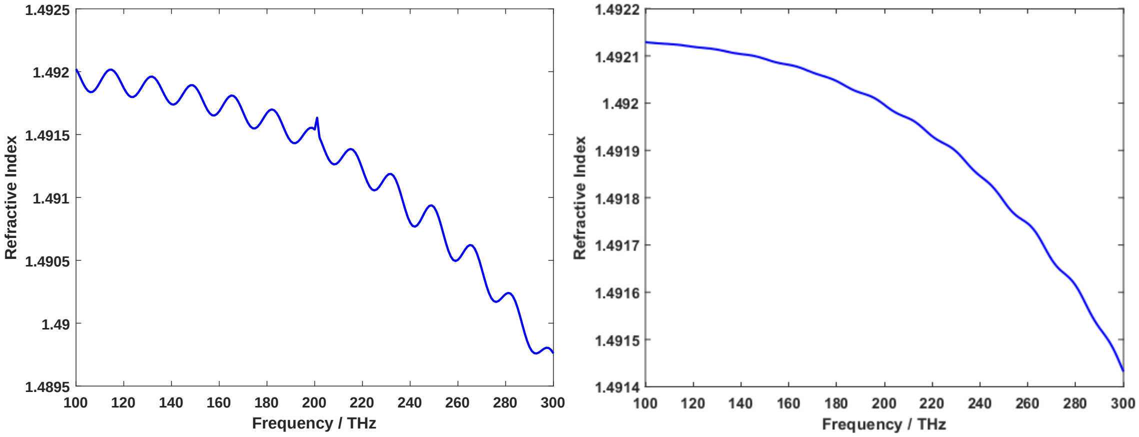

(a) (b)

Figure C.2: (a) and (b) show the retrieved RI for Sim 1 and Sim 2 respectively.

Figure C.3 shows how the interference pattern changes when changing the air gap between the dielectric slab and the ports. The further away the port is from the surface of the dielectric slab, the less pronounced the pattern. The results in table C.1 show that the pattern is consistent with the theoretical interference equation,

$$2nd = p\lambda_p, \tag{C.1}$$

where n is the slab RI, d is the gap between the port and the top face of the dielectric slab, p is the order of reflection and λ_p is the wavelength of the interference. The slight difference between the theoretical values and the actual values may be due to one of the interfaces being into the dielectric rather than being a true reflective interface.

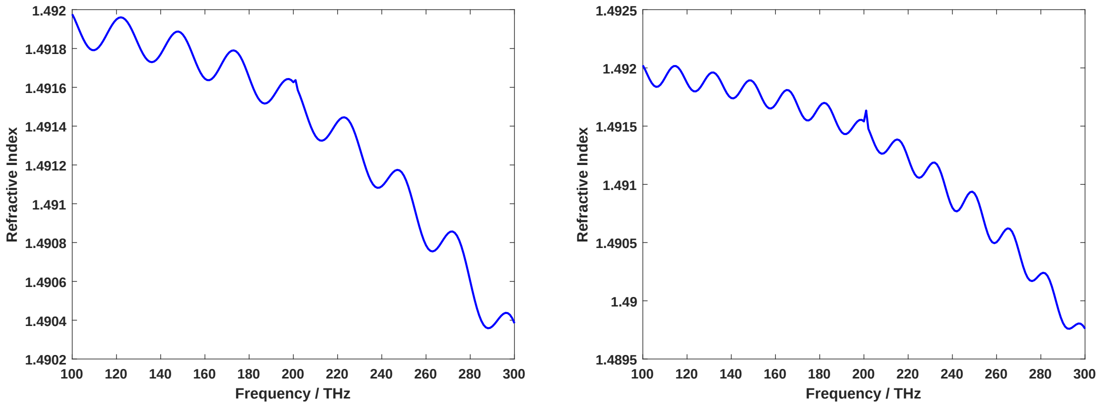

(a) d = $2\lambda_{max}$ (b) d = $3\lambda_{max}$

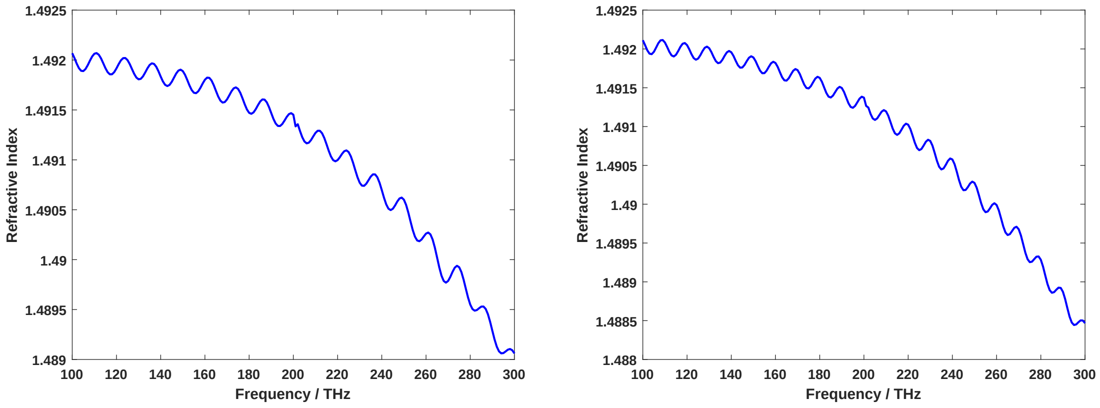

(c) d = $4\lambda_{max}$ (d) d = $5\lambda_{max}$

Figure C.3: (a) – (d) retrieved effective refractive index for the dielectric slab with different distances, d, between the port and dielectric surface where λ_{max} = 3 μm is set to the smallest frequency used (f_i = 100 THz).

Table C.1: Table comparing the theoretical interference frequency to the actual frequency as shown in figure C.3.

Air Gap (λ_{max} = 3 µm)	**Theory / THz**	**Actual / THz**
$2\lambda_{max}$	25	26
$3\lambda_{max}$	16.6	16
$4\lambda_{max}$	12.5	14
$5\lambda_{max}$	10	12

Figure C.4a and C.4b show how changing the width (W) and thickness (T) of the slab affects the retrieved RI. The overall dimensions were 1 μm$\times$W$\times$1 μm and 1 μm$\times$0.8 μm$\times$T respectively. The width of the slab did reduce the slope slightly for the two largest widths. However, a single width will not be set for the full unit cell study as changing the width is part of the investigation. Increasing the thickness of the slab does have a significant affect on the slope of the results. This is likely due to reflections and phase differences within the structure altering the overall results.

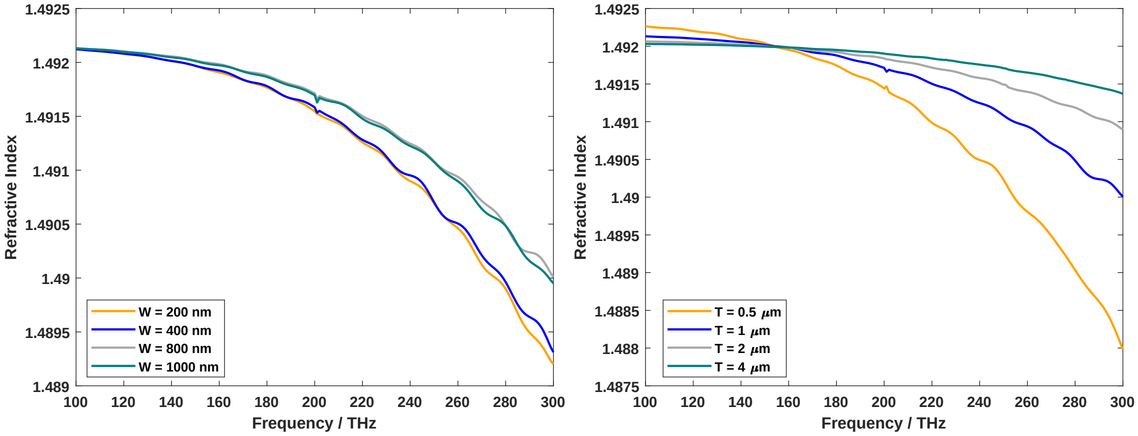

(a) (b)

Figure C.4: Retrieved RI for the dielectric slab for changing unit cell (a) width and (b) thickness.

C.2 Parameter Retrieval: Branching

When simulating the dielectric slab with different thicknesses the branch selection method using equation 5.8 did not always work. The value that is rounded to find the first branch is given by,

$$V_0 = -\frac{1}{2\pi}\left[\ln(e^{inkd})\right]''. \tag{C.2}$$

The calculated V_0 value is presented in table C.2 for the 4 different slab thicknesses, in addition to the selected branch by rounding this value, and the actual branch based on trial an error in selecting the first value for m. Figure C.5 shows an example of how the retrieved RI looks with different initial branch values, showing that for the T = 4 μm thick slab is retrieved correctly for $m_i = 2$ rather than the $m_i = 0$ based on equation 5.8.

Table C.2: Results of the V_0 values and selected and required initial branch indexes for each of the slab thicknesses.

Thickness (μm)	V_0	$m_{selected}$	$m_{required}$
0.5	−0.2489	0	0
1	−0.4977	0	0
2	0.0045	0	1
4	0.0092	0	2

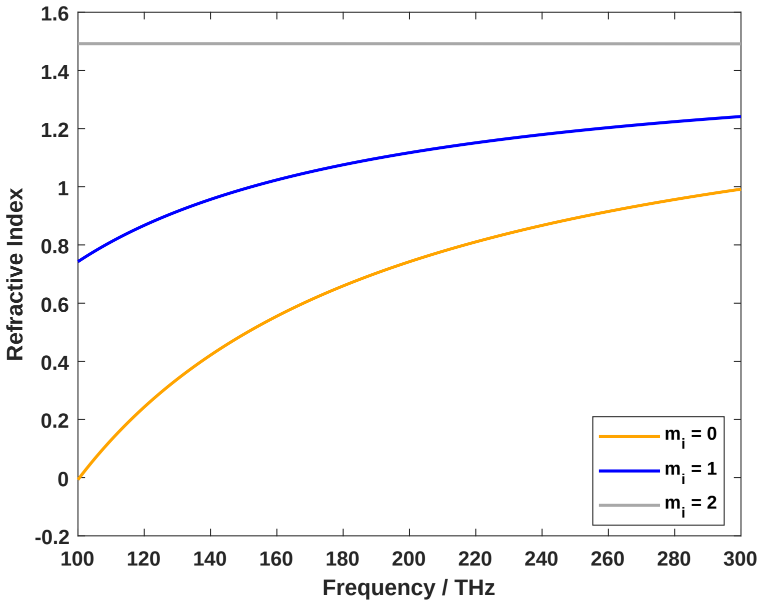

Figure C.5: Retrieved RI for T = 4 μm thick dielectric slab for three different initial branch values. Setting $m_i = 2$ allows the slab to be correctly resolved.

C.3 Conclusion

The gradient of the slope for the retrieved RI for the dielectric slab is small ($\sim 10^{-6}$), therefore there are diminishing returns for simulating at larger thicknesses due to the drastically increasing simulation times. Additionally, there is uncertainty surrounding the branch selection for thicknesses larger than 1 μm. Therefore the main metamaterial study used a thickness of 1 μm, which is can also be deemed the thickness of a unit cell due to it being the approximate thickness of a single layer made using TPP. It is likely that further tweaks need to be made to the simulation domains to ensure it is thickness invariant, in addition to further investigating the branch selection method, where potentially implementing a piecewise selection function is appropriate mathematically, but should be confirmed physically.

Appendix D

Parameter Retrieval Code

```
%%%%%%%%%%%%%%%% EFFECTIVE PARAMETER RETRIEVAL CODE
   %%%%%%%%%%%%%%%

% This code can be used to retrieve the effective material
   parameters from the s-parameters of a metamaterial.
%
% To use this code save the frequency, S11, S21, S11dB and S21dB
   data in a single export from comsol. Change the file path to
   your save location, change the file name to your file name.
%
% You will also need the thickness of your metamaterial (d), and
   the thickness of any air/vacuum gaps between each port and the
    metamaterial surface (prepad and postpad).
%
% The references used to create this work:
%   Chen et al., "Robust method to retrieve the constitutive
%   effective parameters of metamaterials", Phys. Rev. E, 70(1),
   2004.
%
%   Wang et al., "An improved approach to determine the branch
%   index for retrieving the constitutive effective parameters
%   of metamaterials", J. Electromagn. Waves Appl., 25(1), 2011

%
   %%%%%%%%%%%%%%%%%%%%%%%%%%%%%%%%%%%%%%%%%%%%%%%%%%%%%%%%%%%%%%%%%%

clc; close all; clear all;
```

```
%% % Load data %%%%

% Extract the data into their respective arrays
% 1) Be sure to note which order you saved the data in the comsol
    file so the correct data is assigned to the correct variable.
% 2) The conjugate of S11 S21 is taken to account for sign
   convetion of iwt between comsol and the retrieval method
% 3) The dB data has been imported to allow for plotting but is
   not required for the parameter retrieval.

filepath = 'C:\YourFilePath\';
filename   = 'YourFileName'

data = table2array(readtable([filepath,filename]));

f = data(1:5:end,:);         % frequency data
S11= conj(data(2:5:end,:));  % S11
S21 = conj(data(3:5:end,:)); % S21


%% %% Parameter Retrieval %% %%

% Definitions
c = 299792458.0;  % speed of light
k_0 = 2.0*pi*f/c; % wavenumber in vacuum

d = 0.000001; % thickness of metamaterial
prepad = ((6*(2.9979e8/100e12)+d)/2)-d/2;
postpad = prepad;

% Remove padding on both side of the metamaterial slab.
exp_prepad = exp(-1.0i*k_0*prepad);
exp_postpad = exp(-1.0i*k_0*postpad);
S11 = S11 .* exp_prepad.*exp_prepad;
S21 = S21 .* exp_prepad.*exp_postpad;

% %%% Calculate the impedance. %
z = sqrt(((1+S11).^2-S21.^2)./ ...
         ((1-S11).^2-S21.^2));

% Adjust the sign to make sure real part is positive.
z = z.*(real(z)>=0.0) - z.*(real(z)<0.0);

% Factors for ease of calculation later on.
```

```
div = (z-1.0)./(z+1.0);
expink = S21./(1.0-S11.*div);
invkd = (k_0*d).^-1;
imlogexp = imag(log(expink));
relogexp = real(log(expink));

% Calculate the refractive index using branch selection criterion
    %

% pre-allocate arrays.
n = zeros(size(f));
value = zeros(size(f));
branch = zeros(size(f));

% calculate first point.
value(1) = -imag(log(expink(1)))/(2*pi);
branch(1) = round(value(1));

n(1) = invkd(1)*((imlogexp(1)+2*pi*branch(1)) - 1.0i*relogexp(1))
   ;

% calculate following points.
for i = 2:length(n)
    value(i) = (imlogexp(i-1)-imlogexp(i))/(2*pi);
    branch(i) = round(value(i)) + branch(i-1);
    n(i) = invkd(i)*((imlogexp(i)+2*pi*branch(i)) - 1.0i*relogexp
       (i));
end

% Calculate eps and mu if required %
eps_eff = n./z;
mu_eff = n.*z;
```

Appendix E

Unit Cells

(a) W 517 S 10

(b) W 427 S 10

(c) W 487 S 5

(d) W 374 S 4

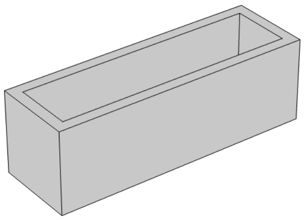

(e) W 273 S 2

Figure E.1: Images of unit cells used in Lens 1.

(a) W 548 S 10

(b) W 523 S 10

(c) W 474 S 10

(d) W 501 S 7

(e) W 392 S 7

(f) W 332 S 5

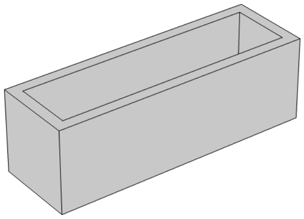

(g) W 273 S 2

Figure E.2: Images of unit cells used in Lens 2.

(a) W 548 S 10

(b) W 504 S 10

(c) W 458 S 10

(d) W 399 S 10

(e) W 339 S 10

(f) W 273 S 10

Figure E.3: Images of unit cells used in Lens 3.

(a) W 548 S 10 (b) W 548 S 9

(c) W 548 S 8 (d) W 548 S 6

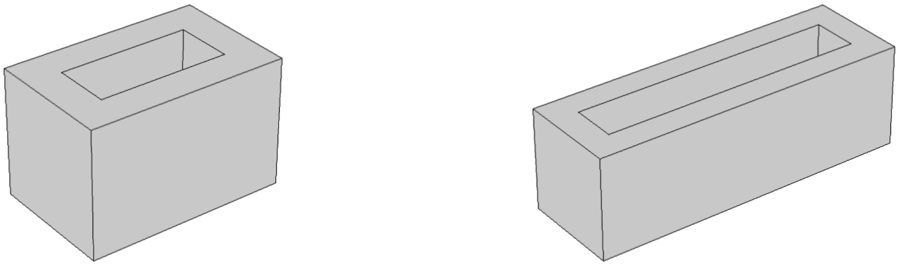

(e) W 548 S 4 (f) W 548 S 2

Figure E.4: Images of unit cells used in Lens 4.

Bibliography

[1] W. Cai and V. Shalaev, *Optical Metamaterials*. Springer New York, 2010. [Online]. Available: http://link.springer.com/10.1007/978-1-4419-1151-3

[2] D. R. Smith, J. J. Mock, A. F. Starr, and D. Schurig, "Gradient index metamaterials," *Physical Review E*, vol. 70, p. 42, 2005. [Online]. Available: https://doi.org/10.1103/PhysRevE.71.036609

[3] J. B. Pendry, "Negative refraction makes a perfect lens," *Physical Review Letters*, vol. 85, pp. 3966–3969, 2000. [Online]. Available: https://doi.org/10.1103/PhysRevLett.85.3966

[4] D. T. Moore, "Gradient-index optics: a review," *Applied Optics*, vol. 19, p. 1035, 1980. [Online]. Available: https://doi.org/10.1364/AO.19.001035

[5] A. O. Pinchuk and G. C. Schatz, "Metamaterials with gradient negative index of refraction," *Journal of the Optical Society of America A*, vol. 24, p. A39, 2007. [Online]. Available: https://doi.org/10.1364/JOSAA.24.000A39

[6] J. Teichman, J. Holzer, B. Balko, B. Fisher, and L. Buckley, "Gradient index optics at darpa," 2013.

[7] K.-S. Lee, D.-Y. Yang, S. H. Park, and R. H. Kim, "Recent developments in the use of two-photon polymerization in precise 2d and 3d microfabrications," *Polymers for Advanced Technologies*, vol. 17, pp. 72–82, 2006. [Online]. Available: https://doi.org/10.1002/pat.664

[8] C. Gomez-Reino, M. V. Perez, and C. Bao, *Gradient-Index Optics : Fundamentals and Applications*. Springer Berlin Heidelberg, 2002.

[9] D. T. Moore, "Gradient index optics," 2010.

[10] S. Cornbleet, *Microwave Optics*. Academic Press, 1976.

[11] J. C. Maxwell, *The Scientific Papers of James Clerk Maxwell*, W. D. Niven, Ed., 1965.

[12] R. K. Luneburg, *Mathematical Theory of Optics*. University of California Press, 1966.

[13] A. Fletcher, T. Murphy, and A.Young, "Solutions of two optical problems," *Proceedings of the Royal Society of London. Series A. Mathematical and Physical Sciences*, vol. 223, pp. 216–225, 1954. [Online]. Available: https://doi.org/10.1098/rspa.1954.0110

[14] R. Wood, *Physical Optics*. Macmillan, 1905.

[15] P. J. Sands, "Third-order aberrations of inhomogeneous lenses," *JOSA, Vol. 60, Issue 11, pp. 1436-1443*, vol. 60, pp. 1436–1443, 1970. [Online]. Available: https://doi.org/10.1364/JOSA.60.001436

[16] D. S. Kindred and D. T. Moore, "Design, fabrication, and testing of a gradient-index binocular objective," *Applied Optics, Vol. 27, Issue 3, pp. 492-495*, vol. 27, pp. 492–495, 1988. [Online]. Available: https://doi.org/10.1364/AO.27.000492

[17] L. G. Atkinson, S. N. Houde-Walter, D. T. Moore, D. P. Ryan, and J. M. Stagaman, "Design of a gradient-index photographic objective," *Applied Optics, Vol. 21, Issue 6, pp. 993-998*, vol. 21, pp. 993–998, 1982. [Online]. Available: https://doi.org/10.1364/AO.21.000993

[18] M. Kawazu and Y. Ogura, "Application of gradient-index fiber arrays to copying machines," *Applied Optics*, vol. 19, pp. 1105–1112, 1980. [Online]. Available: https://doi.org/10.1364/AO.19.001105

[19] G. von Bally, E. Brune, and W. Mette, "Holographic endoscopy with gradient-index optical imaging systems and optical fibers," *Applied Optics*, vol. 25, pp. 3425–3429, 1986. [Online]. Available: https://doi.org/10.1364/AO.25.003425

[20] H. Nishi, H. Ichikawa, M. Toyama, and I. Kitano, "Gradient-index objective lens for the compact disk system," *Applied Optics*, vol. 25, pp. 3340–3344, 1986. [Online]. Available: https://doi.org/10.1364/AO.25.003340

[21] R. W. Gilsdorf and J. C. Palais, "Single-mode fiber coupling efficiency with graded-index rod lenses," *Applied Optics*, vol. 33, pp. 3440–3445, 1994. [Online]. Available: https://doi.org/10.1364/AO.33.003440

[22] P. Sinai, "Correction of optical aberrations by neutron irradiation," *Applied Optics*, vol. 10, pp. 99–104, 1971. [Online]. Available: https://doi.org/10.1364/AO.10.000099

[23] J. B. Macchesney, "Materials and processes for preform fabrication-modified chemical vapor deposition and plasma chemical vapor deposition," *Proceedings of the IEEE*, vol. 68, pp. 1181 – 1184, 1980. [Online]. Available: https://doi.org/10.1109/PROC.1980.11826

[24] Y. Ohtsuka and T. Sugano, "Studies on the light-focusing plastic rod. 14: Grin rod of cr-39–trifluoroethyl methacrylate copolymer by a vapor-phase transfer process," *Applied Optics*, vol. 22, pp. 413–417, 1983. [Online]. Available: https://doi.org/10.1364/AO.22.000413

[25] Y. Ohtsuka and Y. Koike, "Studies on the light-focusing plastic rod. 18: Control of refractive-index distribution of plastic radial gradient-index rod by photocopolymerization," *Applied Optics*, vol. 24, pp. 4316–4320, 1985. [Online]. Available: https://doi.org/10.1364/AO.24.004316

[26] J. Valentine, S. Zhang, T. Zentgraf, E. Ulin-Avila, D. A. Genov, G. Bartal, and X. Zhang, "Three-dimensional optical metamaterial with a negative refractive index," *Nature*, vol. 455, pp. 376–379, 2008. [Online]. Available: https://doi.org/10.1038/nature07247

[27] D. J. Barber and I. C. Freestone, "An investigation of the origin of the colour of the lycurgus cup by analytical transmission electron microscopy," *Archaeometry*, vol. 32, pp. 33–45, 1990. [Online]. Available: https://doi.org/10.1111/j.1475-4754.1990.tb01079.x

[28] B. J. C., "On the rotation of plane of polarisation of electric wave by a twisted structure," *Proceedings of the Royal Society of London*, vol. 63, pp. 146–152, 1 1898. [Online]. Available: https://doi.org/10.1098/rspl.1898.0019

[29] W. Kock, "Metal-lens antennas," *Proceedings of the IRE*, vol. 34, pp. 828–836, 1946. [Online]. Available: https://doi.org/10.1109/JRPROC.1946.232264

[30] J. Brown, "Artificial dielectrics having refractive indices less than unity," *Proceedings of the IEE - Part IV: Institution Monographs*, vol. 100, pp. 51–62, 1953. [Online]. Available: https://doi.org/10.1049/pi-4.1953.0009

[31] W. Rotman, "Plasma simulation by artificial dielectrics and parallel-plate media," *IRE Transactions on Antennas and Propagation*, vol. 10, pp. 82–95, 1962. [Online]. Available: https://doi.org/10.1109/TAP.1962.1137809

[32] "British museum - the lycurgus cup." [Online]. Available: https://www.britishmuseum.org/collection/object/H_1958-1202-1

[33] V. G. Veselago, "Electrodynamics of substances with simultaneously negative values of sigma and mu," *Soviet Physics Uspekhi*, vol. 10, pp. 509–514, 1968. [Online]. Available: https://doi.org/10.1070/PU1968v010n04ABEH003699

[34] D. R. Smith, W. J. Padilla, D. C. Vier, S. C. Nemat-Nasser, and S. Schultz, "Composite medium with simultaneously negative permeability and permittivity," *Physical Review Letters*, vol. 84, pp. 4184–4187, 2000. [Online]. Available: https://doi.org/10.1103/PhysRevLett.84.4184

[35] W. Cai, U. K. Chettiar, A. V. Kildishev, and V. M. Shalaev, "Optical cloaking with metamaterials," *Nature Photonics*, vol. 1, pp. 224–227, 2007. [Online]. Available: https://doi.org/10.1038/nphoton.2007.28

[36] V. M. Shalaev, W. Cai, U. K. Chettiar, H.-K. Yuan, A. K. Sarychev, V. P. Drachev, and A. V. Kildishev, "Negative index of refraction in optical metamaterials," *Optics Letters*, vol. 30, pp. 3356–3358, 2005. [Online]. Available: https://doi.org/10.1364/OL.30.003356

[37] Y. Li, S. Kita, P. Munõz, O. Reshef, D. I. Vulis, M. Yin, M. Loncar, and E. Mazur, "On-chip zero-index metamaterials," *Nature Photonics*, vol. 9, pp. 738–742, 2015. [Online]. Available: https://doi.org/10.1038/nphoton.2015.198

[38] N. Liu, M. Mesch, T. Weiss, M. Hentschel, and H. Giessen, "Infrared perfect absorber and its application as plasmonic sensor," *Nano Letters*, vol. 10, pp. 2342–2348, 2010. [Online]. Available: https://doi.org/10.1021/nl9041033

[39] D. Lin, P. Fan, E. Hasman, and M. L. Brongersma, "Dielectric gradient metasurface optical elements," *Science*, vol. 345, pp. 298–302, 2014. [Online]. Available: https://doi.org/10.1126/science.1253213

[40] C. Wu, A. B. Khanikaev, R. Adato, N. Arju, A. A. Yanik, H. Altug, and G. Shvets, "Fano-resonant asymmetric metamaterials for ultrasensitive spectroscopy and identification of molecular monolayers," *Nature Materials 2011 11:1*, vol. 11, pp. 69–75, 2011. [Online]. Available: https://doi.org/10.1038/nmat3161

[41] F. Aieta, P. Genevet, M. A. Kats, N. Yu, R. Blanchard, Z. Gaburro, and F. Capasso, "Aberration-free ultrathin flat lenses and axicons at telecom wavelengths based on plasmonic metasurfaces," *Nano Letters*, vol. 12, pp. 4932–4936, 2012. [Online]. Available: https://doi.org/10.1021/nl302516v

[42] M. Khorasaninejad, W. T. Chen, R. C. Devlin, J. Oh, A. Y. Zhu, and F. Capasso, "Metalenses at visible wavelengths: Diffraction-limited focusing and subwavelength resolution imaging," *Science*, vol. 352, pp. 1190–1194, 2016. [Online]. Available: https://doi.org/10.1126/science.aaf6644

[43] B. Memarzadeh and H. Mosallaei, "Array of planar plasmonic scatterers functioning as light concentrator," *Optics Letters*, vol. 36, pp. 2569–2571, 2011. [Online]. Available: https://doi.org/10.1364/OL.36.002569

[44] N. Yu, P. Genevet, M. A. Kats, F. Aieta, J. P. Tetienne, F. Capasso, and Z. Gaburro, "Light propagation with phase discontinuities: Generalized laws of reflection and refraction," *Science*, vol. 334, pp. 333–337, 2011. [Online]. Available: https://doi.org/10.1126/science.1210713

[45] O. Paul, B. Reinhard, B. Krolla, R. Beigang, and M. Rahm, "Gradient index metamaterial based on slot elements," *Applied Physics Letters*, vol. 96, p. 241110, 2010. [Online]. Available: https://doi.org/10.1063/1.3453758

[46] C. L. H. Devlin, J. H. Vella, D. E. Walker, J. P. Lombardi, N. I. Limberopoulos, and J. S. Derov, "Nanoscale gradient index media fabrication for extreme control and tunability of optical wave propagation." IEEE, 6 2014, pp. 46–49, From Duplicate 1 (<i>Nanoscale gradient index media fabrication for extreme control and tunability of optical wave propagation</i> - Devlin, Christie L H; Vella, Jarrett H; Walker, Dennis E; Lombardi, Jack P; Limberopoulos, Nicholaos I; Derov, John S)
And Duplicate 2 (<i>Nanoscale gradient index media fabrication for extreme control and tunability of optical wave propagation</i>

- Devlin, Christie L. H.; Vella, Jarrett H.; Walker, Dennis E.; Lombardi, Jack P.; Limberopoulos, Nicholaos I.; Derov, John S.)

PAPER SHOWS TESTING SET UP

I don't understand how they're testing this? They seem to be sending light through the sides rather than through the lens fce

From Duplicate 3 (<i>Nanoscale gradient index media fabrication for extreme control and tunability of optical wave propagation</i> - Devlin, Christie L H; Vella, Jarrett H; Walker, Dennis E; Lombardi, Jack P; Limberopoulos, Nicholaos I; Derov, John S)

PAPER SHOWS TESTING SET UP. [Online]. Available: https://doi.org/10.1109/NAECON.2014.7045774

[47] A. Arbabi, R. M. Briggs, Y. Horie, M. Bagheri, and A. Faraon, "Efficient dielectric metasurface collimating lenses for mid-infrared quantum cascade lasers," *Optics Express*, vol. 23, pp. 33 310–33 317, 2015. [Online]. Available: https://doi.org/10.1364/OE.23.033310

[48] M. Gonidec, "Concept of non-periodic metasurfaces based on positional gradients applied to ir-flat lenses," *Optical Materials Express*, vol. 7, pp. 2346–2351, 2017. [Online]. Available: https://doi.org/10.1364/OME.7.002346

[49] P. Genevet, F. Capasso, F. Aieta, M. Khorasaninejad, and R. Devlin, "Recent advances in planar optics: from plasmonic to dielectric metasurfaces," *Review Article*, vol. 4, pp. 139–152, 2017. [Online]. Available: https://doi.org/10.1364/OPTICA.4.000139

[50] J. C. M. Garnett, "Colours in metal glasses, in metallic films, and in metallic solutions. ii," *Philosophical Transactions of the Royal Society A: Mathematical, Physical and Engineering Sciences*, vol. 205, 1906. [Online]. Available: https://doi.org/10.1098/rsta.1906.0007

[51] ——, "Colours in metal glasses and in metallic films," *Philosophical Transactions of the Royal Society A: Mathematical, Physical and Engineering Sciences*, vol. 203, 1904. [Online]. Available: https://doi.org/10.1098/rsta.1904.0024

[52] D. A. G. Bruggeman, "Calculation of different physical constants of heterogeneous substances. i. dielectric constants and conductivities of the mixed bodies of isotropic substances," *Annalen der Physik*, vol. 416, pp. 636–664, 1935. [Online]. Available: https://doi.org/10.1002/andp.19354160705

[53] D. J. Bergman, "Exactly solvable microscopic geometries and rigorous bounds for the complex dielectric constant of a two-component composite material," *Physical Review Letters*, vol. 44, pp. 1285–1287, 1980. [Online]. Available: https://doi.org/10.1103/PhysRevLett.44.1285

[54] G. W. Milton, "Bounds on the complex dielectric constant of a composite material," *Applied Physics Letters*, vol. 37, pp. 300–302, 1980. [Online]. Available: https://doi.org/10.1063/1.91895

[55] D. R. Smith, S. Schultz, P. Markoš, and C. M. Soukoulis, "Determination of effective permittivity and permeability of metamaterials from reflection and transmission

coefficients," *Physical Review B*, vol. 65, p. 195104, 2002. [Online]. Available: https://doi.org/10.1103/PhysRevB.65.195104

[56] A. V. Kildishev, W. Cai, U. K. Chettiar, H.-K. Yuan, A. K. Sarychev, V. P. Drachev, and V. M. Shalaev, "Negative refractive index in optics of metal-dielectric composites," *Journal of the Optical Society of America B*, vol. 23, pp. 423–433, 2006. [Online]. Available: https://doi.org/10.1364/JOSAB.23.000423

[57] M. N. O. Sadiku, *Numerical techniques in electromagnetics*, 2nd ed. CRC Press, 2001.

[58] J. Hoffmann, C. Hafner, P. Leidenberger, J. Hesselbarth, and S. Burger, "Comparison of electromagnetic field solvers for the 3d analysis of plasmonic nanoantennas," vol. 73900J. SPIE, 2009. [Online]. Available: https://doi.org/10.1117/12.828036

[59] W. Ehrfeld and H. Lehr, "Deep x-ray lithography for the production of three-dimensional microstructures from metals, polymers and ceramics," *Radiation Physics and Chemistry*, vol. 45, pp. 349–365, 1995. [Online]. Available: https://doi.org/10.1016/0969-806X(93)E0007-R

[60] Y.-T. Chen, T.-N. Lo, Y. S. Chu, J. Yi, C.-J. Liu, J.-Y. Wang, C.-L. Wang, C.-W. Chiu, T.-E. Hua, Y. Hwu, Q. Shen, G.-C. Yin, K. S. Liang, H.-M. Lin, J. H. Je, and G. Margaritondo, "Full-field hard x-ray microscopy below 30 nm: a challenging nanofabrication achievement," *Nanotechnology*, vol. 19, p. 395302, 2008. [Online]. Available: https://doi.org/10.1088/0957-4484/19/39/395302

[61] F. Jipa, M. Zamfirescu, A. Velea, M. Popescu, and R. Dabu, "Femtosecond laser lithography in organic and non-organic materials," 7 2013. [Online]. Available: http://www.intechopen.com/books/updates-in-advanced-lithography/femtosecond-laser-lithography-in-organic-and-non-organic-materials

[62] Y. Chen, "Nanofabrication by electron beam lithography and its applications: A review," *Microelectronic Engineering*, vol. 135, pp. 57–72, 2015.

[63] S. Zhang, W. Fan, N. C. Panoiu, K. J. Malloy, R. M. Osgood, and S. R. J. Brueck, "Experimental demonstration of near-infrared negative-index metamaterials," *Physical Review Letters*, vol. 95, p. 137404, 2005. [Online]. Available: https://doi.org/10.1103/PhysRevLett.95.137404

[64] W. Hu, K. Sarveswaran, M. Lieberman, and G. H. Bernstein, "Sub-10 nm electron beam lithography using cold development of poly(methylmethacrylate)," *Journal of Vacuum Science & Technology B: Microelectronics and Nanometer Structures*, vol. 22, p. 1711, 2004. [Online]. Available: https://doi.org/10.1116/1.1763897

[65] A. Boltasseva and V. M. Shalaev, "Fabrication of optical negative-index metamaterials: Recent advances and outlook," *Metamaterials*, vol. 2, pp. 1–17, 2008. [Online]. Available: https://doi.org/10.1016/j.metmat.2008.03.004

[66] C. Enkrich, F. Pérez-Willard, D. Gerthsen, J. F. Zhou, T. Koschny, C. M. Soukoulis, M. Wegener, and S. Linden, "Focused-ion-beam nanofabrication of near-infrared

magnetic metamaterials," *Advanced Materials*, vol. 17, pp. 2547–2549, 2005. [Online]. Available: https://doi.org/10.1002/adma.200500804

[67] M. Askari, D. A. Hutchins, P. J. Thomas, L. Astolfi, R. L. Watson, M. Abdi, M. Ricci, S. Laureti, L. Nie, S. Freear, R. Wildman, C. Tuck, M. Clarke, E. Woods, and A. T. Clare, "Additive manufacturing of metamaterials: A review," *Additive Manufacturing*, vol. 36, p. 101562, 2020. [Online]. Available: https://doi.org/10.1016/j.addma.2020.101562

[68] M. Malinauskas, M. Farsari, A. Piskarskas, and S. Juodkazis, "Ultrafast laser nanostructuring of photopolymers: A decade of advances," *Physics Reports*, vol. 533, pp. 1–31, 2013. [Online]. Available: https://doi.org/10.1016/j.physrep.2013.07.005

[69] I. Gibson, D. W. Rosen, B. Stucker *et al.*, *Additive manufacturing technologies*. Springer, 2010, vol. 238.

[70] S. Maruo and J. T. Fourkas, "Recent progress in multiphoton microfabrication," *Laser & Photonics Reviews*, vol. 2, pp. 100–111, 2008. [Online]. Available: https://doi.org/10.1002/lpor.200710039

[71] S. Maruo, K. Ikuta, and H. Korogi, "Submicron manipulation tools driven by light in a liquid," *Applied Physics Letters*, vol. 82, pp. 133–135, 2003. [Online]. Available: https://doi.org/10.1063/1.1533853

[72] ——, "Force-controllable, optically driven micromachines fabricated by single-step two-photon microstereolithography," *Journal of Microelectromechanical Systems*, vol. 12, pp. 533–539, 10 2003. [Online]. Available: https://doi.org/10.1109/JMEMS.2003.817894

[73] S. Maruo and H. Inoue, "Optically driven micropump produced by three-dimensional two-photon microfabrication," *Applied Physics Letters*, vol. 89, p. 144101, 2006. [Online]. Available: https://doi.org/10.1063/1.2358820

[74] T. Gissibl, S. Thiele, A. Herkommer, and H. Giessen, "Two-photon direct laser writing of ultracompact multi-lens objectives," *Nature Photonics*, vol. 10, pp. 554–560, 2016. [Online]. Available: https://doi.org/10.1038/nphoton.2016.121

[75] P.-I. Dietrich, M. Blaicher, I. Reuter, M. Billah, T. Hoose, A. Hofmann, C. Caer, R. Dangel, B. Offrein, U. Troppenz, M. Moehrle, W. Freude, and C. Koos, "In situ 3d nanoprinting of free-form coupling elements for hybrid photonic integration," *Nature Photonics*, vol. 12, pp. 241–247, 2018. [Online]. Available: https://doi.org/10.1038/s41566-018-0133-4

[76] J. Serbin, A. Ovsianikov, and B. Chichkov, "Fabrication of woodpile structures by two-photon polymerization and investigation of their optical properties," *Optics Express*, vol. 12, pp. 5221–5228, 2004. [Online]. Available: https://doi.org/10.1364/OPEX.12.005221

[77] W. J. Chen, J. C. W. Lee, J. W. Dong, C. W. Qiu, and H. Z. Wang, "Fano resonance of three-dimensional spiral photonic crystals: Paradoxical transmission and polarization gap," *Applied Physics Letters*, vol. 98, p. 081116, 2011. [Online]. Available: https://doi.org/10.1063/1.3560338

[78] M. Thiel, M. S. Rill, G. von Freymann, and M. Wegener, "Three-dimensional bi-chiral photonic crystals," *Advanced Materials*, vol. 21, pp. 4680–4682, 2009. [Online]. Available: https://doi.org/10.1002/adma.200901601

[79] M. Thiel, M. Wegener, and G. V. Freymann, "Layer-by-layer three-dimensional chiral photonic crystals," 2008, pp. 1–2. [Online]. Available: https://doi.org/10.1109/CLEO.2008.4551903

[80] J. K. Gansel, M. Thiel, M. S. Rill, M. Decker, K. Bade, V. Saile, G. von Freymann, S. Linden, and M. Wegener, "Gold helix photonic metamaterial as broadband circular polarizer." *Science*, vol. 325, pp. 1513–1515, 2009. [Online]. Available: https://doi.org/10.1126/science.1177031

[81] M. S. Rill, C. Plet, M. Thiel, I. Staude, G. von Freymann, S. Linden, and M. Wegener, "Photonic metamaterials by direct laser writing and silver chemical vapour deposition," *Nature Materials*, vol. 7, pp. 543–546, 2008. [Online]. Available: https://doi.org/10.1038/nmat2197

[82] J. Moughames, S. Jradi, T. M. Chan, S. Akil, Y. Battie, A. E. Naciri, Z. Herro, S. Guenneau, S. Enoch, L. Joly, J. Cousin, and A. Bruyant, "Wavelength-scale light concentrator made by direct 3d laser writing of polymer metamaterials," *Scientific Reports*, vol. 6, pp. 1–8, 2016. [Online]. Available: https://doi.org/10.1038/srep33627

[83] M. Göppert-Mayer, "Elementary processes with two quantum transitions," *Ann. Phys. (Berlin)*, vol. 18, pp. 466–479, 2009. [Online]. Available: https://doi.org/10.1002/andp.200910358

[84] X. Zhou, Y. Hou, and J. Lin, "A review on the processing accuracy of two-photon polymerization," *AIP Advances*, vol. 5, p. 30701, 2015. [Online]. Available: https://doi.org/10.1063/1.4916886

[85] S. Maruo, O. Nakamura, and S. Kawata, "Three-dimensional microfabrication with two-photon-absorbed photopolymerization," *Optics Letters*, vol. 22, pp. 132–134, 1997. [Online]. Available: https://doi.org/10.1364/OL.22.000132

[86] C. N. N. LaFratta, J. T. T. Fourkas, T. Baldacchini, and R. A. A. Farrer, "Multiphoton fabrication," *Angewandte Chemie International Edition*, vol. 46, pp. 6238–6258, 2007. [Online]. Available: https://doi.org/10.1002/anie.200603995

[87] S.-H. Park, D.-Y. Yang, and K.-S. Lee, "Two-photon stereolithography for realizing ultraprecise three-dimensional nano/microdevices," *Laser & Photonics Reviews*, vol. 3, pp. 1–11, 2009. [Online]. Available: https://doi.org/10.1002/lpor.200810027

[88] R. Wollhofen, J. Katzmann, C. Hrelescu, J. Jacak, and T. A. Klar, "120 nm resolution and 55 nm structure size in sted-lithography," *Optics Express*, vol. 21, pp. 10 831–10 840, 2013. [Online]. Available: https://doi.org/10.1364/OE.21.010831

[89] M. Malinauskas, H. Gilbergs, A. Žukauskas, V. Purlys, D. Paipulas, and R. Gadonas, "A femtosecond laser-induced two-photon photopolymerization technique for structuring microlenses," *Journal of Optics*, vol. 12, p. 035204, 2010. [Online]. Available: https://doi.org/10.1088/2040-8978/12/3/035204

[90] X.-Z. Dong, Z.-S. Zhao, and X.-M. Duan, "Improving spatial resolution and reducing aspect ratio in multiphoton polymerization nanofabrication," *Applied Physics Letters*, vol. 92, p. 91113, 2008. [Online]. Available: https://doi.org/10.1063/1.2841042

[91] J.-F. Xing, X.-Z. Dong, W.-Q. Chen, X.-M. Duan, N. Takeyasu, T. Tanaka, and S. Kawata, "Improving spatial resolution of two-photon microfabrication by using photoinitiator with high initiating efficiency," *Applied Physics Letters*, vol. 90, p. 131106, 2007. [Online]. Available: https://doi.org/10.1063/1.2717532

[92] K. Takada, H.-B. Sun, and S. Kawata, "Improved spatial resolution and surface roughness in photopolymerization-based laser nanowriting," *Applied Physics Letters*, vol. 86, p. 71122, 2005. [Online]. Available: https://doi.org/10.1063/1.1864249

[93] S. H. Park, T. W. Lim, D.-Y. Yang, R. H. Kim, and K.-S. Lee, "Improvement of spatial resolution in nano-stereolithography using radical quencher," *Macromolecular Research*, vol. 14, pp. 559–564, 2006. [Online]. Available: https://doi.org/10.1007/BF03218724

[94] Q. Hu, X.-Z. Sun, C. D. J. Parmenter, M. W. Fay, E. F. Smith, G. A. Rance, Y. He, F. Zhang, Y. Liu, D. Irvine, C. Tuck, R. Hague, and R. Wildman, "Additive manufacture of complex 3d au-containing nanocomposites by simultaneous two-photon polymerisation and photoreduction," *Scientific reports*, vol. 7, p. 17150, 12 2017. [Online]. Available: https://doi.org/10.1038/s41598-017-17391-1

[95] R. Liu, C. Ji, Z. Zhao, and T. Zhou, "Metamaterials: Reshape and rethink," *Engineering*, vol. 1, pp. 179–184, 2015. [Online]. Available: https://doi.org/10.15302/J-ENG-2015036

[96] J. E. G. J. Wijnhoven and W. L. Vos, "Preparation of photonic crystals made of air spheres in titania," *Science*, vol. 281, pp. 802–804, 1998. [Online]. Available: https://doi.org/10.1126/science.281.5378.802

[97] J. Fischer, G. von Freymann, and M. Wegener, "The materials challenge in diffraction-unlimited direct-laser-writing optical lithography," *Advanced Materials*, vol. 22, pp. 3578–3582, 2010. [Online]. Available: https://doi.org/10.1002/adma.201000892

[98] H.-B. Sun, T. Suwa, K. Takada, R. P. Zaccaria, M.-S. Kim, K.-S. Lee, and S. Kawata, "Shape precompensation in two-photon laser nanowriting of photonic

lattices," *Applied Physics Letters*, vol. 85, pp. 3708–3710, 2004. [Online]. Available: https://doi.org/10.1063/1.1807019

[99] M. Deubel, G. von Freymann, M. Wegener, S. Pereira, K. Busch, and C. M. Soukoulis, "Direct laser writing of three-dimensional photonic-crystal templates for telecommunications," *Nature materials*, vol. 3, p. 444, 2004. [Online]. Available: https://doi.org/10.1038/nmat1155

[100] E. Andrzejewska, "Free radical photopolymerization of multifunctional monomers," pp. 62–81, 2016. [Online]. Available: https://doi.org/10.1016/B978-0-323-35321-2.00004-2

[101] M. Farsari, A. Ovsianikov, M. Vamvakaki, I. Sakellari, D. Gray, B. N. Chichkov, and C. Fotakis, "Fabrication of three-dimensional photonic crystal structures containing an active nonlinear optical chromophore," *Applied Physics A 2008 93:1*, vol. 93, pp. 11–15, 2008. [Online]. Available: https://doi.org/10.1007/s00339-008-4642-8

[102] J. Purtov, A. Verch, P. Rogin, and R. Hensel, "Improved development procedure to enhance the stability of microstructures created by two-photon polymerization," *Microelectronic Engineering*, vol. 194, pp. 45–50, 2018. [Online]. Available: https://doi.org/10.1016/j.mee.2018.03.009

[103] C. N. LaFratta and L. Li, "Making two-photon polymerization faster," pp. 221–241, 2016. [Online]. Available: https://doi.org/10.1016/B978-0-323-35321-2.00011-X

[104] J. T. Fourkas, "Fundamentals of two-photon fabrication," pp. 45–61, 2016. [Online]. Available: https://doi.org/10.1016/B978-0-323-35321-2.00003-0

[105] M. Albota, D. Beljonne, J.-L. Brédas, J. E. Ehrlich, J.-Y. Fu, A. A. Heikal, S. E. Hess, T. Kogej, M. D. Levin, S. R. Marder, D. McCord-Maughon, J. W. Perry, H. Röckel, M. Rumi, G. Subramaniam, W. W. Webb, X.-L. Wu, and C. Xu, "Design of organic molecules with large two-photon absorption cross sections," *Science*, vol. 281, pp. 1653–1656, 1998. [Online]. Available: https://doi.org/10.1126/science.281.5383.1653

[106] K. J. Schafer, J. M. Hales, M. Balu, K. D. Belfield, E. W. V. Stryland, and D. J. Hagan, "Two-photon absorption cross-sections of common photoinitiators," *Journal of Photochemistry and Photobiology A: Chemistry*, vol. 162, pp. 497–502, 2004. [Online]. Available: https://doi.org/10.1016/S1010-6030(03)00394-0

[107] J. ichi Kato, N. Takeyasu, Y. Adachi, H.-B. Sun, and S. Kawata, "Multiple-spot parallel processing for laser micronanofabrication," *Applied Physics Letters*, vol. 86, p. 44102, 2005. [Online]. Available: https://doi.org/10.1063/1.1855404

[108] Y. Murakami, C. A. Coenjarts, and C. K. Ober, "Preparation and two-photon lithography of a sulfur containing resin with high refractive index," *Journal of Photopolymer Science and Technology*, vol. 17, pp. 115–118, 2004. [Online]. Available: https://doi.org/10.2494/photopolymer.17.115

[109] X.-M. Duan, H.-B. Sun, K. Kaneko, and S. Kawata, "Two-photon polymerization of metal ions doped acrylate monomers and oligomers for three-dimensional structure fabrication," *Thin Solid Films*, vol. 453-454, pp. 518–521, 2004. [Online]. Available: https://doi.org/10.1016/j.tsf.2003.11.126

[110] D. J. Shir, E. C. Nelson, D. Chanda, A. Brzezinski, P. V. Braun, J. A. Rogers, and P. Wiltzius, "Dual exposure, two-photon, conformal phase mask lithography for three dimensional silicon inverse woodpile photonic crystals," *Journal of Vacuum Science & Technology B, Nanotechnology and Microelectronics: Materials, Processing, Measurement, and Phenomena*, vol. 28, p. 783, 2010. [Online]. Available: https://doi.org/10.1116/1.3456181

[111] F. Klein, B. Richter, T. Striebel, C. M. Franz, G. V. Freymann, M. Wegener, and M. Bastmeyer, "Two-component polymer scaffolds for controlled three-dimensional cell culture," *Advanced Materials*, vol. 23, pp. 1341–1345, 2011. [Online]. Available: https://doi.org/10.1002/adma.201004060

[112] S. Rekštyte, "Direct laser fabrication of composite material 3d microstructured scaffolds," *Journal of Laser Micro/Nanoengineering*, vol. 9, pp. 25–30, 2014. [Online]. Available: http://www.jlps.gr.jp/jlmn/archive/09/09_01/

[113] M. Askari, C. J. Tuck, Q. Hu, R. J. M. Hague, and R. D. Wildman, "Multimaterial manufacture through combining optical tweezers with multiphoton fabrication," *Journal of Laser Micro/Nanoengineering*, vol. 14, pp. 80–87, 2019. [Online]. Available: http://www.jlps.gr.jp/jlmn/archive/14/14_01/

[114] A. I. Kuznetsov, A. B. Evlyukhin, C. Reinhardt, A. Seidel, R. Kiyan, W. Cheng, A. Ovsianikov, and B. N. Chichkov, "Laser-induced transfer of metallic nanodroplets for plasmonics and metamaterial applications," *Journal of the Optical Society of America B*, vol. 26, pp. B130–B138, 2009. [Online]. Available: https://doi.org/10.1364/JOSAB.26.00B130

[115] M. G. Guney and G. K. Fedder, "Estimation of line dimensions in 3d direct laser writing lithography," *Journal of Micromechanics and Microengineering*, vol. 26, p. 105011, 2016, ascending scan method
Numerical simulations. [Online]. Available: https://doi.org/10.1088/0960-1317/26/10/105011

[116] C. A. Schneider, W. S. Rasband, and K. W. Eliceiri, "Nih image to imagej: 25 years of image analysis." *Nature methods*, vol. 9, pp. 671–675, 2012. [Online]. Available: https://doi.org/10.1038/nmeth.2089

[117] D. Legland, I. Arganda-Carreras, and P. Andrey, "Morpholibj: Integrated library and plugins for mathematical morphology with imagej," *Bioinformatics*, vol. 32, pp. 3532–3534, 2016. [Online]. Available: https://doi.org/10.1093/bioinformatics/btw413

[118] C. Leys, C. Ley, O. Klein, P. Bernard, and L. Licata, "Detecting outliers: Do not use standard deviation around the mean, use absolute deviation around the median,"

Journal of Experimental Social Psychology, vol. 49, pp. 764–766, 2013. [Online]. Available: https://doi.org/10.1016/j.jesp.2013.03.013

[119] S. K. Saha, C. Divin, J. A. Cuadra, and R. M. Panas, "Effect of proximity of features on the damage threshold during submicron additive manufacturing via two-photon polymerization," *Journal of Micro and Nano-Manufacturing*, vol. 5, p. 31002, 2017. [Online]. Available: https://doi.org/10.1115/1.4036445

[120] J. B. Mueller, J. Fischer, Y. J. Mange, T. Nann, and M. Wegener, "In-situ local temperature measurement during three-dimensional direct laser writing," *Applied Physics Letters*, vol. 103, p. 123107, 2013. [Online]. Available: https://doi.org/10.1063/1.4821556

[121] A.-I. Bunea, N. del Castillo Iniesta, A. Droumpali, A. E. Wetzel, E. Engay, and R. Taboryski, "Micro 3d printing by two-photon polymerization: Configurations and parameters for the nanoscribe system," *Micro*, vol. 1, pp. 164–180, 2021. [Online]. Available: https://doi.org/10.3390/micro1020013

[122] C. H. Lee, T. W. Chang, K. L. Lee, J. Y. Lin, and J. Wang, "Fabricating high-aspect-ratio sub-diffraction-limit structures on silicon with two-photon photopolymerization and reactive ion etching," *Applied Physics A*, vol. 79, pp. 2027–2031, 2004. [Online]. Available: https://doi.org/10.1007/s00339-003-2423-y

[123] J. Serbin, A. Egbert, A. Ostendorf, B. N. Chichkov, R. Houbertz, G. Domann, J. Schulz, C. Cronauer, L. Fröhlich, M. Popall, G. Domann, J. Schulz, J. Serbin, L. Fröhlich, M. Popall, and R. Houbertz, "Femtosecond laser-induced two-photon polymerization of inorganic–organic hybrid materials for applications in photonics," *Optics Letters*, vol. 28, pp. 301–303, 2003. [Online]. Available: https://doi.org/10.1364/OL.28.000301

[124] S. Shukla, E. P. Furlani, X. Vidal, M. T. Swihart, and P. N. Prasad, "Two-photon lithography of sub-wavelength metallic structures in a polymer matrix," *Advanced Materials*, vol. 22, pp. 3695–3699, 2010. [Online]. Available: https://doi.org/10.1002/adma.201000059

[125] Y. Liu, D. D. Nolte, and L. J. Pyrak-Nolte, "Large-format fabrication by two-photon polymerization in su-8," *Applied Physics A 2010 100:1*, vol. 100, pp. 181–191, 5 2010. [Online]. Available: https://link.springer.com/article/10.1007/s00339-010-5735-8

[126] A. G. Izard, E. P. Garcia, M. Dixon, E. O. Potma, T. Baldacchini, and L. Valdevit, "Enhanced adhesion in two-photon polymerization direct laser writing," *AIP Advances*, vol. 10, p. 045217, 4 2020. [Online]. Available: https://aip.scitation.org/doi/abs/10.1063/5.0005548

[127] H. F. Ma and T. J. Cui, "Three-dimensional broadband ground-plane cloak made of metamaterials," *Nature Communications*, vol. 1, pp. 1–6, 2010. [Online]. Available: https://doi.org/10.1038/ncomms1023

[128] W. X. Jiang, S. Ge, T. Han, S. Zhang, M. Q. Mehmood, C.-W. Qiu, T. J. Cui, W. X. Jiang, S. Ge, T. J. Cui, T. Han, M. Q. Mehmood, C. w Qiu, and S. Zhang, "Shaping 3d path of electromagnetic waves using gradient-refractive-index metamaterials," *Advanced Science*, vol. 3, p. 1600022, 2016. [Online]. Available: https://doi.org/10.1002/advs.201600022

[129] F. Maggiorelli, A. Paraskevopoulos, J. C. Vardaxoglou, M. Albani, and S. Maci, "Profile inversion and closed form formulation of compact grin lenses," *IEEE Open Journal of Antennas and Propagation*, vol. 2, pp. 315–325, 2021. [Online]. Available: https://doi.org/10.1109/OJAP.2021.3059468

[130] J. S. Oakdale, J. Ye, W. L. Smith, J. Biener, X. Zhou, Y. Hou, J. Lin, S. Peng, R. Zhang, V. H. Chen, E. T. Khabiboulline, P. Braun, H. A. Atwater, J. Ye, W. L. Smith, and J. Biener, "Post-print uv curing method for improving the mechanical properties of prototypes derived from two-photon lithography," *Optics Express*, vol. 24, pp. 27 077–27 086, 2016. [Online]. Available: https://doi.org/10.1364/OE.24.027077

[131] S. Maruo, T. Hasegawa, and N. Yoshimura, "Single-anchor support and supercritical co2 drying enable high-precision microfabrication of three-dimensional structures," *Optics Express*, vol. 17, pp. 20 945–20 951, 2009. [Online]. Available: https://doi.org/10.1364/OE.17.020945

[132] S. Ristok, S. Thiele, A. Toulouse, A. M. Herkommer, and H. Giessen, "Stitching-free 3d printing of millimeter-sized highly transparent spherical and aspherical optical components," *Optical Materials Express*, vol. 10, pp. 2370–2378, 2020. [Online]. Available: https://doi.org/10.1364/OME.401724

[133] J. S. Oakdale, R. F. Smith, J. B. Forien, W. L. Smith, S. J. Ali, L. B. B. Aji, T. M. Willey, J. Ye, A. W. van Buuren, M. A. Worthington, S. T. Prisbrey, H. S. Park, P. A. Amendt, T. F. Baumann, and J. Biener, "Direct laser writing of low-density interdigitated foams for plasma drive shaping," *Advanced Functional Materials*, vol. 27, p. 1702425, 2017. [Online]. Available: https://doi.org/10.1002/adfm.201702425

[134] M. Yin, X. Y. Tian, L. L. Wu, D. C. Li, J. B. Pendry, D. Schurig, J. J. Mock, B. J. Justice, S. A. Cummer, A. F. Starr, T. Ergin, N. Stenger, P. Brenner, M. Wegener, X. Y. Tian, L. L. Wu, and D. C. Li, "A broadband and omnidirectional electromagnetic wave concentrator with gradient woodpile structure," *Optics Express*, vol. 21, pp. 19 082–19 090, 2013. [Online]. Available: https://doi.org/10.1364/OE.21.019082

[135] Y. Li, S. Park, M. Mclamb, M. Lata, S. Schöche, D. Childers, I. D. Aggarwal, M. K. Poutous, G. Boreman, and T. Hofmann, "Uv to nir optical properties of ip-dip, ip-l, and ip-s after two-photon polymerization determined by spectroscopic ellipsometry," *Optical Materials Express*, vol. 9, 2019. [Online]. Available: https://doi.org/10.1364/OME.9.004318

[136] "Modeling periodic structures in comsol multiphysics®." [Online]. Available: https://www.comsol.com/video/modeling-periodic-structures-in-comsol-multiphysics

[137] D. R. Smith, D. C. Vier, T. Koschny, and C. M. Soukoulis, “Electromagnetic parameter retrieval from inhomogeneous metamaterials,” *Physical Review E - Statistical, Nonlinear, and Soft Matter Physics*, vol. 71, p. 036617, 2005. [Online]. Available: https://doi.org/10.1103/PhysRevE.71.036617

[138] X. Chen, T. M. Grzegorczyk, B. I. Wu, J. Pacheco, and J. A. Kong, “Robust method to retrieve the constitutive effective parameters of metamaterials,” *Physical Review E - Statistical Physics, Plasmas, Fluids, and Related Interdisciplinary Topics*, vol. 70, p. 016608, 2004. [Online]. Available: https://doi.org/10.1103/PhysRevE.70.016608

[139] H. Wang, X. Chen, and K. Huang, “An improved approach to determine the branch index for retrieving the constitutive effective parameters of metamaterials,” *Journal of Electromagnetic Waves and Applications*, vol. 25, pp. 85–96, 2011. [Online]. Available: https://doi.org/10.1163/156939311793898341

[140] X. Zhang and Y. Wu, “Effective medium theory for anisotropic metamaterials,” *Scientific Reports*, vol. 5, p. 7892, 2015. [Online]. Available: https://doi.org/10.1038/srep07892

[141] C. W. Lan, X. J. Fu, X. M. Liu, B. Li, and J. Zhou, “Double negative optical metamaterial with all-dielectric fishnet structure,” *Advanced Materials Research*, vol. 873, pp. 813–818, 2014. [Online]. Available: https://doi.org/10.4028/www.scientific.net/AMR.873.813

[142] F. Gaufillet, S. Marcellin, and E. Akmansoy, “Dielectric metamaterial-based gradient index lens in the terahertz frequency range,” *IEEE Journal of Selected Topics in Quantum Electronics*, vol. 23, p. 4700605, 2017. [Online]. Available: https://doi.org/10.1109/JSTQE.2016.2633825

[143] D. B. Fullager, G. D. Boreman, and T. Hofmann, “Infrared dielectric response of nanoscribe ip-dip and ip-l monomers after polymerization from 250 cm$\{^-1\}$ to 6000 cm$\{^-1\}$,” *Optical Materials Express*, vol. 7, p. 888, 2017. [Online]. Available: https://doi.org/10.1364/OME.7.000888

[144] S. Dottermusch, D. Busko, M. Langenhorst, U. W. Paetzold, and B. S. Richards, “Exposure-dependent refractive index of nanoscribe ip-dip photoresist layers,” *Optics Letters*, vol. 44, pp. 29–32, 2019. [Online]. Available: https://doi.org/10.1364/OL.44.000029

[145] T. Amotchkina, M. Trubetskov, D. Hahner, and V. Pervak, “Characterization of e-beam evaporated ge, ybf3, zns, and laf3 thin films for laser-oriented coatings,” *Applied Optics*, vol. 59, pp. A40–A47, 2020. [Online]. Available: https://doi.org/10.1364/AO.59.000A40

[146] M. Malinauskas, A. Ukauskas, V. Purlys, A. Gaidukeviiut, Z. Baleviius, A. Piskarskas, C. Fotakis, S. Pissadakis, D. Gray, R. Gadonas, M. Vamvakaki, and M. Farsari, “3d microoptical elements formed in a photostructurable germanium silicate by direct laser writing,” *Optics and Lasers in Engineering*, vol. 50, pp. 1785–1788, 2012. [Online]. Available: https://doi.org/10.1016/j.optlaseng.2012.07.001

[147] M. Schmid, D. Ludescher, and H. Giessen, “Optical properties of photoresists for femtosecond 3d printing: refractive index, extinction, luminescence-dose dependence, aging, heat treatment and comparison between 1-photon and 2-photon exposure,” *Optical Materials Express*, vol. 9, p. 4564, 2019. [Online]. Available: https://doi.org/10.1364/OME.9.004564

[148] . D. J. Richardson, J. M. Fini, L. E. Nelson, and . C. Xia, “Mode-selective coupling between few-mode fibers and buried channel waveguides,” *Optics Express, Vol. 24, Issue 26, pp. 30108-30123*, vol. 24, pp. 30 108–30 123, 12 2016. [Online]. Available: https://doi.org/10.1364/OE.24.030108

[149] “Defining a mapped dielectric distribution of a material (rf).” [Online]. Available: https://www.comsol.com/model/defining-a-mapped-dielectric-distribution-of-a-material-rf-13873

[150] S. Shrestha, A. C. Overvig, M. Lu, A. Stein, and N. Yu, “Broadband achromatic dielectric metalenses,” *Light: Science & Applications 2018 7:1*, vol. 7, pp. 1–11, 11 2018. [Online]. Available: https://www.nature.com/articles/s41377-018-0078-x

[151] J. Neu, B. Krolla, O. Paul, B. Reinhard, R. Beigang, and M. Rahm, “Metamaterial-based gradient index lens with strong focusing in the thz frequency range,” *Optics Express*, vol. 18, pp. 27 748–27 757, 2010. [Online]. Available: https://doi.org/10.1364/OE.18.027748

[152] H. Karstensen and K. Drögemüller, “Loss analysis of laser diode to single-mode fiber couplers with glass spheres or silicon planoconvex lenses,” *Journal of Lightwave Technology*, vol. 8, pp. 739–747, 1990. [Online]. Available: https://doi.org/10.1109/50.54482

[153] D. S. Rovira, H. M. Nielsen, R. Taboryski, and A. I. Bunea, “Additive manufacturing of polymeric scaffolds for biomimetic cell membrane engineering,” *Materials & Design*, vol. 201, p. 109486, 2021. [Online]. Available: https://doi.org/10.1016/j.matdes.2021.109486

[154] B. Groever, C. Roques-Carmes, F. Capasso, and S. J. Byrnes, “Substrate aberration and correction for meta-lens imaging: an analytical approach,” *Applied Optics*, vol. 57, pp. 2973–2980, 2018. [Online]. Available: https://doi.org/10.1364/AO.57.002973

[155] W. Hadibrata, H. Wei, S. Krishnaswamy, and K. Aydin, “Inverse design and 3d printing of a metalens on an optical fiber tip for direct laser lithography,” *Nano Letters*, vol. 21, pp. 2422–2428, 2021. [Online]. Available: https://doi.org/10.1021/acs.nanolett.0c04463

[156] J. Cao, D. Zhao, and Q. Mao, “A highly reproducible and sensitive fiber sers probe fabricated by direct synthesis of closely packed agnps on the silanized fiber taper,” *Analyst*, vol. 142, pp. 596–602, 2017. [Online]. Available: https://doi.org/10.1039/C6AN02414A

[157] L. M. Rosenfeld, D. A. Sulway, G. F. Sinclair, V. Anant, M. G. Thompson, J. G. Rarity, and J. W. Silverstone, "Mid-infrared quantum optics in silicon," *Optics Express*, vol. 28, pp. 37 092–37 102, 2020. [Online]. Available: https://doi.org/10.1364/OE.386615

[158] R. Saint, W. Evans, Y. Zhou, T. Barrett, T. M. Fromhold, E. Saleh, I. Maskery, C. Tuck, R. Wildman, F. Oručević, and P. Krüger, "3d-printed components for quantum devices," *Scientific Reports*, vol. 8, pp. 1–9, 2018. [Online]. Available: https://doi.org/10.1038/s41598-018-26455-9

[159] J. Schindelin, I. Arganda-Carreras, E. Frise, V. Kaynig, M. Longair, T. Pietzsch, S. Preibisch, C. Rueden, S. Saalfeld, B. Schmid, J. Y. Tinevez, D. J. White, V. Hartenstein, K. Eliceiri, P. Tomancak, and A. Cardona, "Fiji: an open-source platform for biological-image analysis," *Nature Methods*, vol. 9, pp. 676–682, 2012. [Online]. Available: https://doi.org/10.1038/nmeth.2019

[160] "Frequency selective surface, periodic complementary split ring resonator." [Online]. Available: https://www.comsol.com/model/frequency-selective-surface-periodic-complementary-split-ring-resonator-15711